SCIENTIFIC REPORTS

OPEN

Received: 4 December 2017
Accepted: 2 July 2018

Quantifying Anharmonic Vibrations in Thermoelectric Layered Cobaltites and Their Role in Suppressing Thermal Conductivity

Susumu Fujii[1], Masato Yoshiya[1,2] & Craig A. J. Fisher[2]

Optimizing multiple materials properties which are simultaneously in competition with each other is one of the chief challenges in thermoelectric materials research. Introducing greater anharmonicity to vibrational modes is one strategy for suppressing phonon thermal transport in crystalline oxides without detrimentally affecting electronic conductivity, so that the overall thermoelectric efficiency can be improved. Based on perturbed molecular dynamics and associated numerical analyses, we show that CoO_2 layers in layered cobaltite thermoelectrics Na_xCoO_2 and $Ca_3Co_4O_9$ are responsible for most of the in-plane heat transport in these materials, and that the non-conducting intermediate layers in the two materials exhibit different kinds of anharmonicity. More importantly, thermal conduction is shown to be altered by modifying the structure of the intermediate layers. The simulation methods developed to quantify the effect of anharmonic atomic vibrations on thermal conductivity provide a new tool for the rational design of thermoelectric materials, and the insights gained should hasten the attainment of higher conversion efficiencies so that thermoelectrics can be put to widespread practical use.

Thermoelectric generators promise to enable efficient recovery of waste heat by converting it directly into electrical power. To be practicable, such devices must be made of thermoelectric materials with high conversion efficiencies, which are usually measured in terms of a figure of merit, $ZT = S^2\sigma T/\kappa$, where T is temperature and Z is proportional to the square of Seebeck coefficient, S; electronic conductivity σ; and the inversely proportional to the thermal conductivity, κ. To attain a high Z value, a material ideally should have high S, high σ and low κ. However, in most classes of materials all three properties are strongly correlated and not easily decoupled[1], so, for example, increasing the electronic conductivity is typically accompanied by an increase in thermal conductivity, making it notoriously difficult to obtain figures of merit high enough for practical application.

Recent studies have shown that introducing greater phonon anharmonicity to a structure is an effective means of suppressing phonon thermal conductivity, κ_{ph}, the chief component of thermal conductivity in a solid, without compromising the electronic properties[2,3]. The complex relationship between phonon anharmonicity and thermal conductivity, however, has meant that a rigorous quantitative understanding of these phenomena is lacking for all but the simplest of materials. Examining vibrational anharmonicity and its effect on thermal conduction is thus an important step in the development of innovative strategies for improving the performance and efficiency of thermoelectric materials[4].

Layered cobaltites such as Na_xCoO_2 and $(Ca_2CoO_3)_{0.62}CoO_2$ (normally approximated as $Ca_3Co_4O_9$) contain no toxic elements and are examples of materials with high power factors, $S^2\sigma$, and modest κ_{ph}. The electronic properties of these materials have been measured using various experimental methods[5–8], and it has been determined through a combination of experimental[9,10], theoretical[11,12] and *ab initio* modelling studies[13–16] that the highly correlated *d* electrons in the CoO_2 layers common to these cobaltites are responsible for the high S and σ values. Their modest κ_{ph} values, on the other hand, have mostly been attributed to the complicated layered structures that characterise the two compounds[8]. Recent experimental studies suggest that crystal layers adjacent to CoO_2 layers, viz., Na layers in Na_xCoO_2 and Ca_2CoO_3 layers in $Ca_3Co_4O_9$, play a role in suppressing κ_{ph}, either directly or indirectly. In the case of Na_xCoO_2, Na vacancies have been reported to exhibit a rattling mode[17], while

[1]Department of Adaptive Machine Systems, Osaka University, 2-1 Yamadaoka, Suita, Osaka, 565-0871, Japan. [2]Nanostructures Research Laboratory, Japan Fine Ceramics Center, 2-4-1 Mutsuno, Atsuta, Nagoya, 456-8587, Japan. Correspondence and requests for materials should be addressed to M.Y. (email: yoshiya@ams.eng.osaka-u.ac.jp)

	$NaCoO_2$			**$Na_{0.5}CoO_2$**			**$Ca_3Co_4O_9$**		
	X	***Y***	***Z***	***X***	***Y***	***Z***	***X***	***Y***	***Z***
$\kappa_{\mathrm{overall}}$	44.55 ± 1.67	43.39 ± 1.92	19.01 ± 1.37	16.69 ± 0.19	14.11 ± 0.49	3.71 ± 0.05	6.60 ± 0.15	7.24 ± 0.28	3.32 ± 0.58
$\kappa_{\mathrm{CoO_2}}$	38.23	36.84	14.82	16.33	13.80	3.31	4.67	5.11	1.47
κ_{adj}	6.32	6.56	4.20	0.37	0.32	0.41	1.93	2.13	1.85
$\kappa'_{\mathrm{CoO_2}}$	57.07	54.99	22.12	25.92	21.90	5.25	13.21	14.46	4.16
κ'_{adj}	19.14	19.86	12.71	0.99	0.85	1.10	2.99	3.29	2.86

Table 1. Overall, partial and layer phonon thermal conductivities for Na_xCoO_2 ($x = 1.0, 0.5$) and $Ca_3Co_4O_9$ at 300 K. Directions X, Y and Z refer to the Cartesian coordinate system, with X parallel to the *a* axis, Y parallel to the *b* axis, and Z perpendicular to the *ab* plane (and CoO_2 layers); "adj" stands for layers adjacent to CoO_2 layers.

in misfit-layered $Ca_3Co_4O_9$, atoms in the Ca_2CoO_3 layers have been reported to exhibit anomalously large static and thermal displacements[18–21]. In both cases the layers adjacent to CoO_2 layers appear to enhance phonon scattering, although the exact mechanism by which they do this is not yet clear.

To address this issue, we analysed atom vibrations and phonon transport mechanisms in these compounds quantitatively using the perturbed molecular dynamics (MD) method[22] in conjunction with lattice dynamics (LD) simulations, focussing on the degree and distribution of vibrational anharmonicity in different layers. The role of anharmonic vibrations in the non-conducting layers in suppressing thermal conductivity was quantified by performing real-space and modal (or frequency) analyses of phonon thermal conductivities in each layer type in Na_xCoO_2 and $Ca_3Co_4O_9$. The results revealed that, although most of the thermal energy is transported by the CoO_2 layers, phonon thermal conduction can be suppressed by increasing the vibrational anharmonicity in the layers adjacent to the CoO_2 layers. Differences in how the Na layers and Ca_2CoO_3 layers interfere with the phonon transport were also identified. From these insights it appears that further increases in anharmonicity in layered cobaltites and related classes of materials through tailoring of the non-conducting layers can result in increased *ZT* values and hence improved thermoelectric performance.

Intralayer Thermal Conduction

Table 1 reports overall thermal conductivities of Na_xCoO_2 ($x = 1.0, 0.5$) and $Ca_3Co_4O_9$ at 300 K in each crystallographic direction obtained from MD simulations. The out-of-plane thermal conductivities are lower than in-plane conductivities for all compounds, and the in-plane thermal conductivity decreases with decreasing Na content from $NaCoO_2$ to $Na_{0.5}CoO_2$, with an even lower value in the case of $Ca_3Co_4O_9$. These trends are in good agreement with experimental reports[23–26]. For example, the average of the calculated in-plane thermal conductivities of $NaCoO_2$ at 300 K is 43.97 W/mK, which is close to the experimentally measured in-plane thermal conductivity reported for Na_xCoO_2 ($x \approx 1$) of 37 W/mK[23]. In $Na_{0.5}CoO_2$, the average in-plane thermal conductivity at 300 K is 15.40 W/mK, which also compares well with the experimentally reported value of 16.5 W/mK (estimated using the Wiedemann-Franz law) for phonon thermal conductivity in single crystalline Na_xCoO_2[24]. In the case of $Ca_3Co_4O_9$, anisotropic phonon thermal conductivity has been reported to be 4.5 and 2.1 W/mK in the in-plane and out-of-plane directions, respectively[26], similar to values in this study of 6.92 and 3.32 W/mK in the corresponding directions. The good quantitative agreement gives us confidence that we can meaningfully examine the mechanism of phonon thermal conduction suppression in these materials using our classical MD model. Also, because electrons in layered cobaltites are transported within CoO_2 layers[24,26], in-plane phonon conduction is the most relevant with respect to optimising the thermoelectric conversion efficiency, so from here on we mainly focus on this aspect of phonon transport.

Table 1 also summarises the calculated thermal conductivities for each type of layer. The partial thermal conductivities are a measure of the contribution of each type of layer to the overall thermal conductivity, which is defined here as an extensive variable such that

$$\kappa_{\mathrm{overall}} = \kappa_{\mathrm{CoO_2}} + \kappa_{\mathrm{adj}},$$

where $\kappa_{\mathrm{CoO_2}}$ and κ_{adj} are the partial thermal conductivities of CoO_2 layers and the layers adjacent to them, respectively. The partial thermal conductivity of a particular layer depends on the volume ratio of the two types of layer, so to enable each type of layer's thermal conduction to be compared on the same basis we also define "layer" thermal conductivities $\kappa'_{\mathrm{CoO_2}}$ and κ'_{adj} to be the partial conductivities normalised by layer thickness (see Methods section for details).

The results in Table 1 show that CoO_2 layers exhibit a larger partial thermal conductivity than the adjacent layers in each of the three compounds. Even in $Ca_3Co_4O_9$, in which the Ca_2CoO_3 layers are thicker than CoO_2 layers, the latter account for more than 70% of $\kappa_{\mathrm{overall}}$. This indicates that in addition to electron transport, the CoO_2 layers also transfer the majority of the heat energy through these materials. From Table 1 it can also be seen that the overall thermal conductivities of $Na_{0.5}CoO_2$ and $Ca_3Co_4O_9$ are markedly lower than those of $NaCoO_2$. Even more notable is the drop in layer thermal conductivities of CoO_2 layers in $Na_{0.5}CoO_2$ and $Ca_3Co_4O_9$ (by roughly 57% and 75%, respectively) compared to $NaCoO_2$, which cannot be explained using a simple macroscopic model in which layer properties are independent of one another. The results thus indicate that increasing vibrational anharmonicity in the adjacent layers also lowers the thermal conductivity in the CoO_2 layers, confirming the importance of the non-conducting layers in modifying the overall thermal conductivity.

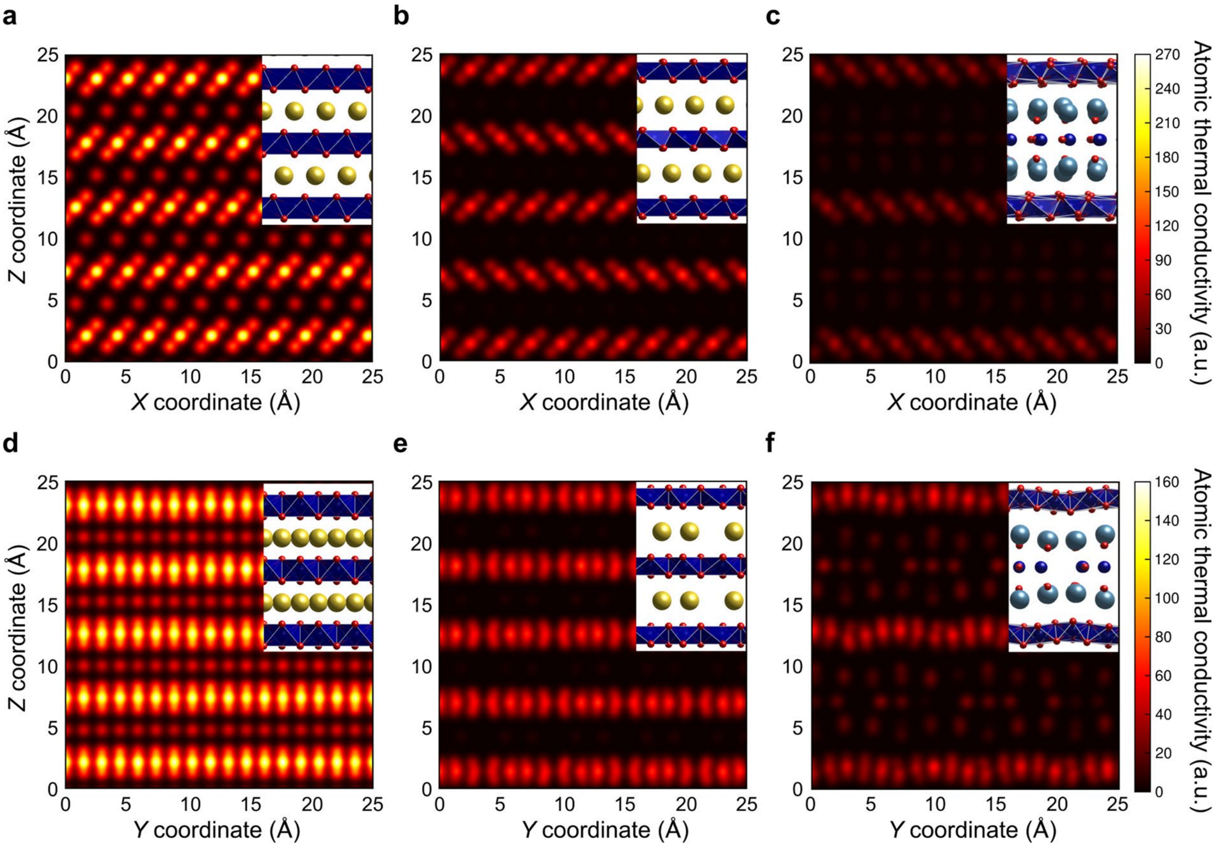

Figure 1. In-plane atomic thermal conductivities at 300 K. (**a–c**) Maps of *X* direction atomic thermal conductivities of **(a)** $NaCoO_2$, **(b)** $Na_{0.5}CoO_2$, and **(c)** $Ca_3Co_4O_9$ viewed down the *Y* direction. (**d–f**) Maps of *Y* direction atomic thermal conductivities of **(d)** $NaCoO_2$, **(e)** $Na_{0.5}CoO_2$, and **(f)** $Ca_3Co_4O_9$ viewed down the *X* direction. Note that the intensity range used in (**a–c**) is different to that used in (**d–f**). Crystal structures corresponding to each map are shown as insets, with yellow, light blue, dark blue and red balls representing Na, Ca, Co and O ions, respectively[43]. Blue polyhedra represent edge-sharing CoO_6 octahedral units.

The mechanism by which thermal conductivity is suppressed in the layered cobaltites can be gleaned better from the real-space analysis in Fig. 1, in which atomic thermal conductivities are visualised. Although phonon densities of CoO_2 layers might be expected to be similar in each material at the same temperature, consistent with the results in Table 1, Fig. 1 shows that the partial thermal conductivities of these layers are strongly influenced by the type of layer sandwiched between the CoO_2 layers, with the thicker but less heat-conductive rock-salt-type Ca_2CoO_3 layers more effective at suppressing κ_{CoO_2} than Na layers containing vacancies. Rébora *et al.* reported that the partial thermal conductivity of Ca_2CoO_3 layers is larger than that of CoO_2 layers, which is the opposite of our results[27]. This is possibly because they used LD within the harmonic approximation and assumed the phonon relaxation time to be constant. In our MD simulations, anharmonic thermal vibrations were included intrinsically on account of the atomic interaction model used. This anharmonicity results in a much lower partial thermal conductivity in the Ca_2CoO_3 layers than CoO_2 layers.

The mechanism by which Ca_2CoO_3 layers more effectively suppress phonon thermal conductivity is related to the incommensurate stacking of Ca_2CoO_3 and CoO_2 layers in $Ca_3Co_4O_9$. The lattice misfit introduces a strain that slightly displaces atoms in the CoO_2 layers from their equilibrium lattice sites[18–21], increasing the anharmonicity of their phonons. In earlier reports[28,29] we demonstrated that atomic vibrations invoked by lattice misfit dominate suppression of κ rather than static atomic displacements in the case of $Ca_3Co_4O_9$. Although the structure and composition of Na layers in Na_xCoO_2 ($x < 1$) are very different to those of Ca_2CoO_3 layers in $Ca_3Co_4O_9$, the misfit lattice strain appears to be the more effective mechanism for increasing phonon anharmonicity. To determine why this is so, we analysed the vibrational behaviour within layers adjacent to CoO_2 in the three systems in greater detail.

Anharmonic Vibrations in Layers Adjacent to CoO_2 Layers

Figure 2a shows a vibrational density plot for atoms in a single Na layer in $NaCoO_2$ projected onto the basal plane together with a representative three-dimensional isosurface of the vibrational density of a single Na atom in that layer (Fig. 2d). These vibrational densities conform to the curvature of the potential energy hypersurface around each atom. All the projections are circular in shape as the vibrational densities in this case are spherical, indicating that Na atoms vibrate uniformally about their equilibrium lattice positions in the defect-free system. Figure 2b,e show corresponding results for $Na_{0.5}CoO_2$, in which each Na layer contains 50% vacancies. In contrast to the

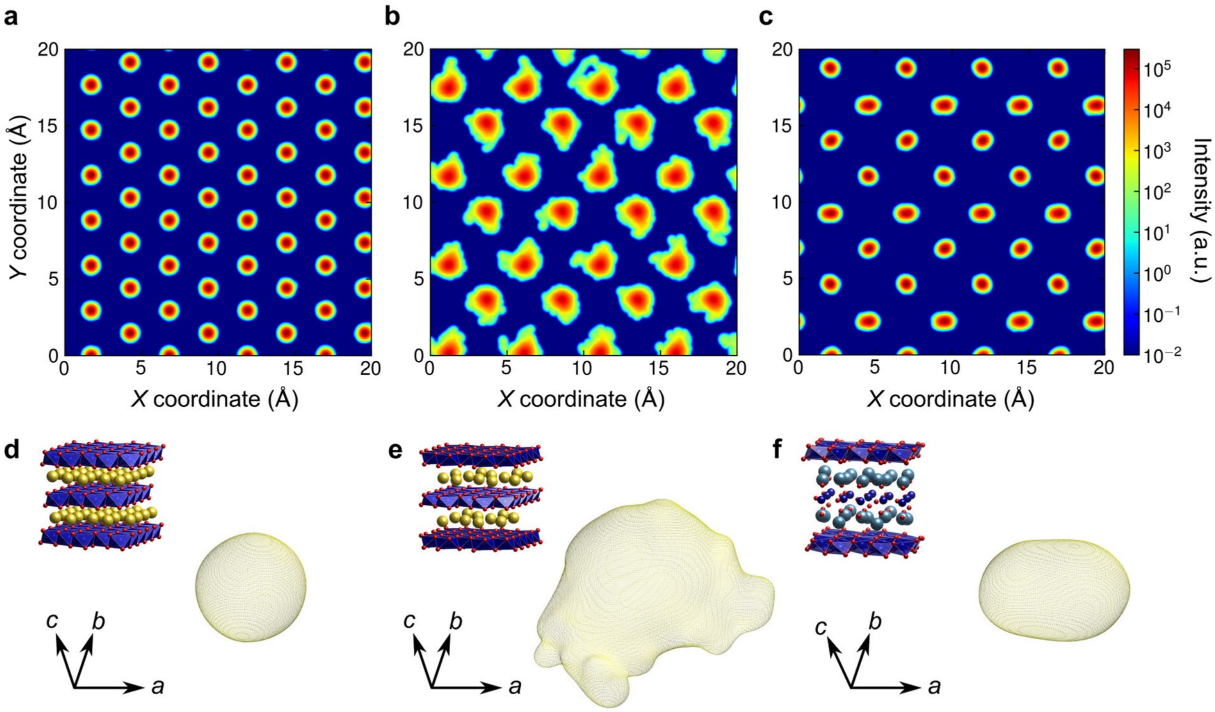

Figure 2. Vibrational density plots in layers adjacent to CoO_2 layers. **(a–c)**, Density plots of atom vibrational motion within **(a)** a single Na layer of $NaCoO_2$, **(b)** a single Na layer of $Na_{0.5}CoO_2$, and **(c)** a single Ca plane in a Ca_2CoO_3 layer of $Ca_3Co_4O_9$, projected onto their *ab* (basal) planes. (**d–f**), Example of density plot isosurfaces of **(d)** a single Na ion in $NaCoO_2$, **(e)** a single Na ion in $Na_{0.5}CoO_2$, and **(f)** a single Ca ion in $Ca_3Co_4O_9$. In **d**, **e** and **f**, the crystal structure of each cobaltite is shown in the upper left hand corner.

vacancy-free compound, the uneven isosurfaces in the case of Na atoms in $Na_{0.5}CoO_2$ reveal that their thermal vibrations are much more irregular and hence anharmonic.

Figures 2c,f show vibrational densities of Ca atoms in one Ca plane in one Ca_2CoO_3 layer of $Ca_3Co_4O_9$ projected onto the basal plane together with a representative three-dimensional isosurface of one of the Ca atoms. The density distributions appear relatively uniform compared with those of Na ions in $Na_{0.5}CoO_2$. However, unlike in $NaCoO_2$, there is considerable variety in the shapes of these isosurfaces, with some of them appearing distended in the *X* direction (ellipsoidal), even though the misfit direction is along the *Y* axis (see Supplementary Material Fig. S2 for details). This indicates that misfit between the two types of layers not only introduces a lattice strain but also causes the Ca atoms to vibrate anisotropically.

The intensities of the vibrational density plots are a response to the potential energy fields experienced by the atoms, and thus, within the harmonic approximation, the second derivative of the intensities is proportional to the atomic vibrational force constant. Figures 3a,b show the average second derivatives calculated for Na ions in $NaCoO_2$ and $Na_{0.5}CoO_2$, respectively, in the three principal directions as a function of distance from the equilibrium lattice position from −0.2 Å to 0.2 Å. When Na layers are vacancy-free, the second derivative is almost the same for all atoms with a narrow standard deviation. This means that, on average, the forces exerted on an Na atom by its neighbours are proportional to its distance from its equilibrium lattice position, i.e., Na vibrations in $NaCoO_2$ are close to being harmonic. Highly harmonic atom vibrations explain the high phonon thermal conductivity of $NaCoO_2$. In the case of $Na_{0.5}CoO_2$, the average second derivative of the Na vibrational density isosurface in the in-plane directions is approximately one third that of Na atoms in $NaCoO_2$. Moreover, the further from the equilibrium lattice position, the larger the standard deviation, indicative of greater anharmonicity. Atoms exhibiting this kind of vibration are often described as "rattlers", and their irregular thermal motion is associated with increased phonon scattering and hence lower phonon thermal conductivity[17].

The average second derivatives of the isosurfaces of Ca ions in $Ca_3Co_4O_9$ in each principal direction are plotted in Fig. 3c. In the *X* direction, the second derivative is highly asymmetric around the equilibrium lattice position and has a much larger standard deviation than in the other two directions (corresponding to large differences in the potential energy surfaces for *X* direction as shown in Fig. 2c). The vibrational motion in this direction is thus further from harmonic. Indeed, all atoms in Ca_2CoO_3 layers exhibit highly asymmetric vibrations. This irregular vibrational motion disturbs the motions of atoms in neighbouring CoO_2 layers, resulting in a lower phonon thermal conductivity for $Ca_3Co_4O_9$ even without introduction of point defects. Linking specific atomic vibration modes observed during MD with phonon modes calculated by lattice dynamics methods can provide further insights into thermal conductivity mechanisms and origins of anharmonicity, although for complex systems such as the cobaltites this is not always straightforward. In the case of $Ca_3Co_4O_9$, the anisotropic decrease in the average of the second derivatives of the potential energy surface in the negative *X* direction can be explained

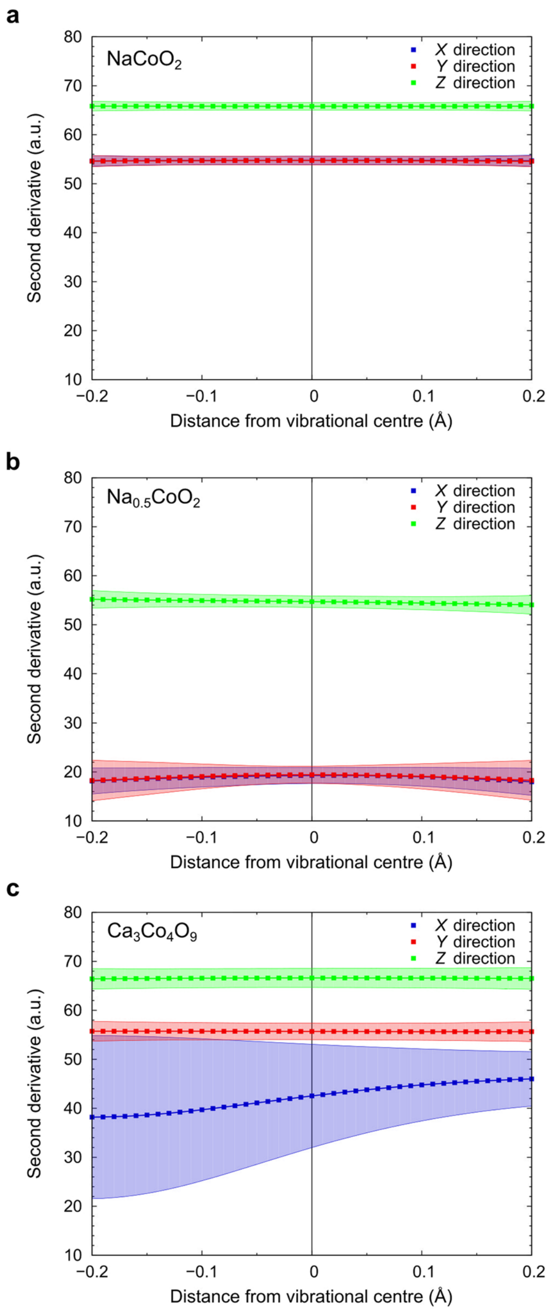

Figure 3. Potential energy second derivatives for cations in layers adjacent to CoO$_2$ layers. Mean potential energy second derivatives (proportional to force constants) and associated standard deviations (shaded regions) for **(a)** Na ions in NaCoO$_2$, **(b)** Na ions in Na$_{0.5}$CoO$_2$, and **(c)** Ca ions in Ca$_3$Co$_4$O$_9$ in in-plane (*X* and *Y*) and out-of-plane (*Z*) directions.

in terms of low-frequency floppy modes within the Ca$_2$CoO$_3$ layers. This approach is discussed in more detail in section S2 of Supplementary Material.

Our analyses show that the anharmonic vibrations in Na$_{0.5}$CoO$_2$ and Ca$_3$Co$_4$O$_9$ are very different to each other as a result of the different types of non-conducting layers separating the CoO$_2$ layers. In Na$_{0.5}$CoO$_2$, the in-plane force constants of Na atoms (corresponding to second derivatives) are small but almost constant. Because of the small force constants, Na atoms can vibrate freely to some extent, resulting in uneven potential energy surfaces and higher standard deviations from equilibrium lattice positions compared to NaCoO$_2$. In contrast, in Ca$_3$Co$_4$O$_9$ the in-plane force constants of Ca atoms are comparatively large (similar in magnitude to those in NaCoO$_2$) but asymmetric. The larger force constants in *Y* and *Z* directions constrain the vibrational densities to narrow bands, but the thermal vibrations in the *X* direction vary greatly, resulting in a large standard deviation from equilibrium lattice positions.

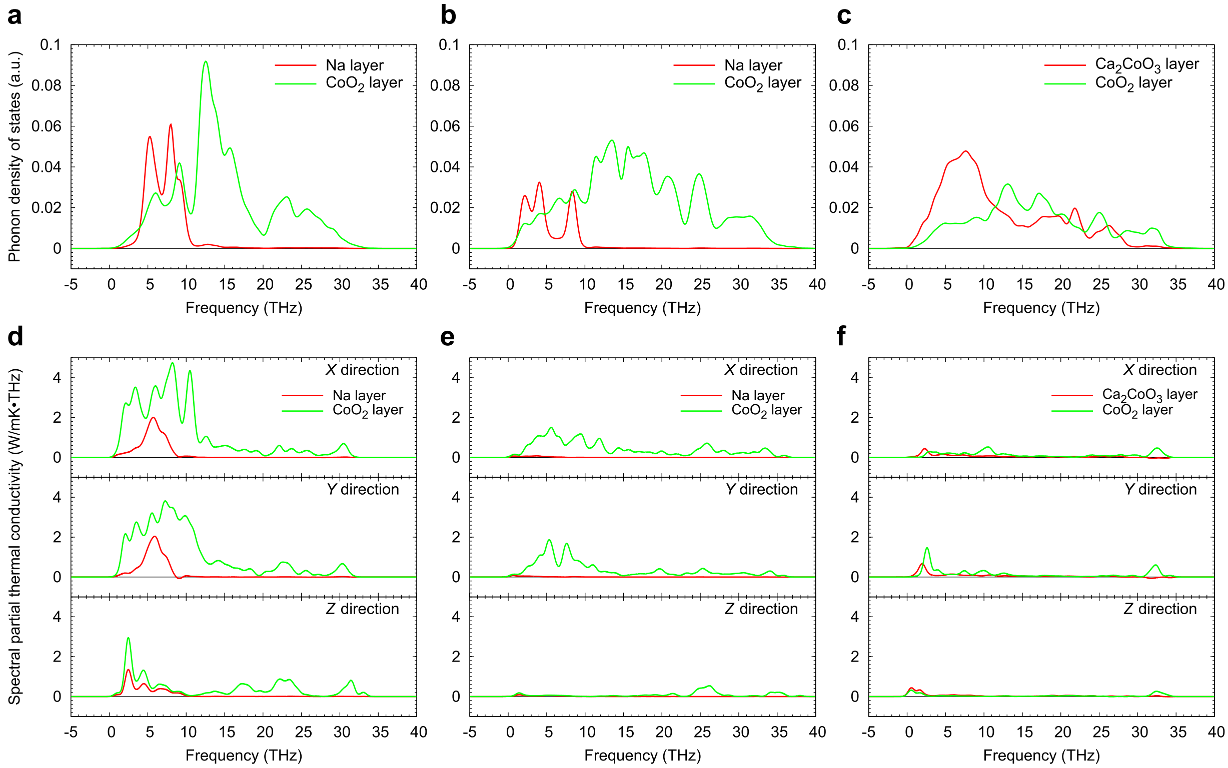

Figure 4. Phonon densities of states and spectral partial thermal conductivities at 300 K. **(a–c)**, Phonon density of states of layers in **(a)** $NaCoO_2$, **(b)** $Na_{0.5}CoO_2$, and **(c)** $Ca_3Co_4O_9$. **(d–f)**, Frequency dependence of partial thermal conductivity of each type of layer in **(d)** $NaCoO_2$, **(e)** $Na_{0.5}CoO_2$, and **(f)** $Ca_3Co_4O_9$ for in-plane (*X* and *Y*) and out-of-plane (*Z*) directions.

It is worth noting that our simulations may underestimate the degree of anharmonicity in these materials, since we employed simple two-body interatomic potentials that do not take into account subtle changes in electronic structure as bond distances lengthen and shorten during vibrational motion[30]. First-principles calculations may provide a more accurate picture of anharmonic vibration modes in these materials, but are much more computationally expensive. In real materials, atomic vibrations, and hence thermal conductivity, are also strongly affected by various crystalline defects, including impurity atoms, grain boundaries, surfaces, and so on, and thus can be expected to exhibit even greater variation than those observed in our model. Further experimental and computational work is needed to quantify the effects of crystalline defects on thermal conductivity in these layered cobaltites, including to what extent these features can be used to lower the thermal conductivity further.

Modal Analysis of Phonon Scattering

To determine which phonons are scattered by anharmonic thermal vibrations, we analysed the modal contributions to phonon thermal conductivity in each of the three compounds. Figure 4a,b and c show phonon densities of states (PDOSs) of each compound obtained from LD calculations using the same supercells as in the MD simulations. The partial thermal conductivities of each type of layer as a function of frequency are plotted in Fig. 4d,e and f (magnified views of these plots are shown in Fig. S4 of Supplementary Material). Figure 5 shows the frequency dependence of layer thermal conductivities for CoO_2 layers in each principal direction. Comparison of PDOSs and frequency dependent partial and layer thermal conductivities reveals which phonons are scattered and which remain heat-conductive.

PDOSs of CoO_2 layers do not exhibit significant differences between the three materials, in that they are all spread over a wide frequency range. PDOSs of Ca_2CoO_3 layers are also spread over a wide frequency range, while those of Na layers are confined to below 10 THz. In $NaCoO_2$, the partial thermal conductivity of the CoO_2 layers is high at relatively low frequencies compared with their PDOS. In the *Z* direction, spectral partial thermal conductivities of Na and CoO_2 layers show similar behaviour at low frequencies, indicating that vibrations in the two layers are strongly coupled. This leads to less scattering within each type of layer also, resulting in high phonon thermal conductivity in the out-of-plane direction.

In contrast to vacancy-free $NaCoO_2$, Na layers make almost no contribution to phonon thermal conductivity in $Na_{0.5}CoO_2$ because the thermal vibrations of Na atoms are strongly anharmonic. However, vibrations of CoO_2 layers can be seen to still be coupled with those of the Na ions because PDOSs of the two layer types overlap. Plots of spectral layer thermal conductivity in the in-plane directions in Fig. 5 show that accumulated layer thermal conductivities (measured from the areas under the curves) within CoO_2 layers in $Na_{0.5}CoO_2$ are about 66% less than those in $NaCoO_2$ below 15 THz and about 9% less above 15 THz compared. Thermal conductivity in CoO_2 layers is thus strongly suppressed at the lower frequencies over which Na atoms mostly vibrate when a high

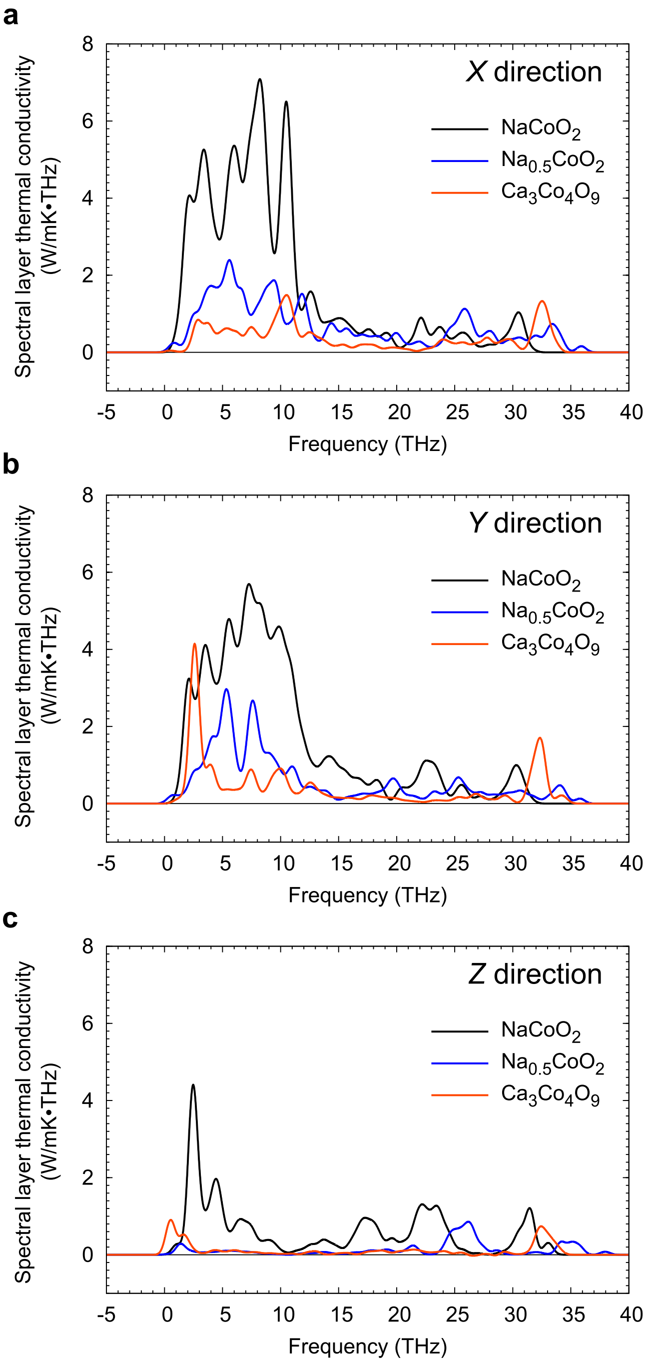

Figure 5. Frequency dependence of layer thermal conductivities of CoO_2 layers. **(a–c)** Layer thermal conductivities of CoO_2 layers in Na_xCoO_2 ($x=1.0$, 0.5) and $Ca_3Co_4O_9$ at 300 K in **(a)** *X*, **(b)** *Y*, and **(c)** *Z* directions as a function of frequency.

concentration of Na vacancies is introduced. The sum of the accumulated thermal conductivities below and above 15 THz is almost the same as that of the partial thermal conductivities of CoO_2 and adjacent layers in Table 1 (the differences are due to the different methods used to calculate the thermal conductivities).

The spectral partial thermal conductivity of CoO_2 layers in $Ca_3Co_4O_9$ is much lower than that in $Na_{0.5}CoO_2$ in all three directions. Figure 5 shows that not only are acoustic phonons strongly suppressed, but so also are the optical phonons at higher frequencies. Accumulated layer thermal conductivities within CoO_2 layers in the in-plane directions are about 81% smaller than those in $Na_{0.5}CoO_2$ below 15 THz and 40% smaller above 15 THz. This can be explained in terms of the large overlap up to ~30 THz in the PDOSs of CoO_2 and Ca_2CoO_3 layers, indicating that atomic vibrations within these layers interfere with each other over a wide frequency range. The anisotropic and irregular thermal vibrations of atoms in Ca_2CoO_3 layers are thus seen to disturb the thermal vibrations of atoms in the CoO_2 layers over a wider frequency range, suppressing the rate of phonon transport in these layers even more effectively than the Na layers in $Na_{0.5}CoO_2$.

Another interesting feature revealed by the plots in Fig. 5 is that the peaks in spectral layer thermal conductivities of CoO_2 layers in $Na_{0.5}CoO_2$ and $Ca_3Co_4O_9$ occur at different frequencies, suggesting that different phonon modes may suppress the thermal conductivity in CoO_2 layers by different amounts. By appropriate manipulation of the non-CoO_2 layers, e.g., through doping or making the layers thicker, it may be possible to "tune" the interference caused by phonon anharmonicity to the optimal frequency to minimise thermal conductivity. Such design strategies would also be greatly facilitated if the anharmonic vibrations observed during MD simulations could be connected particular phonon modes, e.g., through a combination of lattice dynamics and Boltzmann transport calculations. At present, however, such analysis is prohibitively expensive for these complex systems, especially since decomposing the overall thermal conductivities calculated from perturbed MD into heat capacities, group velocities and relaxation times is a non-trivial task.

In summary, overall, partial and layer thermal conductivities of layered cobaltites Na_xCoO_2 ($x = 1.0$ and 0.5) and $Ca_3Co_4O_9$ calculated using perturbed MD confirmed that CoO_2 layers transport most of the thermal energy in these materials. In $Na_{0.5}CoO_2$ and $Ca_3Co_4O_9$, phonon thermal conduction in CoO_2 layers is suppressed by anharmonicity in the thermal vibrations of cations in their neighbouring layers. Quantitative analysis of the atomic vibrations revealed differences in the anharmonic behaviour of the non-CoO_2 layers in $Ca_3Co_4O_9$ to those in Na_xCoO_2. Scattered phonons and heat-conductive phonons were identified by modal analysis using perturbed MD in conjunction with LD. In $Ca_3Co_4O_9$, not only acoustic phonons but also optical phonons are strongly suppressed compared with $Na_{0.5}CoO_2$ because of the incommensurate stacking of alternating layers, resulting in the lowest thermal conductivity of the three systems examined. These insights suggest that thermal conductivities of layered oxides can be lowered further without compromising their electronic properties by manipulating the amount of anharmonicity in the non-CoO_2 layers. The same method can also be used to examine alternative ways of introducing and manipulating anharmonicity in oxide and non-oxide materials to accelerate the development of high efficiency thermoelectric energy conversion systems.

Methods

Model construction. Reported crystal structures determined using x-ray diffraction[31] and electron diffraction[32] were taken as the initial crystal structures for α–$NaCoO_2$ and γ–$Na_{0.5}CoO_2$, respectively. To maintain charge neutrality upon introduction of Na^+ vacancies in $Na_{0.5}CoO_2$, half the Co^{3+} ions were changed to Co^{4+} ions. The lowest energy configuration of Na, Co^{3+} and Co^{4+} ions was determined by performing systematic static lattice calculations using the General Utility Lattice Program (GULP) code[33]. The positions of Na ions in the optimized structure were found to be in good agreement with results of electron diffraction studies[32,34], although they are shifted slightly because Coulombic repulsion between Na^+ and $Co^{3+/4+}$ ions is overestimated in our model on account of the use of formal charges for the ions.

For $Ca_3Co_4O_9$, the model of composition $(Ca_2CoO_3)_{3/5}CoO_2$ (CCO) reported by Rébora *et al.* was used as the initial crystal structure[15]. The lowest energy configuration of Co^{3+} and Co^{4+} ions was determined by carrying out first-principles calculations using the Vienna Ab initio Simulation Package (VASP)[35]. This configuration was confirmed to be the most stable by performing static lattice calculations using the GULP code[33]. Details are reported elsewhere[28].

Supercells of Na_xCoO_2 and CCO were geometrically optimised using GULP before performing MD and LD simulations. Buckingham potential parameters for Na_xCoO_2 reported by Tada *et al.*[30], for O^{2-}-O^{2-} reported by Cherry *et al.*[36], and for Ca^{2+}-O^{2-} reported by Zacate *et al.*[37] were employed. Supercell sizes used in MD simulations were $31 \times 29 \times 31$ Å^3, $30 \times 29 \times 34$ Å^3 and $25 \times 28 \times 44$ Å^3 for $NaCoO_2$, $Na_{0.5}CoO_2$ and CCO, respectively.

Analysis of atomic vibrations. To calculate the lattice constants of the cobaltites at 300 K, MD simulations were carried out in the NPT ensemble for 100 ps with a time step of 1 fs using the Large-scale Atomic/Molecular Massively Parallel Simulator (LAMMPS) code[38]. Next, structural relaxation in the NVT ensemble was performed for an initial 100 ps using temperature scaling and 300 ps using the Nosé-Hoover thermostat to ensure the atoms had reached thermal equilibrium.

Atom positions were recorded during the main production run of 300 ps following structural relaxation. Plots of vibrational density, which follows the curvature of the potential energy hypersurfaces around each atom, were generated by superimposing a Gaussian function on the accumulated atom positions using two- or three-dimensional grids with a mesh size of 0.02 Å. Second derivatives of the density plot intensities (which are proportional to the force constant) at each point were also calculated in each direction using a central difference method. The vibrational centre of each atom was taken to be the grid point whose vibrational density was highest among the points over which the atom vibrated. We used the Gaussian function $G(x, y, \sigma) = \frac{1}{2\pi\sigma^2}\exp(-\frac{x^2+y^2}{2\sigma^2})$ for two-dimensional density plots, and $G(x, y, \sigma) = \frac{1}{(2\pi)^{3/2}\sigma^2}\exp(-\frac{x^2+y^2+z^2}{2\sigma^2})$ for three-dimensional density plots. Before calculating second derivatives, the natural logarithm of each intensity curve was calculated, as the Gaussian function contains an exponential term. Average second derivatives and standard deviations were calculated from the values of all ions of the same element within a single MD run. The number of ions was 720 and 360 for Na in $NaCoO_2$ and $Na_{0.5}CoO_2$, respectively, and 480 for Ca in CCO.

Perturbed molecular dynamics. Phonon thermal conductivities were calculated using the perturbed MD method[22]. The LAMMPS code was modified for this purpose. In this method, phonon thermal conductivity in the *X* direction is calculated according to

$$\kappa = \frac{1}{F_{\text{ext}}T}\lim_{t\to\infty}\langle J_X\rangle_t, \tag{1}$$

where F_{ext} is the magnitude of the perturbation in the X direction, T is temperature and J_X is the heat flux in the X direction. The heat flux, J_X, is slightly enhanced by the perturbation and proportional to the magnitude of the perturbation within the linear response regime. This cancels out the $1/F_{\text{ext}}$ term so that the calculated phonon thermal conductivity is independent of F_{ext}. According to Irving and Kirkwood[39], the microscopic heat flux $\mathbf{J}$ is given by the summation of atomic contributions $\mathbf{J}_i$,

$$\mathbf{J} = \sum_i \mathbf{J}_i = \sum_i \frac{1}{2V}\left[\left\{m_i \mathbf{v}_i^2 \mathbf{I} + \sum_j \phi_{ij}\mathbf{I}\right\}\mathbf{v}_i - \sum_j (\mathbf{F}_{ij}\cdot\mathbf{v}_i)\mathbf{r}_{ij}\right], \tag{2}$$

where V is the volume of the supercell, m_i is the mass of atom i, $\mathbf{v}_i$ is the velocity of atom i, ϕ_{ij} is the internal energy resulting from interaction between atoms i and j, $\mathbf{I}$ is a unit tensor of second rank, and $\mathbf{F}_{ij}$ is the force exerted by atom j on atom i. The overall thermal conductivity κ is given by the sum of atomic thermal conductivities κ_i according to

$$\kappa = \sum_i \kappa_i = \sum_i \frac{1}{F_{\text{ext}}T} \lim_{t\to\infty} \langle J_{i,X}\rangle_t, \tag{3}$$

By summing heat fluxes over atoms in each layer separately, each layer's contribution to the overall thermal conductivity can be evaluated. However, the partial thermal conductivities of $\mathrm{CoO_2}$ layers cannot be simply compared between different cobaltites because atomic contributions may differ depending on the volume of the supercell (or volume ratio between the two types of layer) which is used in eq. (2). In this case, each partial thermal conductivity needs to be scaled by the ratio of layer thicknesses according to

$$\kappa'_{\mathrm{CoO_2}} = \frac{d_{\mathrm{CoO_2}} + d_{\text{adj}}}{d_{\mathrm{CoO_2}}} \kappa_{\mathrm{CoO_2}} \tag{4}$$

and

$$\kappa'_{\text{adj}} = \frac{d_{\mathrm{CoO_2}} + d_{\text{adj}}}{d_{\text{adj}}} \kappa_{\text{adj}}, \tag{5}$$

where $d_{\mathrm{CoO_2}}$ and d_{adj} are the thicknesses of a $\mathrm{CoO_2}$ layer and an adjacent layer in a given structure, and we refer to $\kappa'_{\mathrm{CoO_2}}$ and κ'_{adj} as layer thermal conductivities. The thickness of each layer is defined such that the boundary between two layers is midway between the average position of O ions in a $\mathrm{CoO_2}$ layer and the average position of Na or Ca ions in an adjacent layer in the Z direction.

Thermal conductivity calculations. After achieving thermal equilibrium, perturbed MD simulations were carried out for 1.1 ns. The first 0.1 ns was the time needed for energy fluctuations caused by the perturbation to relax. The average heat fluxes of all constituent atoms were calculated using the last 1.0 ns of data, from which phonon thermal conductivities were derived. More than four different simulations were performed with perturbations of different magnitude within the linear response regime for each cobaltite to obtain an average thermal conductivity and calculate its standard deviation. The atomic thermal conductivities in Fig. 1 were standardised by multiplying by the cross-sectional areas of their supercells perpendicular to the direction of interest in order to facilitate comparison of maps of different sized systems.

Modal analysis. According to the Green-Kubo modal analysis method developed by Lv and Henry[40], we can project atomic trajectories from MD onto the modes from LD. The modal contributions to the velocity of each atom, $\mathbf{v}_i(n)$, can be obtained from the time derivative of the amplitude of normal mode, $\dot{X}(n)$, as

$$\mathbf{v}_i = \sum_n \mathbf{v}_i(n) = \sum_n \frac{1}{\sqrt{m_i}} \mathbf{p}_i(n)\dot{X}(n) \tag{6}$$

where $\mathbf{p}_i(n)$ is the eigenvector of atom i in mode n[40,41]. Thus we can obtain modal contributions $\mathbf{J}(n)$ to the microscopic heat flux such that

$$\mathbf{J} = \sum_n \mathbf{J}(n) = \sum_n \sum_i \mathbf{J}_i(n) = \sum_n \sum_i \frac{1}{2V}\left[\left\{m_i \mathbf{v}_i^2 \mathbf{I} + \sum_j \phi_{ij}\mathbf{I}\right\}\mathbf{v}_i(n) - \sum_j (\mathbf{F}_{ij}\cdot\mathbf{v}_i(n))\mathbf{r}_{ij}\right] \tag{7}$$

where $\mathbf{J}_i(n)$ are atomic modal contributions to this flux. In this study, we substituted eq. (7) into eq. (1) instead of using the Green-Kubo expression. With this method, modal or frequency dependencies of overall, atomic, partial, and layer thermal conductivities can be analysed simply from the time average of modal contributions to the heat flux.

LD calculations were performed to obtain normal mode eigenvalues (phonon frequencies), eigenvectors at the gamma point and phonon densities of states of the supercells, using the Phonopy code[42]. The eigenvectors were then read into MD simulations, and calculations of modal thermal conductivity were carried out with one perturbation for each cobaltite system. The calculation procedure used was the same as that described under *Thermal conductivity calculations* except that the time under perturbation was set to 5.1 ns instead of 1.1 ns to improve the statistical accuracy. Further details about the method used to calculate thermal conductivities are given in section S1 of Supplementary Material, and the method of assigning of anharmonic vibrations in CCO to particular phonon modes in section S2.

References

1. Snyder, G. J. & Toberer, E. S. Complex thermoelectric materials. *Nat. Mater.* **7**, 105–114 (2008).
2. Zhao, L.-D. *et al.* Ultralow thermal conductivity and high thermoelectric figure of merit in SnSe crystals. *Nature* **508**, 373–377 (2014).
3. Morelli, D. T., Jovovic, V. & Heremans, J. P. Intrinsically minimal thermal conductivity in cubic I-V-VI2 semiconductors. *Phys. Rev. Lett.* **101**, 035901 (2008).
4. He, J. & Tritt, T. M. Advances in thermoelectric materials research: Looking back and moving forward. *Science* **357**, eaak9997 (2017).
5. Terasaki, I., Sasago, Y. & Uchinokura, K. Large thermoelectric power in $NaCo_2O_4$ single crystals. *Phys. Rev. B* **56**, R12685–12687 (1997).
6. Funahashi, R. *et al.* An oxide single crystal with high thermoelectric performance in air. *Jpn. J. Appl. Phys.* **39**, L1127–1129 (2000).
7. Funahashi, R. & Shikano, M. $Bi_2Sr_2Co_2O_y$ whiskers with high thermoelectric figure of merit. *Appl. Phys. Lett.* **81**, 1459–1461 (2002).
8. Koumoto, K., Terasaki, I. & Funahashi, R. Complex oxide materials for potential thermoelectric applications. *MRS Bull.* **31**, 206–210 (2006).
9. Wang, Y. *et al.* Spin entropy as the likely source of enhanced thermo power in Na_xCoO_2. *Nature* **423**, 425–428 (2003).
10. Takeuchi, T. *et al.* Contribution of electronic structure to the large thermoelectric power in layered cobalt oxides. *Phys. Rev. B* **69**, 125410 (2004).
11. Koshibae, W., Tsutsui, W. & Maekawa, S. Thermopower in cobalt oxide. *Phys. Rev. B* **62**, 6869–6871 (2000).
12. Kuroki, K. & Arita, R. "Pudding mold" band drives large thermopower in Na_xCoO_2. *J. Phys. Soc. Jpn.* **76**, 083707 (2007).
13. Singh, D. J. Electronic structure of $NaCo_2O_4$. *Phys. Rev. B* **61**, 13397 (2000).
14. Xiang, H. J. & Singh, D. J. Suppression of thermopower of Na_xCoO_2 by an external magnetic field: Boltzmann transport combined with spin-polarized density functional theory. *Phys. Rev. B* **76**, 195111 (2007).
15. Rébola, A. *et al.* First-principles study of the atomic and electronic structures of misfit-layered calcium cobaltite $(Ca_2CoO_3)(CoO_2)_{1.62}$ using rational approximants. *Phys. Rev. B* **85**, 155132 (2012).
16. Baran, J. D. *et al.* Tuning Thermoelectric Properties of Misfit Layered Cobaltites by Chemically Induced Strain. *J. Phys. Chem. C* **119**, 21818–21827 (2015).
17. Voneshen, D. J. *et al.* Suppression of thermal conductivity by rattling modes in thermoelectric sodium cobaltate. *Nature Mater.* **12**, 1028–1032 (2012).
18. Wu, L. *et al.* Origin of phonon glass-electron crystal behavior in thermoelectric layered cobaltate. *Adv. Funct. Mater.* **23**, 5728–5736 (2013).
19. Miyazaki, Y. *et al.* Modulated structure of the thermoelectric compound $[Ca_2CoO_3]_{0.62}CoO_2$. *J. Phys. Soc. Jpn.* **71**, 491–497 (2002).
20. Lambert, S., Leligny, H. & Grebille, D. Three Forms of the Misfit Layered Cobaltite $[Ca_2CoO_3]$ $[CoO_2]_{1.62}$·A 4D Structural Investigation. *J. Solid State Chem.* **160**, 322–331 (2001).
21. Muguerra, H., Grebille, D. & Bourée, F. Disordered misfit $[Ca_2CoO_3][CoO_2]_{1.62}$ structure revisited via a new intrinsic modulation. *Acta Cryst., Sect. B: Struct. Sci.* **64**, 144–153 (2008).
22. Yoshiya, M. *et al.* Perturbed molecular dynamics for calculating thermal conductivity of zirconia. *Mol. Simul.* **30**, 953–961 (2004).
23. Lee, M. *et al.* Large enhancement of the thermopower in Na_xCoO_2 at high Na doping. *Nat. Mater.* **5**, 537–540 (2006).
24. Fujita, K., Mochida, K. & Nakamura, K. High-temperature thermoelectric properties of $Na_xCoO_{2-\delta}$ single crystals. *Jpn. J. Appl. Phys.* **40**, 4644–4647 (2001).
25. Shikano, M. & Funahashi, R. Electrical and thermal properties of single-crystalline $(Ca_2CoO_3)_{0.7}CoO_2$ with a $Ca_3Co_4O_9$ structure. *Appl. Phys. Lett.* **82**, 1851–1853 (2003).
26. Kenfaui, D. *et al.* Development of multilayer textured $Ca_3Co_4O_9$ materials for thermoelectric generators: Influence of the anisotropy on the transport properties. *J. Eur. Ceram. Soc.* **32**, 2405–2414 (2012).
27. Rébola, A. *et al.* Phonon and thermal transport properties of the misfit-layered oxide thermoelectric $Ca_3Co_4O_9$ from first principles. *Appl. Phys. Lett.* **104**, 251910 (2014).
28. Fujii, S. *et al.* Impact of dynamic interlayer interactions on thermal conductivity of $Ca_3Co_4O_9$. *J. Electron. Mater.* **43**, 1905–1915 (2014).
29. Fujii, S. & Yoshiya, M. Manipulating thermal conductivity by interfacial modification of misfit-layered cobaltites $Ca_3Co_4O_9$. *J. Electron. Mater.* **45**, 1217–1226 (2016).
30. Tada, M., Yoshiya, M. & Yasuda, H. Derivation of interatomic potentials from *Ab-initio* calculations for molecular dynamics simulations of Na_xCoO_2. *Trans. Mater. Res. Soc. Jpn.* **35**, 205–208 (2010).
31. Takahashi, Y., Gotoh, Y. & Akimoto, J. Single-crystal growth, crystal and electronic structure of $NaCoO_2$. *J. Solid State Chem.* **172**, 22–26 (2003).
32. Huang, Q. *et al.* Low temperature phase transitions and crystal structure of $Na_{0.5}CoO_2$. *J. Phys.: Condens. Matter* **16**, 5803–5814 (2004).
33. Gale, J. D. GULP: A computer program for the symmetry-adapted simulation of solids. *J. Chem. Soc., Faraday Trans.* **97**, 629–637 (1997).
34. Zandbergen, H. W. Sodium ion ordering in Na_xCoO_2: Electron diffraction study. *Phys. Rev. B.* **70**, 024101 (2004).
35. Kresse, G. & Hafner, J. *Ab initio* molecular dynamics for liquid metals. *Phys. Rev. B* **47**, 558–561 (1993).
36. Cherry, M., Islam, M. S. & Catlow, C. R. A. Oxygen Ion Migration in Perovskite-Type Oxides. *J. Solid State Chem.* **118**, 125–132 (1995).
37. Zacate, M. O. & Grimes, R. W. Intrinsic defect processes in Ca-Al-Fe-O cement-phase compounds. *J. Mater. Sci.* **34**, 445–449 (1999).
38. Plimpton, S. Fast parallel algorithms for short-range molecular-dynamics. *J. Comput. Phys.* **117**, 1–19 (1995).
39. Irving, J. H. & Kirkwood, G. The statistical mechanical theory of transport processes. IV. The equations of Hydrodynamics. *J. Chem. Phys.* **18**, 817–829 (1950).
40. Lv, W. & Henry, A. Direct calculation of modal contributions to thermal conductivity via Green-Kubo modal analysis. *New J. Phys.* **18**, 013028 (2016).
41. Dove, M. T. *Introduction to Lattice Dynamics*. (Cambridge University Press, 1993).
42. Togo, A. & Tanaka, I. First principles phonon calculations in materials science. *Scripta Mater.* **108**, 1–5 (2015).
43. Momma, K. & Izumi, F. VESTA 3 for three-dimensional visualization of crystal, volumetric and morphology data. *J. Appl. Crystallogr.* **44**, 1272–1276 (2011).

Acknowledgements

This work was supported by the Grant-in-Aid for Scientific Research on Innovative Areas 'Nano Informatics' (grant no. 25106005) from the Japan Society for the Promotion of Science (JSPS), and also by a Grant-in-Aid for JSPS Fellows (grant no. 15J00489).

Author Contributions

S.F. and M.Y. designed the study. S.F. performed the calculations. S.F., M.Y., C.A.J.F. interpreted the results and wrote the manuscript.

Additional Information

Supplementary information accompanies this paper at https://doi.org/10.1038/s41598-018-29259-z.

Competing Interests: The authors declare no competing interests.

Acta Materialia 171 (2019) 154–162

Contents lists available at ScienceDirect

Acta Materialia

journal homepage: www.elsevier.com/locate/actamat

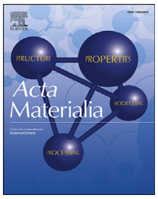

Full length article

Atomistic mechanisms of thermal transport across symmetric tilt grain boundaries in MgO

Susumu Fujii [a], Tatsuya Yokoi [a, b], Masato Yoshiya [a, c, *]

[a] Department of Adaptive Machine Systems, Osaka University, 2-1 Yamadaoka, Suita, Osaka 565-0871, Japan
[b] Department of Materials Science and Engineering, Nagoya University, Furo-chou, Chikusa, Nagoya, 464-8603, Japan
[c] Nanostructures Research Laboratory, Japan Fine Ceramics Center, 2-4-1 Mutsuno, Atsuta, Nagoya, 456-8587, Japan

ARTICLE INFO

Article history:
Received 10 September 2018
Received in revised form
10 January 2019
Accepted 5 April 2019
Available online 10 April 2019

Keywords:
Grain boundary
Thermal conductivity
Magnesium oxide (MgO)
Phonon transport
Molecular dynamics

ABSTRACT

Grain boundaries often have a decisive effect on the macroscopic properties of polycrystalline materials, but the wide variety of their atomic structures, interfacial lengths, and compositions makes them difficult to characterize all-encompassingly. An indispensable example in which an understanding of the relationship between grain boundary structures and properties would greatly facilitate development of superior materials is thermal transport, especially with respect to microstructure evolution, thermoelectrics and thermal barrier coatings. To contribute to a more comprehensive understanding, we performed a systematic study of lattice thermal conduction across a wide range of symmetric tilt grain boundaries in MgO using perturbed molecular dynamics. It was found that thermal conductivities vary significantly with grain boundary structure but are strongly correlated with excess volume, which is a measure of the number density of atoms in the vicinity of the grain boundary planes. Real-space analysis revealed that dislocation densities determine the phonon transport paths and thermal conductivity in low-angle boundaries whereas it is the amount of open volume rather than the shape of structural units in high-angle boundaries that determine thermal conductivity. We also found that low-angle boundaries mainly reduce phonon transports at low frequencies whereas high-angle boundaries also reduce it at intermediate and high frequencies effectively, regardless of the shape of structural units. These insights are expected to be applicable to other close-packed oxide systems, and should aid the design of next-generation thermal materials through tailoring of grain boundaries.

1. Introduction

Grain boundaries (GBs) can be defined as homogeneous interfaces between crystallites in a polycrystalline material, and are thus a form of two dimensional defect. An essentially infinite number of atomic configurations are possible depending on the microstructure which can be more quantitatively characterized by the sizes and shapes of the grains, the misorientation between them, and their thermodynamic state. As it is extensively studied and well known for metals, GBs are often interpreted as infinite arrays of dislocations or in terms of structural units [1,2,3,4,5]. Recent studies have shown that properties such as oxygen diffusion [6,7], electrical conductivity [8,9,10] and thermal diffusivity [11] of individual GBs vary significantly; GB properties are also often the dominant factor determining the macroscopic properties of a material. One of the major goals of materials science is to develop a detailed understanding of grain boundary structure-property relationships so that materials properties or microstructures behind them can be optimized through tailoring of GB chemistry and structure.

Thermal conductivity is a property critical not only for microstructure evolution but also for many technologically important applications such as microelectronics [12], high-power electronic devices [13], thermoelectrics [14,15], and thermal barrier coatings [16,17] that is known to be affected strongly by the nature and distribution of GBs. For example, nanocrystalline materials have been designed with high GB densities to achieve extremely low lattice thermal conductivities in a number of different materials [14,15,17,18,19]. In most cases, however, the atomic-level mechanisms behind the increased thermal resistance have not been examined in detail.

---

[*] Corresponding author. Department of Adaptive Machine Systems, Osaka University, 2-1 Yamadaoka, Suita, Osaka, 565-0871, Japan.
E-mail address: yoshiya@ams.eng.osaka-u.ac.jp (M. Yoshiya).

https://doi.org/10.1016/j.actamat.2019.04.009
1359-6454/

According to kinetic theory [20], lattice thermal conductivity, κ_{lattice}, is given by the summation of all phonon modes,

$$\kappa_{\text{lattice}} = \frac{1}{3}\sum_{\text{mode}}\int C_V(\omega)v(\omega)^2\tau(\omega)\mathrm{d}\omega = \frac{1}{3}\sum_{\text{mode}}\int C_V(\omega)v(\omega)\Lambda(\omega)\mathrm{d}\omega, \tag{1}$$

where, C_V, v, τ, ω and Λ are the spectral heat capacity, group velocity, relaxation time, phonon frequency, and mean free path of phonons, respectively. Decreases in lattice thermal conductivity by GB scattering can be attributed to a decrease in Λ, assuming that Λ corresponds to the average grain size and is independent of phonon frequencies and the nature of the GBs [17,21,22]. This first-order approximation enables lattice thermal conductivity to be estimated from the average grain size, and thus the degree of nanostructuring by a given amount [23]. However, many studies have reported that interfacial thermal conductance (or conversely resistance) across GBs strongly depends on the nature (structure and chemistry) of the GBs. For instance, interfacial thermal resistances across three twist GBs in Al_2O_3 were measured experimentally and found to differ by a factor of 3 [11].

Computational simulations have also been carried out for many materials such as silicon [24,25], diamond [26], graphene [27,28], and various oxides [29,30,31] using non-equilibrium molecular dynamics (MD) methods. These revealed that, in general, interfacial thermal resistance (a) increases with misorientation angle before plateauing out at high angles [25,29], and (b) increases linearly with GB energy [26,29,31]. Such systematic investigations of a large variety of GB structures are helpful for understanding overall trends in structure-property relationships, specifically interfacial thermal conduction. Investigations into the underlying scattering mechanisms at different GBs, however, remain limited. With the exception of recent studies of interfacial thermal resistances of two types of dislocations in low-angle GBs [28] and demonstrations of the importance of disordered structures at GBs [30,32], the impact of the fundamental building blocks of GBs, namely, dislocation cores and structural units, on interfacial thermal resistances have not yet been investigated systematically.

Equation (1) shows that lattice thermal conduction across GBs also depends on phonon frequency. One method used over the last few decades to investigate the frequency dependence of thermal conduction through GBs is to calculate phonon energy transmissivity using the wave packet method [24,30,33,34]. Such calculations have shown that transmission coefficients tend to decrease with increasing phonon frequency. This is consistent with an experimental study of nanocrystalline silicon showing that the temperature dependence of its lattice thermal conductivity can be understood in terms of frequency-dependent mean free paths, Λ [15]. One important issue, however, is that the wave packet method assumes that the system contains no other phonons except for an incident phonon wave packet; in other words, no phonon-phonon scattering is included in such simulations [24,35]. This results in underestimation of the degree of phonon scattering because anharmonicity is significant at finite temperature [30].

In this study, we analyze lattice thermal conduction across various symmetric tilt GBs (STGBs) in a model material, MgO, using the perturbed MD method [36]. We chose MgO because of the following reasons: (a) its GB structures were well characterized and relatively simple in comparison with wide spectrum of materials due to its highly ionic bonding, (b) the GB structures can be readily compared with face-centered-cubic (FCC) metals as both Mg and O atoms form FCC sublattices, (c) the gained insights from MgO may be applied to the oxides which also have FCC sublattice, e.g., rock salt, zinc blende, fluorite (ZrO_2), and perovskite ($SrTiO_3$), (d) the impact of GBs on lattice thermal conductivity is readily estimated due to the high thermal conductivity of single crystalline MgO. The effective thermal conductivity, κ_{eff}, defined as the overall lattice thermal conductivity through grain interiors and GBs, was calculated instead of interfacial thermal resistance because intragranular thermal conductivity is also changed in nanocrystalline materials, so that attributing this decrease to interfacial thermal resistance alone may be misleading [32].

Our systematic calculations of effective thermal conductivities of more than 80 types of STGBs in MgO reveal a strong correlation with the magnitude of excess volume at a GB rather than its excess energy. The underlying phonon transport mechanisms across the STGBs are also identified through real-space analyses of lattice thermal conductivity. We also calculate frequency-dependent thermal conductivity in several STGBs using perturbed MD in conjunction with lattice dynamics (LD) simulations, which includes all anharmonic effects [37]. The insights suggest that lattice thermal conduction can be controlled effectively by tailoring micro- or nanostructures such that GBs with the appropriate excess volume occur in appropriate concentrations.

2. Simulation methods

2.1. GB model construction

Eighty-one MgO STGBs were generated by rotating two crystals about their [001], $[1\bar{1}0]$, [111], [112], $[2\bar{1}0]$ or $[3\bar{1}0]$ axes for a wide range of misorientation angles. Stable atomic configurations of these STGBs were obtained using simulated annealing (SA) techniques (schematically described in our previous paper [38]). In each case, an initial configuration was constructed by sandwiching a disordered structure (generated by performing a separate MD simulation of single crystal MgO at $T = 8000$ K for 20 ps with a time step of 1 fs) between two crystal slabs under three dimensional periodic boundary conditions. Slab widths perpendicular to the GB planes were about 60 Å. In order to avoid a rapid pressure increase upon expansion of the disordered structure during relaxation, the starting model was manually expanded by a few percent in each principal direction.

SA simulations commenced in the NVT ensemble at 4000 K. An NPT ensemble was then used to optimize both the atomic positions and lattice constants, decreasing T in a stepwise manner in intervals of $\Delta T = 250$ K (for 2000 K $\leq T$) and 500 K (for 1000 K $\leq T \leq$ 2000 K). During the process, atomic diffusion was sufficiently promoted by thermal energy, and atoms in the disordered structure spontaneously became ordered to decrease the lattice energy in the vicinity of GB planes. Rigid-body translations could also be spontaneously occurred, and the microscopic degrees of freedom, thus, were fully taken into account in the simulations [39]. Obtained structures were then annealed at 100 K and then at 50 K, and the final instantaneous atom arrangement at 50 K was optimized by performing an energy minimization calculation using the General Utility Lattice Program (GULP) [40]. Holding times at each temperature were set at 30 ps (for 1500 K $< T \leq$ 4000 K) and 15 ps (for $T \leq$ 1500 K).

SA simulations were performed 10 times for each STGB using different initial velocity distributions to determine the most stable atomic arrangement (lowest GB energy). To determine equilibrium lattice constants of the STGB models at 300 K, MD simulations were then performed in the NPT ensemble for 100 ps. After fixing the lattice constants, structural relaxation in the NVT ensemble was carried out for 100 ps using temperature scaling and 300 ps using a Nosé-Hoover thermostat to achieve thermal equilibrium. All MD simulations in this work were performed using the Large-scale

Atomic/Molecular Massively Parallel Simulator (LAMMPS) code [41].

2.2. GB characterization

GBs were characterized in terms of GB energy, excess volume, and number of coordination defects. The GB energy, ΔE^{GB}, was defined as

$$\Delta E^{\mathrm{GB}} = \frac{E^{\mathrm{GB}} - \frac{N^{\mathrm{GB}}}{N^{\mathrm{SC}}}E^{\mathrm{SC}}}{2A}, \tag{2}$$

where E^{GB} and E^{SC} are the lattice energies of the GB model and unit cell of MgO, respectively, N^{GB} and N^{SC} are the number of atoms in the GB model and unit cell, respectively, and A is the GB cross-sectional area. The excess volume per unit area, ΔV^{GB}, was defined as

$$\Delta V^{\mathrm{GB}} = \frac{V^{\mathrm{GB}} - \frac{N^{\mathrm{GB}}}{N^{\mathrm{SC}}}V^{\mathrm{SC}}}{2A} = \frac{V^{\mathrm{GB}} - N^{\mathrm{GB}}/\rho^{\mathrm{SC}}}{2A}, \tag{3}$$

where V^{GB} and V^{SC} are the volume of the GB model and unit cell of MgO, respectively, and ρ^{SC} is the number density of the unit cell. The excess volume can be related to the change in the number of atoms per unit area, ΔN^{GB}, according to

$$\Delta N^{\mathrm{GB}} = \frac{N^{\mathrm{GB}} - V^{\mathrm{GB}}\rho^{\mathrm{SC}}}{2A} = -\Delta V^{\mathrm{GB}}\rho^{\mathrm{SC}}. \tag{4}$$

Equation (4) shows that an increase in the excess volume directly corresponds to a decrease in the number of atoms in the vicinity of the GB plane. Definitions for coordination number and number of coordination defects are given in section S4 of Supporting Information. The energy and volume terms of GB models and unit cell in Eqs. (2)–(4) were obtained by performing energy minimization (structure optimization) technique using the GULP code.

To estimate how much these GB characteristics correlate with thermal conductivity, we calculated correlation coefficient between them [42]. The correlation coefficient, r, is a measure of the linear correlation between two variables, and defined as the following equation for x and y,

$$r = \frac{\sum_{i=1}^{n}(x_i - \bar{x})(y_i - \bar{y})}{\sqrt{\sum_{i=1}^{n}(x_i - \bar{x})^2}\sqrt{\sum_{i=1}^{n}(y_i - \bar{y})^2}}, \tag{5}$$

where n is the number of data, x_i and y_i are the individual data of x and y indexed with i, respectively, and $\bar{x}$ and $\bar{y}$ are the mean of x and y, respectively. It exhibits a value between -1 and $+1$, where negative and positive values mean negative and positive linear correlation, and 0 means no linear correlation.

2.3. Thermal conductivity calculations

Effective thermal conductivities across the GB planes in each STGB model at 300 K were calculated using perturbed MD [36]. The LAMMPS code was modified for this purpose. In perturbed MD, lattice thermal conductivity in the x direction can be calculated according to

$$\kappa_{\mathrm{lattice}} = \frac{1}{F_{\mathrm{ext}}T}\lim_{t\to\infty}\langle J_x\rangle_t, \tag{6}$$

where F_{ext} is the magnitude of the perturbation in the x direction, T is the absolute temperature, and J_x is the heat flux in the x direction. In this study, the perturbation was chosen to increase the heat flux in the direction perpendicular to GB planes. Average heat flux is proportional to the magnitude of the perturbation, and thus cancels out the $1/F_{\mathrm{ext}}$ term in Eq. (6). The calculated thermal conductivity is thus independent of the choice of F_{ext} within the linear response regime.

The microscopic heat flux, $\mathbf{J}$, can be written as

$$\mathbf{J} = \sum_i \mathbf{J}_i = \sum_i \frac{1}{2V}\left[\left\{m_i \mathbf{v}_i^2 \mathbf{I} + \sum_j \phi_{ij}\mathbf{I}\right\}\mathbf{v}_i - \sum_j (\mathbf{F}_{ij}\cdot\mathbf{v}_i)\mathbf{r}_{ij}\right], \tag{7}$$

where $\mathbf{J}_i$ is the atomic contribution of atom i to the overall heat flux, V is the volume of the supercell, m_i and $\mathbf{v}_i$ are the mass and velocity of atom i, ϕ_{ij} is the internal energy from interaction between atoms i and j, $\mathbf{I}$ is a unit tensor of second rank, and $\mathbf{F}_{ij}$ is the force exerted by atom j on atom i [43]. From Eqs. (6) and (7), overall lattice thermal conductivity can be written as a summation of the atomic thermal conductivities κ_i, which are calculated from the average heat flux of each atom, $\mathbf{J}_i$, i.e.,

$$\kappa_{\mathrm{lattice}} = \sum_i \kappa_i = \sum_i \frac{1}{F_{\mathrm{ext}}T}\lim_{t\to\infty}\left\langle J_{i,x}\right\rangle_t, \tag{8}$$

where $J_{i,\,x}$ is the contribution of atom i to overall heat flux in the x direction. The obtained atomic thermal conductivities were projected onto planes perpendicular to the rotation axes in Figs. 3 and 4. Equation (7) shows that the atomic thermal conductivities vary with supercell volume. To compare maps of atomic thermal conductivities between different sized supercells we normalized them by multiplying by the supercell cross-sectional area perpendicular to the rotation axis.

Perturbed MD simulations were performed for 1.1 ns, with the first 0.1 ns of data discarded because this portion represents the transition from thermal equilibrium to steady-state under the perturbation. The remaining 1.0 ns of each simulation was used to calculate thermal conductivity from the average heat flux. At least four different magnitudes of the perturbation were used (within the linear response regime) for each STGB model to determine the average thermal conductivity and its standard deviation. An example of simulation cells used for thermal conductivity calculations is shown in Fig. 1(a).

We also carried out a preliminary examination of the effect of grain size on thermal conductivity (since thermal conductivity is known to decrease with decreasing grain size [15,32]) by comparing models with the same STGBs separated by different distances (i.e., different box lengths or GB separation) under three dimensional periodic boundary conditions (see Fig. S1 of Supporting Information for details). Although effective thermal conductivities were found to increase with increasing GB separation, relative values (i.e., the order of increasing or decreasing effective thermal conductivities) between different STGBs remained essentially the same. From here on we thus restrict ourselves to reporting results for STGBs with a fixed separation of 5 nm.

Modal analyses were performed by extracting normal mode eigenvalues (phonon frequencies) and eigenvectors at the Γ point of STGB models. As explained by Lv and Henry [44], the atomic trajectories from MD can be projected onto the modes from LD. The velocity of each atom, $\mathbf{v}_i$, can be decomposed into modal contributions, $\mathbf{v}_i(n)$, from the time derivative of the amplitude of the normal modes, $\dot{X}(n)$, according to

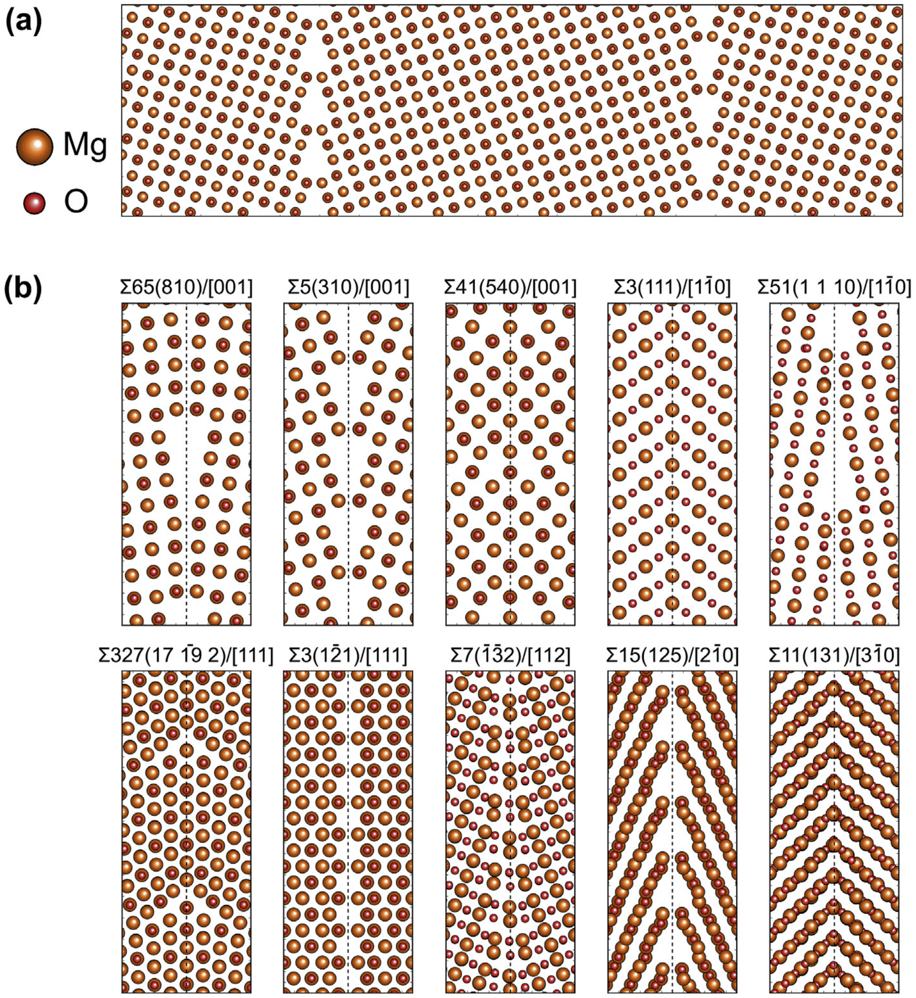

Fig. 1. (a) An example of STGB models used for thermal conductivity calculation with the GB separation of about 5 nm ($\Sigma5(310)/[001]$). There are two identical GB planes of the same GB structure to satisfy the three dimensional periodic boundary conditions. (b) Atom arrangements at ten types of STGBs. Orange and red balls represent Mg and O ions, respectively. The $\Sigma3(111)/[1\bar{1}0]$ GB has the highest symmetry and lowest defect density. (For interpretation of the references to colour in this figure legend, the reader is referred to the Web version of this article.)

$$\mathbf{v}_i = \sum_n \mathbf{v}_i(n) = \sum_n \frac{1}{\sqrt{m_i}} \mathbf{p}_i(n)\dot{X}(n), \tag{9}$$

where $\mathbf{p}_i(n)$is the eigenvector of atom i in mode n [44,45]. By substituting Eq. (9) into Eq. (7), we obtain the modal contributions to the heat flux as

$$\begin{aligned}\mathbf{J} &= \sum_n \mathbf{J}(n) = \sum_n \sum_i \mathbf{J}_i(n) \\ &= \sum_n \sum_i \frac{1}{2V}\left[\left\{ m_i \mathbf{v}_i(n)^2 \mathbf{I} + \sum_j \phi_{ij} \mathbf{I} \right\} \mathbf{v}_i(n) - \sum_j \left(\mathbf{F}_{ij} \cdot \mathbf{v}_i(n)\right)\mathbf{r}_{ij}\right],\end{aligned} \tag{10}$$

where $\mathbf{J}_i(n)$ is the contribution of atom i in mode n to overall heat flux. Combining Eqs. (6) and (10), modal contributions to overall lattice thermal conductivity are given by

$$\kappa_{\text{lattice}} = \sum_n \kappa(n) = \sum_n \sum_i \kappa_i(n) = \sum_n \sum_i \frac{1}{F_{\text{ext}} T} \lim_{t \to \infty} \left\langle J_{i,x}(n) \right\rangle_t, \tag{11}$$

where $\kappa(n)$ is the modal thermal conductivity of mode n, $\kappa_i(n)$ is the contribution of atom i in mode n to the overall thermal conductivity, and $J_{i,\ x}(n)$ is the contribution of atom i in mode n to the overall heat flux in the x direction.

The eigenvectors at Γ point were obtained by LD calculations using GULP and read into MD simulations, and then modal contributions to thermal conductivity were calculated with one perturbation for each STGB model for 5.1 ns to improve the statistical accuracy. Further details of the above procedures are given elsewhere [37,44]. Preliminary simulations showed that finite-size effects on thermal conductivity were negligible if simulation box lengths were greater than about 2.1 nm.

3. Results and discussion

Representative examples of the generated STGBs are shown in Fig. 1(b). GB structures varied widely depending on the misorientation angle, from densely packed to relatively open (low-density)

GBs. Many of these STGBs have never been reported before, but the relatively open polyhedral structural units found for the Σ5(310)/[001] GB plane are in good agreement with those obtained previously by *ab initio* calculations [2]. In addition, densely packed and relatively open dislocation core structures, which are found in low-angle STGBs with [001] or $[1\bar{1}0]$ rotation axes, are also in good agreement with those observed by scanning transmission electron microscopy (STEM) [3]. The agreement between simulated and experimental structures for known STGBs gives us confidence that the structures predicted for the other configurations are also reliable.

Effective thermal conductivities for each STGB with the GB separation of 5 nm were obtained by linear regression of the calculated thermal conductivities with different GB separations (Fig. S1). Values ranged from 9.2 to 33.4 W/mK, and are much lower than the lattice thermal conductivity of a single crystal of 119.2 W/mK (see section S2 of Supporting Information for details). The results indicate that even highly symmetrical GBs have a significant impact on lattice thermal conduction in MgO; the change in local atomic configurations from that in the bulk lattice is found to result in a large drop in thermal conduction irrespective of the particular GB plane or misorientation angle. We searched for correlations between the effective thermal conductivity and various GB properties to identify the most important factors influencing thermal conduction at GBs. Fig. 2 shows plots of the calculated effective thermal conductivities of all STGBs as functions of (a) rotation axis, (b) grain boundary energy, and (c) excess volume per unit area. Plots of effective thermal conductivity versus misorientation angle and number of coordination defects are provided in sections S3 and S4 of Supporting Information.

In Fig. 2(b) the effective thermal conductivities of low-angle STGBs appear to decrease linearly as the GB energy increases, which is the same trend as has been observed in other materials [11,26,29,33]. In contrast, the thermal conductivity of high-angle STGBs is not strongly correlated with GB energy. This marked difference can be attributed to differences in the GB structures themselves: low-angle STGBs are composed of arrays of dislocations whereas high-angle STGBs are composed of polyhedral structural units whose shapes vary with misorientation angle and rotation axis. The correlation coefficient between the effective thermal conductivity and GB energy is −0.53, which is smaller in magnitude than that of excess volume or number of coordination defects. In other words, even if a GB structure has an excess energy close to zero, lattice thermal conduction through it is not necessarily similar to that in a single crystal.

In the plots of effective thermal conductivity against excess volume in Fig. 2(c), the STGBs can be classified into three groups based on the three different correlations observed: (I) low-angle STGBs with dense dislocation core structures (e.g., Σ41(540)/[001] and $\Sigma327(17\overline{19}2)$/[111] STGBs in Fig. 1), (I’) low-angle STGBs with open dislocation core structures (e.g., Σ65(810)/[001] and Σ51(1 1 10)/$[1\bar{1}0]$ STGBs in Fig. 1), and (II) high-angle STGBs (e.g., Σ5(310)/[001] and $\Sigma3(1\bar{2}1)$/[111] STGBs in Fig. 1). Although the gradients of the curves in Fig. 2(c) for the three groups are different, the correlation coefficient between effective thermal conductivity and excess volume is −0.82, which is the strongest correlation with the GB properties that we found. This indicates that the excess volume is one of the most important factors determining lattice thermal conduction across GBs in MgO. An increase in the excess volume directly corresponds to a decrease in the number density of atoms in the vicinity of GB planes (see subsection 2.2, *GB characterization*). Lower number densities of atoms near GB planes means that local atomic arrangements or bonding environments at the GBs are more disrupted, which makes it difficult for phonons to propagate through them [26,46]. This explains why the effective thermal conductivity decreases with increasing excess volume. Detailed analysis of the twin boundary in Fig. 2(c) is provided in section S3 of Supporting Information. Note that, in MgO, the GB energy and excess volume are less correlated as indicated by their small correlation coefficient of 0.18, in contrast to metallic materials where a close linear correlation between them are observed [47]. This difference is attributed to the existence of relatively open GB structures in highly ionic MgO which are not observed in metallic materials, explaining why the strong correlation are found not in GB energy but in excess volume as shown in Fig. 2.

To understand better the reasons for the strong correlation between the effective thermal conductivity and excess volume, we performed real-space analyses of lattice thermal conduction, as these enable us to identify phonon transport paths across GB planes [37]. Fig. 3(a) shows plots of atomic thermal conductivities for three low-angle STGBs viewed down its [001] rotation axis. These low-angle STGBs have dense dislocation cores and belong to correlation group I, in which the effective thermal conductivity drops rapidly with increasing excess volume, as seen in Fig. 3(b). In the vicinity of the dislocation cores, the atomic thermal conductivities are low. This is presumably because Mg and O atoms next to the GB plane are under-coordinated (Fig. 3(c)), which disrupts the bonding network across the GB, leading to greater phonon scattering. The further from the dislocation cores, the higher the atomic thermal conductivities, even for atoms adjacent to or on the GB planes. In these cases, Mg and O ions are linked across the GB planes in a manner similar to that within the crystal bulk, and thus phonons are not strongly scattered in these regions.

As the misorientation angle increases, the intervals between dislocation cores (with their lower number densities of atoms) become shorter, and the excess volume increases. This results in increasingly narrower regions of undisrupted Mg-O bonding, explaining why the effective thermal conductivity decreases sharply in the case of group I GBs. Conversely, when the misorientation angle and excess volume decrease, the effective thermal conductivity approaches that of a single crystal because a greater volume of the GB region consists of Mg and O atoms in regular coordination environments with minimal scattering of phonons.

In the case of group I′ GBs, the mechanism of lattice thermal conduction is almost the same as that in group I GBs, i.e., phonons are mainly transported through fully coordinated regions of the GB, and thus thermal conductivity is also determined by the distances between dislocation cores (i.e., the dislocation density). Group I′ GBs, however, are composed of dislocation cores that are more open, with a lower number density of atoms, than group I GBs, which leads to longer intervals between dislocation cores and higher effective thermal conductivities for the same excess volume. Based on these observations, effective thermal conductivities of other low-angle STGB containing dislocation core structures varying from dense to open are expected to lie between the curves of correlations I and I’ in Fig. 2(c).

Fig. 4(a) shows atomic thermal conductivities of three high-angle STGBs, namely Σ9(221)/$[1\bar{1}0]$, $\Sigma5(0\bar{2}1)$/[112] and Σ5(310)/[001], viewed down their respective rotation axes. These STGBs belong to correlation group II, where effective thermal conductivity gradually decreases, as shown in Fig. 4(b). Almost all high-angle STGBs have lower effective thermal conductivity than low-angle STGBs. This can be explained by comparing the structures of the two types of STGBs. In high-angle STGBs, polyhedral structural units are arrayed along the GB plane, and all atoms adjacent to the GB plane are under-coordinated, as seen in Fig. 4(c). This extended disruption of the bonding connectivity at GBs means that efficient transport of phonons is no longer possible anywhere along the GB, unlike in low-angle STGBs with their alternating under-coordinated and fully coordinated regions.

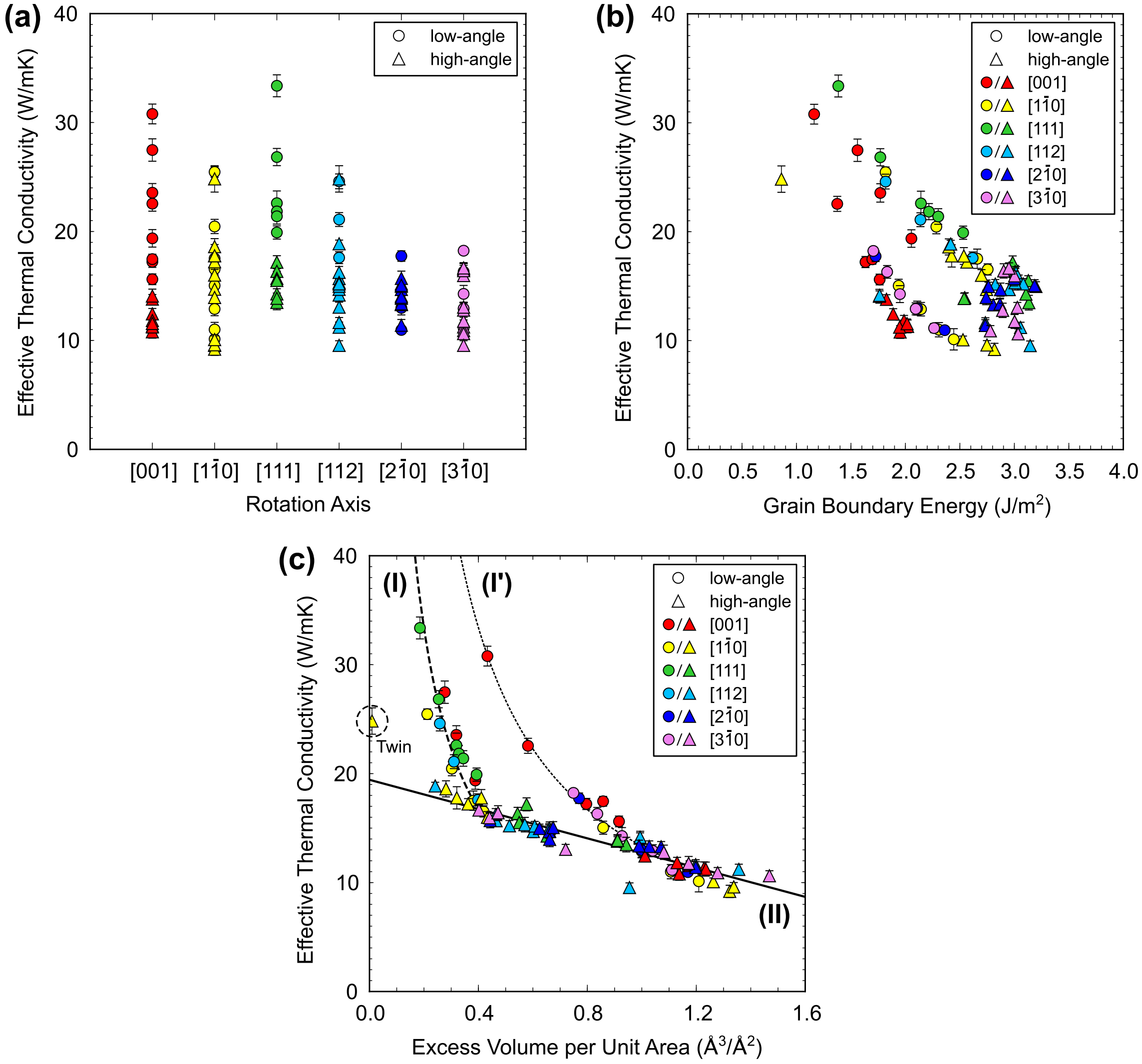

Fig. 2. Effective thermal conductivities across STGBs in MgO: (a) as a function of rotation axis, (b) grain boundary energy, and (c) excess volume per unit area. In (c), STGBs can be classified into three groups based on the type of correlation: (I) low-angle STGBs with dense dislocation core structures, (I′) low-angle STGBs with open dislocation core structures, and (II) high-angle STGBs.

In group II GBs, the higher excess volume is a result of the GB's structural units being more open (lower number densities) than simple dislocation cores. However, the influence of excess volume on effective thermal conductivity is relatively small because changes in the shapes of the structural units do not affect phonon transport paths across GB planes much in comparison with changes in dislocation densities at low-angle STGB planes. This explains why effective thermal conductivity decreases gradually with increasing excess volume in group II GBs. The above results show that, once a GB has been classified as low-angle or high-angle, its effective thermal conductivity can be predicted with good accuracy from its excess volume.

To determine which phonons are scattered by different STGBs, we extracted modal contributions to the effective thermal conductivities from perturbed MD data in conjunction with LD [37]. GB separations were fixed at about 4 nm in each case. In preliminary calculations, it was found that the phonon density of states (PDOS) of STGB models with GB separations of a few nanometers is almost the same as that of a single crystal (details are provided in section S5 of Supporting Information). This means that specific heat in Eq. (1) and its temperature dependence of polycrystals are not very different from that of a single crystal in MgO; a similar result was reported from an experimental study of the specific heats of poly- and nanocrystalline diamonds [48]. Thus, if we assume Eq. (1) holds for these cases, the decrease in the effective thermal conductivity as will be disscused as follows can thus be attributed directly to decreases in relaxation time and the group velocity of the phonons.

To clarify the impact of dislocation density in low-angle STGBs and the difference between low- and high-angle STGBs more quantitatively, modal contribution analyses were carried out for three low-angle STGBs and one high-angle STGB, all with [111] rotation axis. Other low-angle STGBs with dense and open dislocation structures were confirmed to produce similar results (Section S6 of Supporting Information). As seen in Fig. 5(a), the spectral effective thermal conductivities are high at frequencies below 20 THz, and the area below the curve up to this frequency accounts for about 80% of the total thermal conductivity. With increasing misorientation angle, the effective thermal conductivity gradually decreases over the whole frequency range; no clear distinction between low- and high-angle STGBs are found except for the magnitude of thermal conductivity. These results indicate that, although the phonon frequency ranges that are scattered by GBs is almost the same for low- and high-angle STGBs, local atomic arrangements at GB planes affect the scattering probabilities and

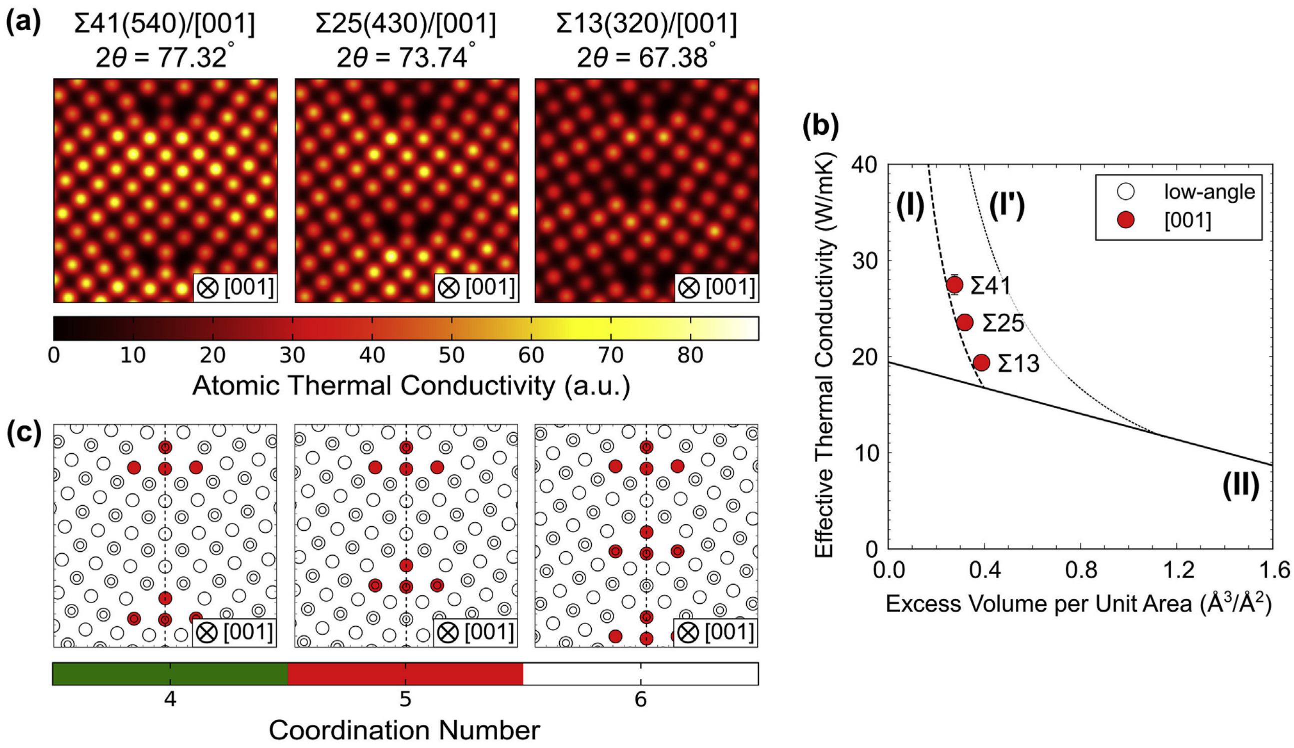

Fig. 3. Atomic thermal conductivities in the vicinity of three low-angle STGBs with [001] rotation axis. (a) Maps of atomic thermal conductivities, (b) effective thermal conductivities of the low-tilt STGBs as a function of excess volume, and (c) maps of coordination number, in which large and small balls represent Mg and O ions, respectively. In rocksalt MgO, both Mg and O ideally have coordination numbers of six.

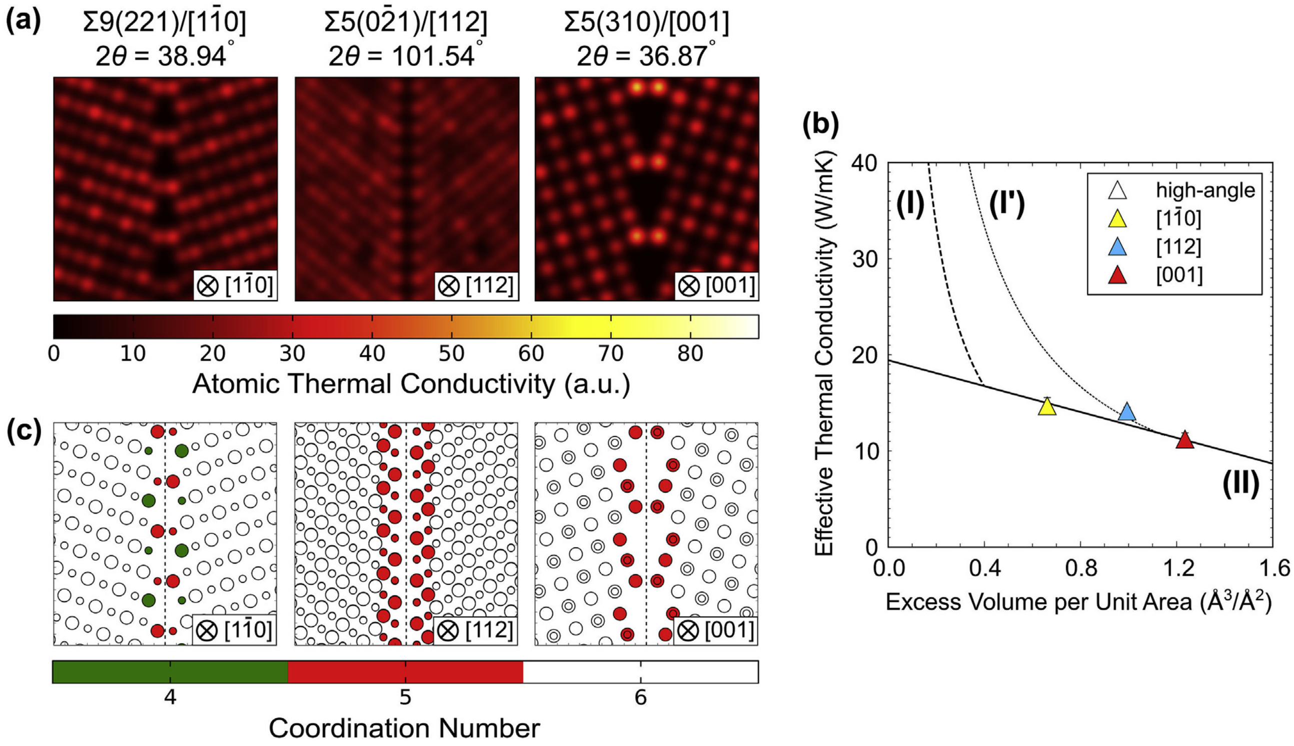

Fig. 4. Atomic thermal conductivities in the vicinity of three high-angle STGBs with different rotation axes. (a) Maps of atomic thermal conductivities, (b) effective thermal conductivities of the high-tilt STGBs as a function of excess volume, and (c) maps of coordination number, where large and small balls represent Mg and O ions, respectively. In rocksalt MgO, both Mg and O ideally have coordination numbers of six.

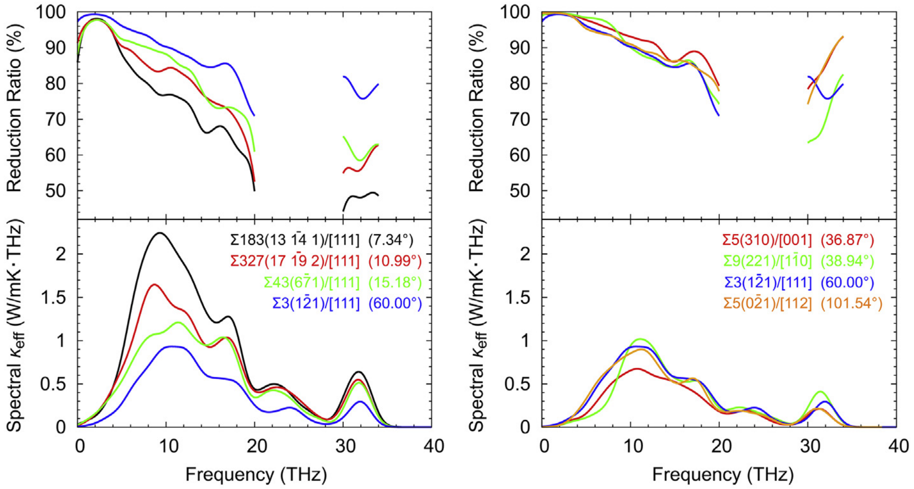

Fig. 5. Spectral effective thermal conductivities of STGBs and their reduction ratios compared to a single crystal. (a) Low- and high-angle STGBs with [111] rotation axes, and (b) high-angle STGBs with a variety of rotation axes.

group velocities of phonons significantly.

To quantitatively estimate the magnitude of phonon transport suppression relative to a single crystal, we calculated the reduction ratio, $R(\omega)$, according to the following equation,

$$R(\omega) = -\frac{\kappa_{\mathrm{GB}}(\omega) - \kappa_{\mathrm{SC}}(\omega)}{\kappa_{\mathrm{SC}}(\omega)}, \tag{12}$$

where $\kappa_{\mathrm{GB}}(\omega)$ and $\kappa_{\mathrm{SC}}(\omega)$ are the spectral thermal conductivities of the GB model and a single crystal of MgO, respectively (section S7 of Supporting Information shows the spectral thermal conductivity of a single crystal). The reduction ratios are plotted in Fig. 5(a); between 20 and 30 THz and above 34 THz no values are given because in those frequency ranges the thermal conductivity of a single crystal is already very low, and thus the calculated relative reduction is associated with large errors.

Reduction at low frequencies is very large, indicating that acoustic phonons are strongly scattered by STGBs. This is probably because low-frequency acoustic phonons have longer mean free paths. The reduction ratio decreases almost linearly with increasing frequency, indicating that high-frequency optical phonons are less affected by the GBs than acoustic phonons. This may be because the high-frequency optical phonons also undergo phonon-phonon scattering to some extent before being scattered by the GBs due to their shorter mean free paths. These results are consistent with the prediction by Klemens et al. [16] that GBs reduce lattice thermal conductivity at low frequencies. In contrast, high-angle STGBs reduce the phonon transport more than low-angle STGBs at all frequencies. High-angle STGBs are thus more effective at reducing lattice thermal conductivity than low-angle STGBs regardless of the phonon frequency.

Spectral effective thermal conductivities of several high-angle STGBs and the reduction ratios compared to a single crystal are plotted in Fig. 5(b). (Results for other high-angle STGBs are provided in section S6 of Supporting Information.) It can be seen that there are no significant differences between the spectral effective thermal conductivities of different high-angle STGBs, indicating that phonons are scattered by a similar mechanism in all of them. This is presumably because the atomic arrangements of the structure units in high-angle STGBs are relatively simple (see, e.g., Fig. 1), due to the close-packed FCC structure of MgO. Reduction ratios decrease gradually with increasing phonon frequency to about 70–80% at 20 Hz, remaining at this level at frequencies above 30 Hz. The extensive phonon scattering by high-angle STGBs even at intermediate and high frequencies explains why effective thermal conductivities of high-angle STGBs are lower than those of low-angle STGBs, which only scatter phonons effectively at low frequencies.

4. Conclusions

We systematically calculated effective thermal conductivities across STGBs in MgO using the perturbed MD method. The effective thermal conductivities varied by a factor of four between the 81 different STGBs examined. The results show that the effective thermal conductivity of a given STGB can be predicted from its excess volume because of the strong correlation found between the two. Real-space analyses of lattice thermal conduction in low- and high-angle STGBs revealed that the phonon transport mechanisms in these two classes of GBs are different, and hence the relationship between thermal conductivity and excess volume is also different. Low-angle STGBs, which consist of dislocation core structures, exhibited higher thermal conductivities but with greater variability because the phonon transport paths across their GB planes strongly depend on the dislocation core number density (and hence spacing between cores). In contrast, high-angle STGBs exhibit lower thermal conductivity with smaller variability because their structural units represent a greater disruption of the bonding environments of atoms (more coordination defects) at GB planes regardless of the shape of the structural units. These results suggest that low-angle STGBs are to be preferred when seeking to increase lattice thermal conductivity, whereas the number of high-angle STGBs should be maximized when seeking to decrease it.

Calculations of modal contributions to effective thermal conductivities revealed that all the STGBs strongly suppress lattice thermal conduction of low-frequency acoustic phonons. Low-angle STGBs mainly reduce phonon transport at low frequencies, whereas high-angle STGBs strongly reduce it at intermediate and high frequencies also, which is why high-angle STGBs show lower thermal conductivity than low-angle STGBs overall. Despite the wide variety of structural units found in high-angle STGBs, no significant differences were observed between the spectral thermal conductivities of the STGBs examined here, suggesting that the precise GB orientation of high-angle STGBs does not affect significantly the amount of reduction of lattice thermal conductivity, at least in materials with close-packed FCC structures like MgO. These insights suggest that grain boundary engineering at the nanoscale using advanced processing techniques should allow lattice thermal conductivities to be tailored for specific applications by controlling the fraction of low- and high-angle STGBs formed, and, in the case of low-angle STGBs, their dislocation core densities.

Author contributions

S.F., T.Y. and M.Y. designed the study. S.F. performed theoretical calculations. T.Y. carried out structural analyses. S.F, T.Y., M.Y. interpreted the results and wrote the manuscript.

Notes

The authors declare no competing financial interest.

Acknowledgment

This work was supported by Grant-in-Aid for Scientific Research on Innovative Areas 'Nano Informatics' from the Japan Society for the Promotion of Science (JSPS) [grant number 25106005]; a JSPS Fellowship from JSPS [grant number 15J00489]; and Cross-ministerial Strategic Innovation Promotion (SIP) Program "Structural Materials for Innovation" from the Japan Science and Technology Agency (JST). The authors are grateful to Dr. C. A. J. Fisher of Japan Fine Ceramics Center for helpful discussions and for critical reading of the manuscript.

Appendix A. Supplementary data

Supplementary data to this article can be found online at https://doi.org/10.1016/j.actamat.2019.04.009.

References

[1] Z. Wang, M. Saito, K.P. McKenna, L. Gu, S. Tsukimoto, A.L. Shluger, Y. Ikuhara, Atom-resolved imaging of ordered defect superstructures at individual grain boundaries, Nature 479 (2011) 380–383.

[2] Y. Yan, M. Chisholm, G. Duscher, a. Maiti, S. Pennycook, S. Pantelides, Impurity-induced structural transformation of a MgO grain boundary, Phys. Rev. Lett. 81 (1998) 3675–3678.

[3] Z. Wang, M. Saito, K.P. McKenna, Y. Ikuhara, Polymorphism of dislocation core structures at the atomic scale, Nat. Commun. 5 (2014) 3239.

[4] W. Tong, H. Yang, P. Moeck, M.I. Nandasiri, N.D. Browning, General schema for [0 0 1] tilt grain boundaries in dense packing cubic crystals, Acta Mater. 61 (2013) 3392–3398.

[5] J. Han, V. Vitek, D.J. Srolovitz, The grain-boundary structural unit model redux, Acta Mater. 133 (2017) 186–199.

[6] T. Nakagawa, H. Nishimura, I. Sakaguchi, N. Shibata, K. Matsunaga, T. Yamamoto, Y. Ikuhara, Grain boundary character dependence of oxygen grain boundary diffusion in α-Al_2O_3 bicrystals, Scripta Mater. 65 (2011) 544–547.

[7] J.S. Park, Y.B. Kim, J. An, F.B. Prinz, Oxygen diffusion across the grain boundary in bicrystal yttria stabilized zirconia, Solid State Commun. 152 (2012) 2169–2171.

[8] T. Yamamoto, Y. Sato, T. Tanaka, K. Hayashi, Y. Ikuhara, T. Sakuma, Electron transport behaviors across single grain boundaries in n-type $BaTiO_3$, $SrTiO_3$ and ZnO, J. Mater. Sci. 40 (2005) 881–887.

[9] Y. Sato, T. Yamamoto, Y. Ikuhara, Atomic structures and electrical properties of ZnO grain boundaries, J. Am. Ceram. Soc. 90 (2007) 337–357.

[10] J.J. Bean, M. Saito, S. Fukami, H. Sato, S. Ikeda, H. Ohno, Y. Ikuhara, Atomic structure and electronic properties of MgO grain boundaries in tunneling magnetoresistive devices, Sci. Rep. 7 (2017) 45594.

[11] K. Tai, A. Lawrence, M.P. Harmer, S.J. Dillon, Misorientation dependence of Al_2O_3 grain boundary thermal resistance, Appl. Phys. Lett. 102 (2013) 034101.

[12] M.A. Angadi, T. Watanabe, A. Bodapati, X. Xiao, O. Auciello, J.A. Carlisle, J.A. Eastman, P. Keblinski, P.K. Schelling, S.R. Phillpot, Thermal transport and grain boundary conductance in ultrananocrystalline diamond thin films, J. Appl. Phys. 99 (2006) 063503.

[13] Y. Zhou, H. Hyuga, D. Kusano, Y. Yoshizawa, K. Hirao, A tough silicon nitride ceramic with high thermal conductivity, Adv. Mater. 23 (2011) 4563–4567.

[14] A.J. Minnich, M.S. Dresselhaus, Z.F. Ren, G. Chen, Bulk nanostructured thermoelectric materials: current research and future prospects, Energy Environ. Sci. 2 (2009) 466–479.

[15] Z. Wang, J.E. Alaniz, W. Jang, J.E. Garay, C. Dames, Thermal conductivity of nanocrystalline silicon: importance of grain size and frequency-dependent mean free paths, Nano Lett. 11 (2011) 2206–2213.

[16] P.G. Klemens, M. Gell, Thermal conductivity of thermal barrier coatings, Mater. Sci. Eng., A 245 (1998) 143–149.

[17] H.S. Yang, G.R. Bai, L.J. Thompson, J.A. Eastman, Interfacial thermal resistance in nanocrystalline yttria-stabilized zirconia, Acta Mater. 50 (2002) 2309–2317.

[18] J.P. Feser, E.M. Chan, A. Majumdar, R.A. Segalman, J.J. Urban, Ultralow thermal conductivity in polycrystalline CdSe thin films with controlled grain size, Nano Lett. 13 (2013) 2122–2127.

[19] C. Abs Da Cruz, N.A. Katcho, N. Mingo, R.G.A. Veiga, Thermal conductivity of nanocrystalline SiGe alloys using molecular dynamics simulations, J. Appl. Phys. 114 (2013) 164310.

[20] J. Yang, Theory of thermal conductivity, in: M.T. Tritt (Ed.), Thermal Conductivity: Theory, Properties, and Applications, Springer, New York, 2006, pp. 1–20.

[21] S. Ju, X. Liang, Thermal conductivity of nanocrystalline silicon by direct molecular dynamics simulation, J. Appl. Phys. 112 (2012) 064305.

[22] H. Dong, B. Wen, R. Melnik, Relative importance of grain boundaries and size effects in thermal conductivity of nanocrystalline materials, Sci. Rep. 4 (2014) 7037.

[23] D. Aketo, T. Shiga, J. Shiomi, Scaling laws of cumulative thermal conductivity for short and long phonon mean free paths, Appl. Phys. Lett. 105 (2014) 131901.

[24] P.K. Schelling, S.R. Phillpot, P. Keblinski, Kapitza conductance and phonon scattering at grain boundaries by simulation, J. Appl. Phys. 95 (2004) 6082–6091.

[25] J.K. Bohrer, K. Schröer, L. Brendel, D.E. Wolf, Thermal resistance of twist boundaries in silicon nanowires by nonequilibrium molecular dynamics, AIP Adv. 7 (2017) 045105.

[26] T. Watanabe, B. Ni, S.R. Phillpot, P.K. Schelling, P. Keblinski, Thermal conductance across grain boundaries in diamond from molecular dynamics simulation, J. Appl. Phys. 102 (2007) 063503.

[27] A. Bagri, S.P. Kim, R.S. Ruoff, V.B. Shenoy, Thermal transport across twin grain boundaries in polycrystalline graphene from nonequilibrium molecular dynamics simulations, Nano Lett. 11 (2011) 3917–3921.

[28] A. Cao, J. Qu, Kapitza conductance of symmetric tilt grain boundaries in graphene, J. Appl. Phys. 111 (2012) 053529.

[29] A. Chernatynskiy, X.M. Bai, J. Gan, Systematic investigation of the misorientation- and temperature-dependent Kapitza resistance in CeO_2, Int. J. Heat Mass Transf. 99 (2016) 461–469.

[30] Z. Zheng, X. Chen, B. Deng, A. Chernatynskiy, S. Yang, L. Xiong, Y. Chen, Phonon thermal transport through tilt grain boundaries in strontium titanate, J. Appl. Phys. 116 (2014) 073706.

[31] T. Chen, D. Chen, B.H. Sencer, L. Shao, Molecular dynamics simulations of grain boundary thermal resistance in UO_2, J. Nucl. Mater. 452 (2014) 364–369.

[32] D. Spiteri, J. Anaya, M. Kuball, The effects of grain size and grain boundary characteristics on the thermal conductivity of nanocrystalline diamond, J. Appl. Phys. 119 (2016) 085102.

[33] C. Kimmer, S. Aubry, A. Skye, P.K. Schelling, Scattering of phonons from a high-energy grain boundary in silicon: dependence on angle of incidence, Phys. Rev. B 75 (2007) 1–7.

[34] B. Deng, A. Chernatynskiy, S.B. Sinnott, S.R. Phillpot, Thermal transport at (001) twist grain boundaries in UO_2, J. Nucl. Mater. 479 (2016) 167–173.

[35] K. Gordiz, A. Henry, A formalism for calculating the modal contributions to thermal interface conductance, New J. Phys. 17 (2015) 103002.

[36] M. Yoshiya, A. Harada, M. Takeuchi, K. Matsunaga, H. Matsubara, Perturbed molecular dynamics for calculating thermal conductivity of Zirconia, Mol. Simulat. 30 (2004) 953–961.

[37] S. Fujii, M. Yoshiya, C.A.J. Fisher, Quantifying anharmonic vibrations in thermoelectric layered cobaltites and their role in suppressing thermal conductivity, Sci. Rep. 8 (2018) 11152.

[38] T. Yokoi, M. Yoshiya, Atomistic simulations of grain boundary transformation under high pressures in MgO, Phys. B. 532 (2018) 2–8.

[39] L. Priester, Geometrical order of grain boundaries, in: L. Priester (Ed.), Grain Boundaries -From Therory to Engineering, Springer, New York, 2013, pp. 3–28.

[40] J.D. Gale, GULP: a computer program for the symmetry-adapted simulation of solids, J. Chem. Soc. Faraday. Trans. 93 (1997) 629–637.

[41] S. Plimpton, Fast Parallel algorithms for short-range molecular dynamics, J. Comput. Phys. 117 (1995) 1–19.

[42] K.W. Smillie, An Introduction to Regression and Correlation, Academic Press, New York, 1966.

[43] J.H. Irving, J.G. Kirkwood, The statistical mechanical theory of transport processes. IV. The equations of hydrodynamics, J. Chem. Phys. 18 (1950) 817.

[44] W. Lv, A. Henry, Direct calculation of modal contributions to thermal conductivity via Green-Kubo modal analysis, New J. Phys. 18 (2016) 013028.

[45] M.T. Dove, Introduction to Lattice Dynamics, Cambridge University Press, Cambridge, 1993.

[46] N. Goel, E.B. Webb III, A. Oztekin, J.M. Rickman, S. Neti, Kapitza resistance at segregated boundaries in β-SiC, J. Appl. Phys. 118 (2017) 115101.

[47] D. Wolf, Structure-energy correlation for grain boundaries in F.C.C. metals-III. Symmetrical tilt boundaries, Acta Metall. Mater. 38 (1990) 781–790.

[48] C. Moelle, M. Werner, F. Szücs, D. Wittorf, M. Sellschopp, J. von Borany, H.-J. Fecht, C. Johnston, Specific heat of single-, poly- and nanocrystalline diamond, Diam. Relat. Mater. 7 (1998) 499–503.

nature COMMUNICATIONS

ARTICLE

https://doi.org/10.1038/s41467-020-15619-9 OPEN

Quantitative prediction of grain boundary thermal conductivities from local atomic environments

Susumu Fujii[1,2,3]✉, Tatsuya Yokoi[3,4], Craig A. J. Fisher[1], Hiroki Moriwake[1,2] & Masato Yoshiya[1,3,5]✉

Quantifying the dependence of thermal conductivity on grain boundary (GB) structure is critical for controlling nanoscale thermal transport in many technologically important materials. A major obstacle to determining such a relationship is the lack of a robust and physically intuitive structure descriptor capable of distinguishing between disparate GB structures. We demonstrate that a microscopic structure metric, the local distortion factor, correlates well with atomically decomposed thermal conductivities obtained from perturbed molecular dynamics for a wide variety of MgO GBs. Based on this correlation, a model for accurately predicting thermal conductivity of GBs is constructed using machine learning techniques. The model reveals that small distortions to local atomic environments are sufficient to reduce overall thermal conductivity dramatically. The method developed should enable more precise design of next-generation thermal materials as it allows GB structures exhibiting the desired thermal transport behaviour to be identified with small computational overhead.

---

[1] Nanostructures Research Laboratory, Japan Fine Ceramics Center, 2-4-1 Mutsuno, Atsuta, Nagoya 456-8587, Japan. [2] Center for Materials Research by Information Integration, National Institute for Materials Science, 1-2-1 Sengen, Tsukuba, Ibaraki 305-0047, Japan. [3] Department of Adaptive Machine Systems, Osaka University, 2-1 Yamadaoka, Suita, Osaka 565-0871, Japan. [4] Department of Materials Physics, Nagoya University, Furo-chou, Chikusa, Nagoya 464-8603, Japan. [5] Division of Materials and Manufacturing Science, Osaka University, 2-1 Yamadaoka, Suita, Osaka 565-0871, Japan.
✉email: susumu_fujii@jfcc.or.jp; yoshiya@ams.eng.osaka-u.ac.jp

Thermal conductivity is a fundamental property of a material and crucial for many technological applications, e.g., thermoelectrics[1–3], thermal barrier coatings[4,5], high-power devices[6,7] and microelectronics[8,9]. Recent studies have shown that nanocrystalline materials, which have large grain boundary (GB) populations, exhibit extremely low lattice thermal conductivities[1,5,10,11], even when the bulk form is thermally conductive, e.g., elemental silicon[12,13]. This dramatic reduction in lattice thermal conductivity is commonly attributed to shortening of the phonon mean free path (MFP), with the assumption that it is of the same order as the average grain size[5,12,14,15]. Although this first-order approximation has informed most attempts to control thermal conductivity, e.g., by tailoring grain size distributions[16], it does not take into account the impact of individual GBs and their different atomistic structures, and recent experimental studies have indicated that the amount of thermal conductivity reduction varies considerably depending on the structure of a particular GB[17–19]. For example, Tai et al[18]. measured the thermal resistances of three twist Al_2O_3 GBs and found that they vary by a factor of three. Quantitatively determining the relationship between GB structure and thermal conductivity is thus desirable for designing thermally functional materials at the nano-scale.

Many computational studies have been performed over the past two decades using non-equilibrium molecular dynamics (MD) to examine thermal conductivities of individual GBs[20–24]. Although the results revealed that thermal conductivity varies with misorientation angle and GB energy, the underlying physical mechanism responsible for this has not been elucidated in terms of the GB structures themselves. To help remedy this, we recently calculated thermal conductivities of 81 MgO symmetric tilt GBs (STGBs), and found that GB excess volume, which stems from reduced atomic coordination and non-optimal bond lengths at the GB core (the characteristic structure pattern centred on the GB plane), is strongly correlated with thermal conductivity[25]. We identified three different correlations depending on the type of GB, with low thermal conductivities occurring in the vicinity of the most open structures. The results provided further evidence that thermal conductivity can vary significantly depending on the type of GB and its atomic structure.

An analysis based on excess volume alone, however, is insufficient for explaining structure-property relationships over high-dimensional space, e.g., general GBs in polycrystals, because a given excess volume is not necessarily unique to a particular GB structure. This is because excess volume is a measure of the non-optimum packing of atoms at a GB but contains no other information about how the GB structure differs from that in the crystal bulk or to other GBs; consequently two GBs can have the same excess volume but exhibit very different thermal conductivity behaviour because of differences in atom configurations and bonding[26–30]. General GBs consist of complex mixtures of simpler high-symmetry (planar) GBs, and are even harder to analyse because of the enormous number of degrees of freedom involved. This problem is exacerbated when the effect of intrinsic defects or impurity atoms is included. A brute force method, e.g., MD simulation, can enable a specific thermal conductivity to be assigned to a specific GB core structure so that the dependence of thermal conductivity on GB misorientation and composition can be examined systematically, but even using computationally inexpensive empirical potential models it would take an inordinately long time to generate sufficient data for a wide variety of GB forms. Thus a more efficient and computationally tractable method is needed if meaningful progress is to be made.

A promising method for handling large numbers of different atomic configurations is the use of structure descriptors developed in the burgeoning field of materials informatics[31–35]. These descriptors contain information sufficient to define uniquely a particular atom arrangement, and act as fingerprints distinguishing different atomistic structures. Recent studies have used such descriptors in the context of machine learning (ML) to enhance our understanding of GB structure-property relationships[36–38]. A prime example is the study of Rosenbrock et al.[38]; using the smooth overlap of atomic positions (SOAP) descriptor[39,40] and a supervised ML technique, they identified a set of building blocks (or representative local atomic environments, LAEs) from which GBs of metallic Ni are constructed, and determined which LAEs strongly influence GB energies and mobilities. In related work[41] they reviewed various models used to analyse GB structures (in particular comparing the utility of the local environment representation to that of the structural unit model in the analysis of 126 Ni STGBs), and showed that the former is in many respects superior to the others, most notably because it provides a smoothly varying function.

In this report we describe our search for a suitable SOAP-based microscopic metric that correlates with GB thermal conductivity and can be used to identify relationships between GB structure and thermal conductivity. To ensure the rigour of the relationship identified, a wide range of GBs are included in the analysis, viz., symmetric tilt, twist, twin and asymmetric tilt GBs stable at standard pressure, and symmetric tilt GBs stable at higher pressure. MgO is chosen as a model material because of its simple structure and long history of experimental and theoretical work. The most appropriate microscopic quantity that we identify, which we refer to as the local distortion factor, LDF, measures deviations in the local structural environment of an atom near a GB from that of an identical atom in the crystal bulk, and correlates well with atomically decomposed thermal conductivities perpendicular to the GB extracted from perturbed MD simulations. We then construct a prediction model using multiple linear regression with input variables based on hierarchical clustering of LAEs, and demonstrate that the thermal conductivity of a GB can be predicted with high accuracy using this model. Analysing the results in terms of LDFs reveals that even a small amount of structural distortion at the GB is sufficient to suppress thermal conductivity strongly. We expect that extension of this ML-based technique to other materials should greatly enhance our understanding of GB behaviour, thereby enabling materials to be tailored to exhibit the desired thermal properties, especially once suitable nano-scale engineering techniques have been developed.

Results

Effective thermal conductivities. In addition to low-angle and high-angle STGBs reported previously[25], in this study we calculated effective thermal conductivities across GB planes of standard-pressure twist, asymmetric tilt and high-pressure tilt GBs of MgO to obtain a more comprehensive understanding of the relationship between GB structure and thermal conductivity. Detailed lists of all GB models used in this study are provided in Supplementary Tables 1–9, with some relevant properties summarised in Supplementary Figs. 1–3, and explanatory notes included as Supplementary Notes 1 and 2. The combined results are plotted in Fig. 1a against excess volume per unit area of each GB, with representative GB structures shown in Fig. 1b–h. For the STGBs under standard pressure, the thermal conductivities exhibit three different correlations with excess volume depending on the GB type: low-angle GBs with (I) dense and (I′) open dislocation core structures, and (II) high-angle GBs. In Fig. 1a, thermal conductivities of high-angle high-pressure STGBs also fall on correlation line II (solid black line), whereas their excess volumes are smaller than those of standard-pressure STGBs with the same misorientation because of their denser GB core

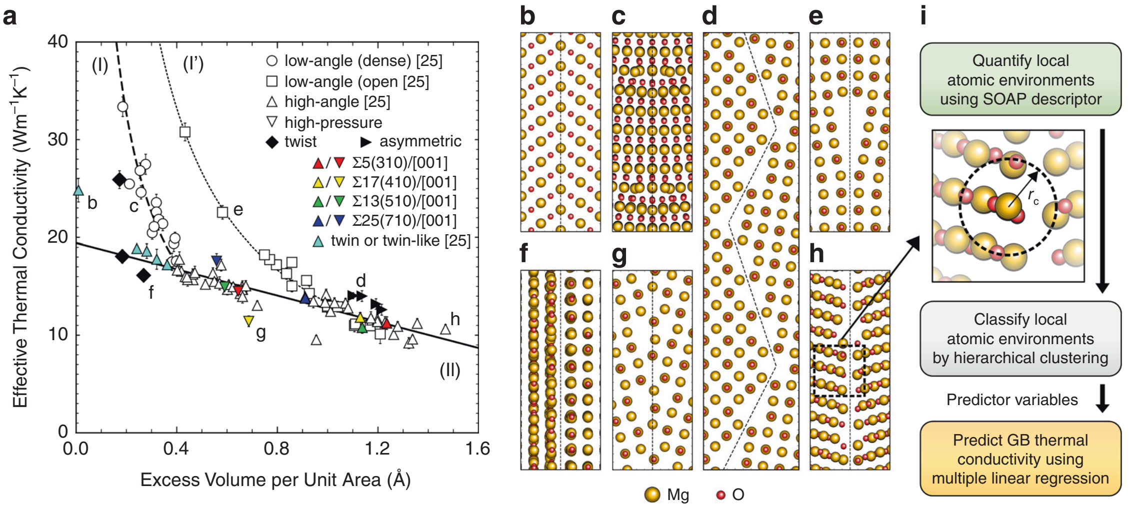

Fig. 1 Overview of GB thermal conductivities and structures. **a** Effective thermal conductivities across standard-pressure tilt and twist GBs, twin (and twin-like) boundaries, and high-pressure tilt GBs as a function of excess volume. Data for standard-pressure tilt GBs and the correlations indicated by solid, dashed and dotted lines are from Fujii et al.[25] (I) low-angle tilt GBs with dense dislocation core structures; (I′) low-angle tilt GBs with open dislocation core structures; and (II) high-angle tilt GBs. Error bars indicate standard deviations in thermal conductivity calculated using perturbations of different magnitudes. **b**–**h** Example structures of different types of GB: **b** twin, **c** low-angle GB with dense dislocation cores, **d** asymmetric tilt GB, **e** low-angle GB with open dislocation cores, **f** twist GB, **g** high-pressure high-angle GB and **h** standard-pressure high-angle GB. **i** Method for predicting GB thermal conductivities based on local atomic environments. r_c is the cutoff radius of the SOAP descriptor.

structures. In contrast, thermal conductivities of low-angle high-pressure STGBs deviate from these trends, lying between lines I and I′ because of the intermediate densities of their dislocation structures. Thermal conductivities of asymmetric Σ5 [001] tilt GBs lie only slightly above the correlation II line, probably because their GB core structures are similar to those of high-angle GBs; the asymmetric boundaries in this study are mainly composed of (310) and (210) facets similar to those in the corresponding symmetric boundaries, although different kinds of atomic structures are formed at the facet junctions.

The three twist GBs examined also show similar behaviour to the dense low-angle STGBs; the thermal conductivity is high for low excess volumes, and initially decreases rapidly with increasing excess volume, but the rate of decrease diminishes once the dislocations begin to overlap. The most pertinent difference between twist and tilt GBs in this case, however, is that the excess volumes of twist GBs are much smaller than those of STGBs because of their denser structures. GBs with very high symmetry and thus high number density, viz., the Σ3(111) twin boundary and GBs with LAEs similar to it (labelled twin-like in Fig. 1a), appear to fall on a fourth correlation line, one flatter than correlations I or I′ (see Supplementary Fig. 1 for their structures). The results indicate that the thermal conductivities of high-pressure tilt, asymmetric tilt and twist GBs are governed by the same mechanism as for STGBs, and that the macroscopic metric, i.e., GB excess volume, is inadequate as a parameter for accurately predicting thermal conductivities of various types of GB structures. As explained below, we overcome this problem by quantifying LAEs in the vicinity of GBs using the SOAP descriptor to generate input data for ML techniques. A schematic of the method is shown in Fig. 1i.

Quantifying local distortions. The mechanism by which thermal conductivity is reduced at GBs is expected to be related to local structural distortions because long-range thermal transport occurs by phonons, which are the collective motion of atoms in a periodic lattice, and any disturbance to this motion results in enhanced phonon scattering, as evidenced by numerous experimental and theoretical studies[1,3,5,10–25]. To quantify these structural distortions, we defined a (non-normalised) dissimilarity metric that measures the difference in LAE between an atom at a GB and an atom in the crystal bulk, which we refer to as the local distortion factor, LDF using the SOAP descriptor (see Methods for details). We calculated LDFs of all atoms in GB structure models for a wide variety of different GB types, viz., 80 standard-pressure STGBs (about six different rotation axes), a twin[25], four high-pressure [001] STGBs, three (001) twist GBs and four asymmetric [001] tilt GBs. Figure 2a shows a plot of the LDFs in each model classified by GB rotation axis in order of increasing tilt or twist angle. The LDFs span a wide range, from 0 to 3000, with atoms at open GBs tending to have high values and those at relatively dense GBs to have low values.

To quantify how LDFs vary with bond elongation, we also calculated those of atoms in uniformly expanded, defect-free MgO single crystals, and the results are plotted in Fig. 2b. This plot shows that when an MgO crystal is expanded isotropically, LDFs (those of cations and anions are equivalent in this case because of its rock-salt structure) increase smoothly and reach a value equivalent to the maximum LDF in the GB models for a lattice constant elongation of ~9.5% and volume expansion of ~31.2%. Unlike the atoms in the perfect crystal, atoms at GBs are not subjected to as large increases in local volume or bond lengths, but instead experience non-uniform (anisotropic) strain to their bonds and/or changes in coordination environment. Although LDFs by themselves do not indicate whether strain or coordination environment has the stronger effect, separate analysis showed that both of them are important, with contributions of similar magnitude in many cases. For example, the average and standard deviation of LDFs of atoms with first-nearest neighbour coordination deficiencies of 0, 1 and 2 are 456.6 ± 392.4, 1270.0 ± 608.4 and 1483.5 ± 580.0, respectively. The LDF values increase with increasing under-coordination but also have high standard deviations because of large variations in bond strain about atoms with different LAEs.

Clustering analysis of LAEs. To classify the structural environments of atoms at the cores of different GBs into groups suitable for constructing our ML model, we first used the complete-linkage

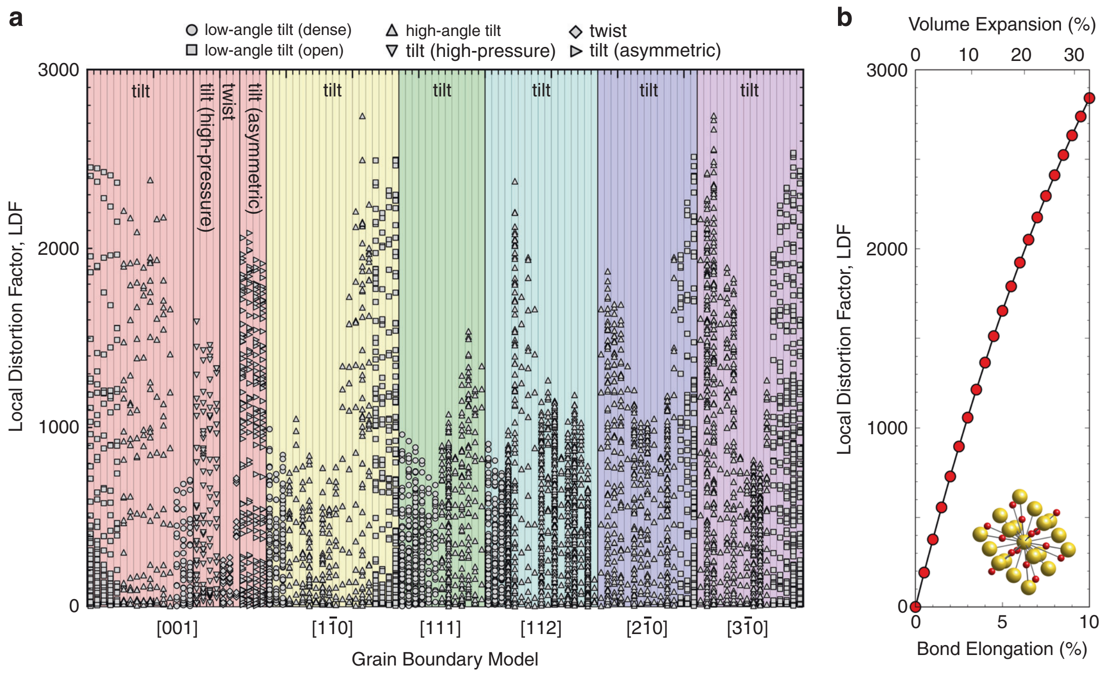

Fig. 2 Local distortion factors, LDFs, obtained using the SOAP descriptor. a LDFs of all LAEs in tilt and twist GB models in order of increasing tilt or twist angle for each class of rotation axis. One vertical column of LDFs corresponds to one GB model. **b** LDFs of atoms in an isotropically expanded unit cell as a function of bond elongation and volume expansion.

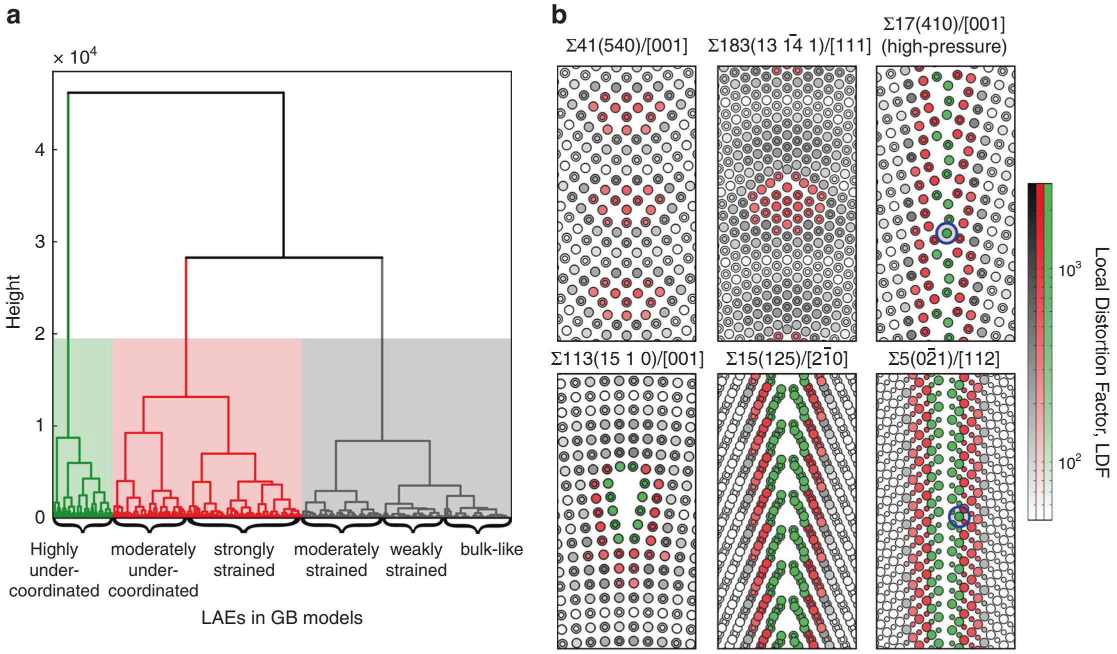

Fig. 3 Hierarchical clustering of GB LAEs. a Hierarchical relationship between LAEs depicted in dendrogram form. The different regions represent three general groups of LAEs: (green) highly under-coordinated (bond-ruptured); (red) moderately under-coordinated or strongly strained; and (grey) moderately strained, weakly strained or bulk-like. **b** Representative distributions of the LAE groups and LDFs at six STGBs. A log scale is used to make it easier to distinguish changes in LDFs within LAE groups.

method to identify LAEs in each GB model based on the dissimilarity metric d between each pair of atoms, before applying Ward's hierarchical clustering method[42] to the complete set of LAEs generated (see Methods for details). Figure 3 shows a dendrogram of the different classes of LAEs identified, together with representative STGBs to illustrate how they are distributed around GBs. The dendrogram in Fig. 3a shows three supergroups of LAEs (indicated by different colour shading in the figure) that are classified into six groups whose members consist of unstrained (bulk-like) atoms, weakly strained atoms, moderately strained atoms, strongly strained atoms, moderately under-coordinated atoms and highly under-coordinated (bond-ruptured) atoms. The averages and standard deviations of LDFs in these six groups are 70.0 ± 66.1, 138.7 ± 42.9, 316.8 ± 84.8, 609.8 ± 140.7, 1032.3 ± 165.6 and 1786.1 ± 323.8, respectively, reflecting the increasing amount of structural distortion (LDF distributions in each LAE group are reported in Supplementary Fig. 3). For reference, from Fig. 2b the LDFs of weakly strained, moderately strained and strongly strained groups correspond to average bond elongations of roughly 0.4, 0.8 and 1.6%, respectively. The average amounts of first-nearest neighbour under-coordination in these groups are 0.00, 0.01, 0.03, 0.22, 0.37 and 0.94, respectively, suggesting that the effect of strongly strained atoms is of similar magnitude to that of slightly under-coordinated atoms.

Figure 3b shows GB structures coloured according to LAE group and LDF values for two low-angle STGBs with dense structures, a low-angle STGB with open structure, a high-pressure high-angle STGB and two standard-pressure high-angle GBs. These indicate that highly under-coordinated atoms occur at open GB core structures, whereas dense GB core structures consist of atoms in strongly strained environments, either at dense low-angle GBs or adjacent to under-coordinated atoms in high-angle STGBs. In dense low-angle GBs such as $\Sigma183(13\,\overline{14}\,1)/[111]$ and $\Sigma113(15\ 1\ 0)/[001]$, atoms between the dislocation cores have LAEs similar to bulk atoms. These results illustrate how hierarchical clustering of LAEs and LDFs captures information regarding the arrangement of atoms and degree of distortion at GBs in a physically interpretable manner.

LDF values quantify the local distortion relative to the ideal crystal bulk, but do not directly measure differences in LAEs between GBs. To better assess the range of LAEs present in different types of GBs, we thus also calculated *d* values between all atoms in one GB model with those in another. This revealed that similar LAEs frequently occur in other GBs, with greater differences occurring for high-pressure and high-angle STGBs than for others. Specifically, the minimum *d* value of any atom in the high-pressure STGBs, asymmetric tilt GBs and twist GBs were no greater than 211, 140 and 87, respectively (compared to maximum LDFs close to 3000); these values correspond to about 0.5%, 0.4% and 0.2% bond elongation, respectively, when considered in terms of a uniformly expanded MgO crystal (Fig. 2b). For example, the *d* value for the two atoms indicated by blue circles in the high-pressure $\Sigma17(410)/[001]$ GB and standard-pressure $\Sigma5(0\bar{2}1)/[112]$ GB in Fig. 3b is only 58.2. In other words, the range of LAEs provided by a sufficiently large and diverse sample of GB structures (92 in our case) is expected to encompass those encountered in GBs with other misorientations, higher complexity or lower symmetry. This result is consistent with Priedman et al.'s observation that different GBs consist of similar structural building blocks or motifs[41]. Consequently, similar to Rosenbrock et al.'s[38] findings for GB energies and mobilities, the properties and behaviour of individual GBs of MgO can be expected to depend on the relative numbers of each type of LAE of which they are composed. Identifying correlations between the numbers and distributions of LAEs in a GB and its thermal conductivity, preferably in a physically meaningful way, should thus allow thermal conductivities of MgO GBs of arbitrary structure to be predicted quickly, accurately and reliably. In the following sections we demonstrate how hierarchical clustering can fulfil this purpose in the context of thermal transport and phonon dispersion, with interpretation facilitated by analysing LDFs.

Thermal conduction at tilt grain boundaries. To determine the dependence of microscopic thermal conduction on structural distortion in the vicinity of GB planes, we calculated atomic thermal conductivities perpendicular to GB planes at 300 K using perturbed MD simulations, and LDFs from the relaxed GB structures for each GB model.

Figure 4 compares plots of LDFs and atomic thermal conductivities of standard- and high-pressure $\Sigma25(710)/[001]$ and $\Sigma5(310)/[001]$ STGBs, together with the LAE classifications identified by hierarchical clustering. These plots reveal that, overall, there is strong negative correlation between LDF and atomic thermal conductivity in these two cases. One exception to this is the standard-pressure $\Sigma5(310)/[001]$ STGB, in which LDFs of the innermost atoms (Fig. 4b) are high and their atomic thermal conductivities (Fig. 4d) are the highest of all atoms in the GB structure. This inversion of the correlation is because the SOAP vector, and hence LDF, are non-directional, whereas there is a large anisotropy in the bond distances and hence components of atomic thermal conductivity of the $\Sigma5(310)/[001]$ GB, with single pairs of atoms across the GB plane acting like thermal conduction bottlenecks. Distances between atoms perpendicular to the GB plane are similar to those in the bulk, but much longer parallel to it in the $[1\bar{3}0]$ direction, resulting in a large LDF factor (maps of the components of atomic thermal conductivity perpendicular and parallel to the GB plane are compared in Supplementary Fig. 4 and Supplementary Note 3). Such bottlenecks generally only occur in high-angle STGBs, but in low densities dispersed between low-conductivity voids, so their effect on the overall thermal conductivity is small.

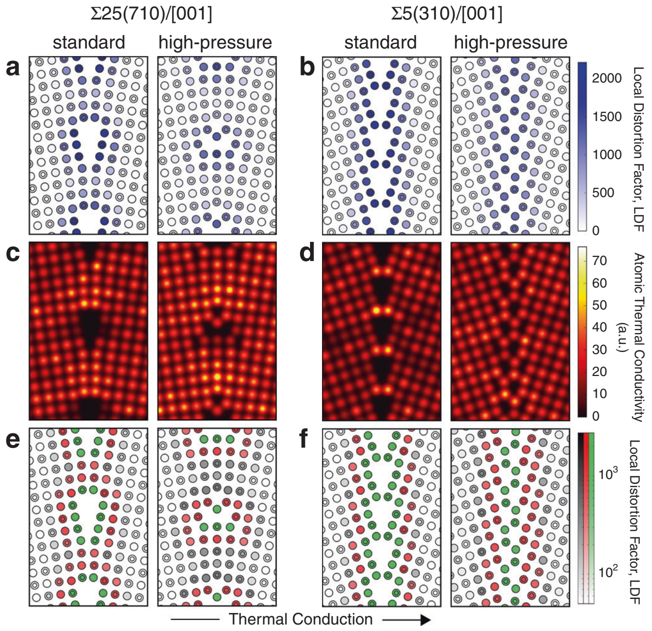

Fig. 4 Atomic configurations and atomic thermal conductivities near GB planes of four STGBs. a, **b** Local distortion factors, LDFs; **c**, **d** Gaussian-smeared atomic thermal conductivities; **e**, **f** Distributions of LAE groups classified from hierarchical clustering. A log scale is used to make it easier to distinguish changes in LDFs within LAE groups.

The greatest decrease in atomic thermal conduction occurs at the centres of dislocation cores, whereas thermal conduction is rapid via atoms in less disturbed (low LDF) regions even if on the GB plane (corresponding to light-coloured atoms in Fig. 4a, b). The core structures of the high-pressure GBs are denser than those of the standard-pressure GBs, making them more like low-angle GBs in which dislocations are arrayed in a regular pattern. This results in the wider regions of unruptured bonds on the GB planes seen in the right-hand images of Fig. 4a, c. This explains why the effective thermal conductivity of the low-angle high-pressure GB is higher than those of the standard-pressure GBs, falling between lines I and I′ in Fig. 1a because of the intermediate atomic densities of its dislocations. Overall, the close correspondence between LDF and atomic thermal conductivity suggests that this metric makes a good descriptor for developing a model for predicting thermal conductivities in a wide variety of GB types of MgO.

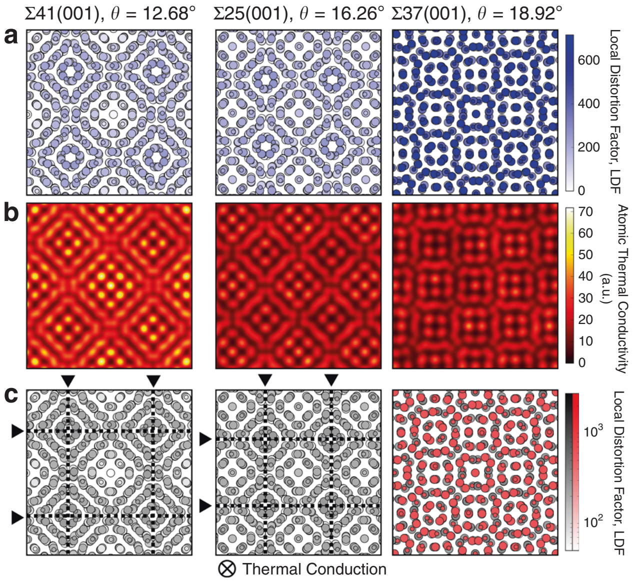

Fig. 5 Atomic configurations and atomic thermal conductivities near GB planes of three twist GBs. a Local distortion factors, LDFs; **b** Gaussian-smeared atomic thermal conductivities; **c** Distributions of LAE groups classified using hierarchical clustering. Dislocation lines are shown as dashed lines in **c**. A log scale is used for LDF values in **c** to make it easier to distinguish differences within LAE groups.

Thermal conduction at twist grain boundaries. In Fig. 5, we compare LDFs and atomic thermal conductivities of three (001) twist GBs, viz. Σ41, Σ25 and Σ37, in order of increasing twist angle. In this case thermal conductivities are projected onto the GB planes, as opposed to parallel to the GB planes in the case of tilt GBs (Fig. 4). In the twist GBs, the LDFs are smaller than those of STGBs (as seen in Fig. 2a), but the structurally distorted sites are widely distributed about the GB plane, which is very different to the case of tilt GBs. In the case of the Σ41 twist GB, the dislocation lines, identified using the method of Stukowski et al.[43], are relatively far apart, and the LDF values are relatively low in the regions between them. These regions serve as thermal conduction highways, evidenced by the close match between regions of low LDF and high atomic thermal conductivity (Fig. 5a, b). In the case of the Σ37 GB, with its relatively high twist angle, all atoms on the GB plane are in distorted environments and the LDFs are uniformly high. The structural distortion thus correlates with low thermal conductivities across the GB plane in contrast to the rapid thermal conduction paths identified in the case of the Σ41 GB.

In contrast to the strong correlation between LDF and atomic thermal conductivity in the case of Σ41 and Σ37 twist GBs, the correlation in the case of the Σ25 twist GB is somewhat weaker. Even though its LDFs are lower than those of the Σ37 GB, especially in the inter-dislocation regions, their atomic thermal conductivities (and hence the effective thermal conductivity of the GB) are similar to those of the Σ37 GB. This difference indicates that the relationship between LDF and atomic thermal conductivity is non-linear; relatively small structural distortions to the lattice are sufficient to dampen the local thermal conduction strongly and thus very high LDFs may not be necessary to suppress thermal transport dramatically. This interpretation is consistent with the slow decrease in effective thermal conductivity exhibited by correlation II in Fig. 1a. Figure 5 also suggests that LDFs may be useful for identifying sites which induce strong phonon scattering and thus lower the effective thermal conductivity in the case of twist GBs as well as for tilt GBs. Further discussion on the utility and limitations of the LDF is provided in Supplementary Note 4.

Prediction models for thermal conductivity. Motivated by the good correlation between LDF and atomic thermal conductivity described in the previous sections, we constructed a mathematical model for predicting thermal conductivities of GBs using multiple linear regression with l_2-norm (or ridge) regularisation. For this, we classified the LAEs into several groups according to the magnitude of their average LDF values by slicing the hierarchical clustering relationships in Fig. 3a in the manner described in Supplementary Fig. 5. We found that classifying the LAEs into six groups, viz., (1) bulk-like, (2) weakly strained, (3) moderately strained, (4) strongly strained, (5) moderately under-coordinated and (6) highly under-coordinated (as shown in Fig. 3a), is sufficient for accurate prediction of GB thermal conductivities. A summary of predictive performance using alternative numbers of LAE groups is also provided as Supplementary Fig. 5 and Supplementary Note 5.

Numbers of LAEs per unit area of a GB, N_m, for each LAE group ($m = 1$–6) were used as predictor variables, and fitting carried out using multiple linear regression (see the Methods section for details). As examples, Fig. 6a, b show the structures of Σ5(310)/[001] and $\Sigma327(17\,\overline{19}\,2)/[111]$ STGBs, the Gaussian weighting function, $G(x)$, and plots of their N_m values for each LAE group. These show that there are only highly distorted LAEs in the vicinity of the high-angle Σ5(310)/[001] GB whereas there are both bulk-like and moderately distorted LAEs in the vicinity of the low-angle $\Sigma327(17\,\overline{19}\,2)/[111]$ GB.

The predictor model was trained using data from 70 randomly chosen symmetric GBs, and then validated using data from the remaining 22 GBs, including all four asymmetric tilt GBs. Figure 6c shows a parity plot of overall thermal conductivities calculated using perturbed MD against values predicted by the model. The root mean squared error (RMSE) and R^2 value are 1.28 $\mathrm{W m^{-1} K^{-1}}$ and 0.93, respectively, for the training data, and 1.30 $\mathrm{W m^{-1} K^{-1}}$ and 0.92, respectively, for the test data. These results demonstrate that GB thermal conductivity can be predicted with high precision from their local atomic structures alone, regardless of whether the GB is under standard or high pressure, a tilt, twist or twin GB. The prediction model also reliably estimated thermal conductivities of the asymmetric tilt GBs, confirming its good transferability as well as the efficacy of including a wide range of GB types in the training dataset. In addition, as seen in Fig. 6d, the regression coefficient is very high in the case of LAE group 1, where LDFs are very small (70.0 on average), i.e., the local environments are very similar to those in the crystal bulk, and very low for the other LAE groups decreasing gradually as LDF increases. These results again suggest that introducing GBs with relatively small structural distortions (e.g., low-angle GBs with dense GB cores) is an effective strategy for reducing thermal conductivity dramatically.

Discussion

Similar to point defects such as vacancies, impurity atoms and interstitial atoms[44], GBs are known to limit phonon MFPs by causing diffuse scattering, and this is consistent with the results of our perturbed MD simulations. GBs can be thought of as extended planar defects or clusters of point defects, typically a few nanometres wide, so that deviations from the ideal lattice in the vicinity of GBs, as reflected in their LAEs and LDFs, are typically much larger than for isolated defects, making them able to scatter long-wavelength phonons much more effectively, resulting in much shorter MFPs in a polycrystal than in single crystal (in which MFPs are on the order of hundreds of nanometres or

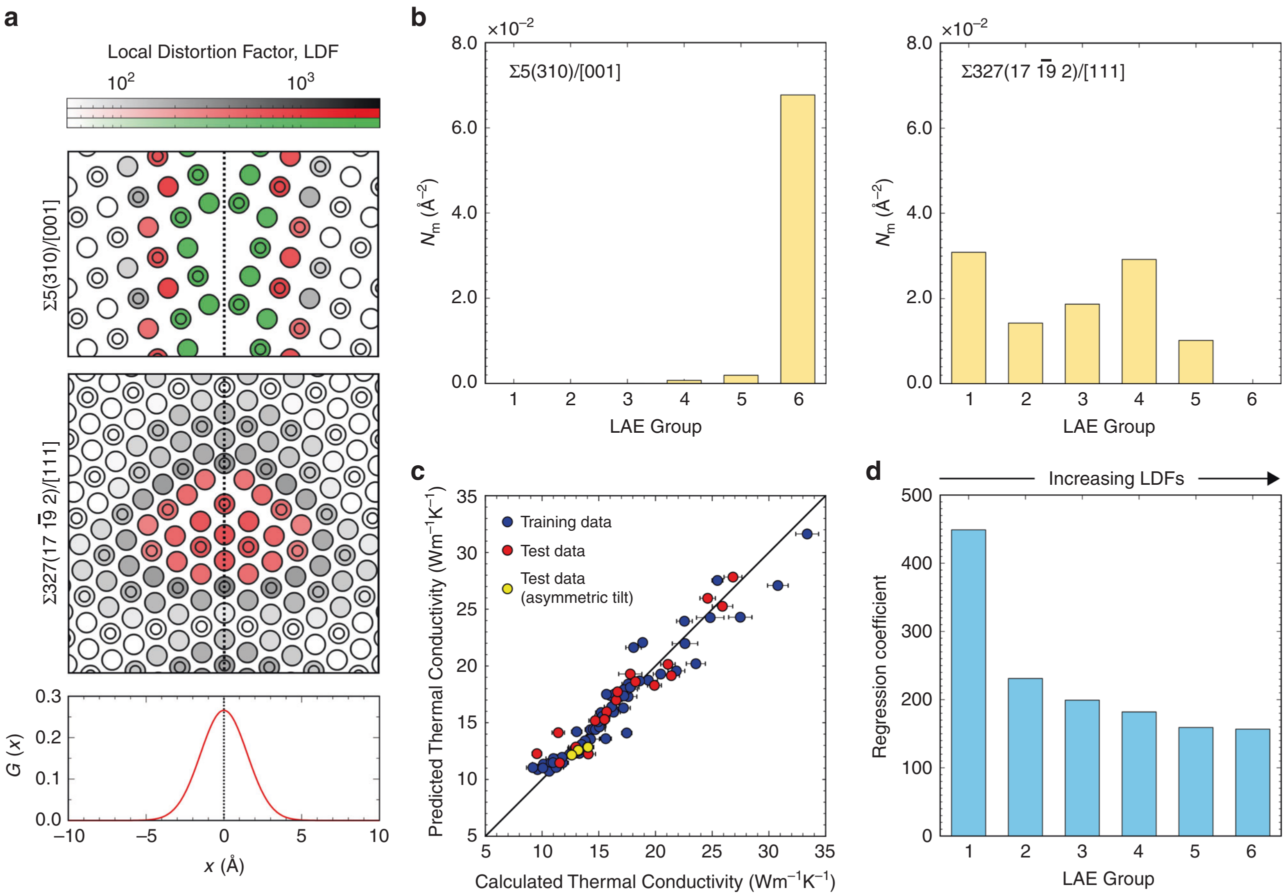

Fig. 6 Regression modelling of thermal conductivity at GBs of MgO. a, **b** Example of how predictor (input) variables N_m were generated from GB structures for multiple linear regression. **a** LDFs in the vicinity of high-angle Σ5(310)/[001] and low-angle Σ327(17 $\bar{1}\bar{9}$ 2)/[111] STGBs, and the Gaussian function $G(x)$ centred on the GB plane used in calculating N_m. A log scale is used for LDF values to make it easier to distinguish differences within LAE groups. **b** Number of atoms per unit area in each LAE group, N_m, using hierarchical clustering results for the two GBs. **c** Parity plot of calculated against predicted GB thermal conductivities. Error bars indicate standard deviations in thermal conductivity calculated using perturbations of different magnitudes. **d** Ridge regression coefficients for N_m of each LAE group. The higher the LAE group number, the larger the LDF values in the group.

several micrometres in the case of single crystal MgO[45]). Constructing an ML model with data from MD simulations of GBs shows that these effects can be predicted accurately from analysis of LAEs calculated with only a short cutoff (~4.5 Å).

The correlation between GB structure and thermal conductivity identified in this study should enable polycrystalline materials to be designed with more precisely controlled thermal conductivities, e.g., by identifying GBs with the desired microscopic behaviour for a given application and facilitating their formation in the material with appropriate synthesis methods and conditions. Although it is still very difficult to engineer GB structures directly at the atomic level, it is possible to increase the probability of their formation by tailoring grain orientation through thermal treatment, mechanical processing, use of substrates, and so on, as grains coming into contact within a narrower range of orientations are more likely to exhibit a particular GB structure with the desired LAEs. It should also be possible to examine the effect of dopants on GB thermal conductivities using this model, assuming suitable potential parameters are available for performing MD simulations, although the number of simulations required may increase substantially as a result of the increased degrees of freedom (dopant concentration, segregation sites and so on). Nevertheless, extending the ML method developed in this study to more complex crystal structures and compounds should enable a more comprehensive understanding of GB structure-property relationships to be obtained, so that the next-generation of thermal materials can be designed more efficiently and effectively.

The method presented here, in which the relationship between thermal conductivity and local atomic distortions is identified through ML with a multidimensional dataset, can be readily applied to other structure-property relationships because of the universality of the SOAP descriptor, whether the cause of the distortion is point defects (isolated or clustered), dislocations, GBs, heterointerfaces or surfaces. When used in conjunction with a large dataset of defective structures such as those generated by atomistic materials modelling[46–48] using reliable interatomic potentials, quantification of complex structure-property relationships using ML techniques with SOAP-derived metrics has the potential to provide deeper insights into complex interface phenomena and greatly accelerate materials design of a broad range of technologically important materials. In some situations, however, it may be necessary to include directional information in the model so that properties more sensitive to anisotropy or that are highly directional can be predicted accurately. Methods for including directional information are discussed briefly in Supplementary Note 3 as a stimulus for future work.

In summary, we have used ML with data derived from the SOAP descriptor and perturbed MD to quantify the relationship between local atomic structure and overall thermal conductivity in standard- and high-pressure STGBs, twin, twist and asymmetric tilt GBs of MgO. The LDF, a simple metric based on the

SOAP descriptor, was found to correlate well with atomic thermal conductivity in a non-linear fashion. The prediction model constructed based on this insight revealed that even small structural distortions at GBs can reduce thermal conductivity dramatically, suggesting that the thermal conductivity of a polycrystalline material may be closely controlled by tailoring the number and distribution of such GBs through GB engineering. Although the importance of structural disorder at GBs has been posited by earlier researchers[20,49], to the best of our knowledge this is the first study to demonstrate quantitatively the correlation between structural distortion and suppression of thermal conductivity at the atomic level.

Methods

GB model construction. Eighty-one standard-pressure STGBs of MgO constructed previously[25] were used together with an additional three (001) twist GBs, four [001] asymmetric tilt GBs, and four high-pressure STGBs generated using the method described previously[25,50]. Simulated annealing (SA) of initial structures was performed to obtain the stable atomic configurations of the GBs using equilibrium MD methods encoded in the Large-scale Atomic/Molecular Massively Parallel Simulator (LAMMPS) programme[51]. Initial configurations were constructed by tilting or twisting two half-crystals by a specific angle, and sandwiching an amorphous block of MgO between them. The amorphous block was obtained from a separate MD calculation by heating a perfect crystal of MgO to 8000 K. The rigid-ion Buckingham potential for MgO reported by Landuzzi et al.[52] was used in all cases.

SA simulations commenced with the GB model heated to 4000 K, and the temperature was decreased gradually to 50 K over 330 ps. This gradual cooling from high temperature allowed the atoms in the amorphous region to diffuse and find energetically favourable positions, so that a low-energy ordered GB structure was obtained for each initial configuration. The final atomic configuration for each GB model was obtained by performing geometry optimisation (at 0 GPa) using the General Utility Lattice Program (GULP)[53] on the structures obtained from SA simulations. In several cases, metastable GB structures (GBs with higher energies than the most stable form for that GB orientation at 0 GPa with atoms trapped in higher-energy local minima) were also obtained. These GB structures became lower in energy than the stable GB structures when geometry-optimised at higher pressures using GULP, so these were included as examples of high-pressure STGBs when developing the ML model.

We repeated the SA simulations 10 times for each symmetric GB and 50 times for each asymmetric GB using different initial velocity distributions to confirm that the most energetically stable atomic arrangement had been obtained. Structures of the $\Sigma5$ (310)/[001] GB were found to be in agreement with that determined using first-principles calculations[54], and a few dislocation core structures, which can be seen in low-angle STGBs with [001] and $[1\bar{1}0]$ rotation axes, e.g., $\Sigma41(540)/[001]$ and $\Sigma51(1\ 1\ 10)/[1\bar{1}0]$ GBs, were found to be in excellent agreement with those observed by scanning transmission electron microscopy[25,55]. This gives us confidence that we successfully identified the lowest-energy (ground-state) structures. These GB models are available as Supplementary Data 1 in LAMMPS format. Two GB structure models are illustrated in Supplementary Fig. 6 as examples.

The excess volume per unit area of each GB, ΔV^{GB}, was calculated using the following equation:

$$\Delta V^{\mathrm{GB}} = \frac{V^{\mathrm{GB}} - \frac{N^{\mathrm{GB}}}{N^{\mathrm{SC}}} V^{\mathrm{SC}}}{2A} = \frac{V^{\mathrm{GB}} - N^{\mathrm{GB}}/\rho^{\mathrm{SC}}}{2A} \qquad (1)$$

where V^{GB} and V^{SC} are the volume of the GB model and unit cell, respectively, N^{GB} and N^{SC} are the number of atoms in the GB model and unit cell, respectively, and ρ^{SC} is the number density of the unit cell.

SOAP descriptor. SOAP vectors of all atoms in MgO GBs were calculated using the Python-based software DScribe[56]. The SOAP descriptor is derived by fitting a set of spherical harmonics and radial basis functions to the 3-dimensional density distribution generated by placing Gaussian-smeared atomic densities on atoms within a specified cutoff radius about a central atom. The coefficients of the fit form a rotationally invariant power spectrum[57] which is compiled into a SOAP vector for that atom which contains all the information needed to reconstruct the LAE. Compiling SOAP vectors of atoms in the GB model into a matrix known as the local environment representation allows each particular GB structure to be described quantitatively and uniquely[38,41]. One of the advantages of the SOAP descriptor is that it also makes it possible to compare LAEs quantitatively, so that a dissimilarity (or, conversely, similarity) metric can be defined between two atoms[33] which varies smoothly with a change in neighbouring atom positions[38]. In this study, we used a non-normalised dissimilarity metric, d, defined as

$$d_{ij} = \sqrt{\mathbf{p}_i \cdot \mathbf{p}_i + \mathbf{p}_j \cdot \mathbf{p}_j - 2\mathbf{p}_i \cdot \mathbf{p}_j} \qquad (2)$$

where $\mathbf{p}_i$ and $\mathbf{p}_j$ are the SOAP vectors of two atoms i and j. If $\mathbf{p}_i$ and $\mathbf{p}_j$ are the SOAP vectors of a GB atom and its equivalent crystal bulk atom, the dissimilarity metric represents how much the LAE of the GB atom differs from that of the bulk atom. We refer to this as the local distortion factor, LDF, defined as

$$\mathrm{LDF} = \sqrt{\mathbf{p}_{\mathrm{GB}} \cdot \mathbf{p}_{\mathrm{GB}} + \mathbf{p}_{\mathrm{bulk}} \cdot \mathbf{p}_{\mathrm{bulk}} - 2\mathbf{p}_{\mathrm{GB}} \cdot \mathbf{p}_{\mathrm{bulk}}} \qquad (3)$$

where $\mathbf{p}_{\mathrm{GB}}$ and $\mathbf{p}_{\mathrm{bulk}}$ are the SOAP vectors of a GB atom and an atom in the crystal bulk, respectively. A cutoff of 4.461 Å, corresponding to the average of the fourth and fifth nearest neighbour distances in MgO, was selected after preliminary testing of cutoffs both shorter and longer.

To compare LAEs and GB excess volume quantitatively, we defined the term total distortion factor, TDF, to be the sum of all LDFs at a GB normalised to the GB cross-sectional area, A,

$$\mathrm{TDF} = \sum_i \mathrm{LDF}_i/2A \qquad (4)$$

where i is the index of an atom in the GB model. TDF is divided by two because each GB model produces two GBs under periodic boundary conditions. The calculated TDF and GB excess volume exhibited a linear relationship, especially in the case of high-angle tilt GBs formed under standard pressure (see Supplementary Fig. 7 and Supplementary Note 6). We also calculated the LDFs and TDFs using cutoffs of 3.313 and 3.923 Å, and confirmed that the relationship between TDF and excess volume was not overly sensitive to the choice of cutoff. Using large cutoff radii (~10 Å or greater) made it difficult to identify the GB core structure because it resulted in many more atoms being classified as having under-coordinated atoms in their spheres of influence.

The maximum degree of spherical harmonics, l_{max}, and the number of radial basis functions, n_{max}, were set to 9 and 12, respectively. In test calculations, it was found that the linear relationship between TDF and excess volume was insensitive to l_{max} (even 0 produced similar results) but n_{max} needed to be sufficiently large to achieve a good linear fit. We used spherical Gaussian type orbitals (as defined in Himanen et al.[56]) as radial basis functions, with a Gaussian width of 0.5 Å. Another implementation of the SOAP descriptor, the QUIP code[58], was also tested, and produced essentially the same linear relationship as DScribe (see Supplementary Fig. 8), indicating that the results reported here do not depend strongly on the particular implementation of the SOAP descriptor.

To extract a unique set of LAEs from each GB model in Fig. 2a, we performed complete-linkage clustering as implemented in Scipy[59] so that all combinations of atoms in each LAE group had d values below a threshold value of 30.0. The threshold value was carefully chosen to maximise the performance of the prediction model without compromising interpretability of the classification groups. We also tested normalised forms of the SOAP vectors and other dissimilarity metrics such as the SOAP kernel and Gaussian kernel, but found that they make interpretation of the hierarchical clustering results difficult and reduce the predictive performance of the model. Further details are given in Supplementary Methods.

Thermal conductivity calculations. Overall thermal conductivities across the GB planes and grain interiors, which we refer to as effective thermal conductivities, were calculated using the perturbed MD method[60] for a few high-pressure tilt, twist and asymmetric tilt GB structures at 300 K. Custom-written code was added to LAMMPS for this purpose. In this method, lattice thermal conductivity in the x direction is calculated according to

$$\kappa_{\mathrm{lattice}} = \frac{1}{F_{\mathrm{ext}} T} \lim_{t \to \infty} \langle J_x \rangle_t \qquad (5)$$

where F_{ext} is the magnitude of the perturbation, T is the absolute temperature and J_x is the heat flux in the x direction. The microscopic heat flux is defined by Irving and Kirkwood[61] to be

$$\mathbf{J} = \sum_i \mathbf{J}_i = \sum_i \frac{1}{2V} \left[\left\{ m_i \mathbf{v}_i^2 \mathbf{I} + \sum_j \phi_{ij} \mathbf{I} \right\} \mathbf{v}_i - \sum_j \left(\mathbf{F}_{ij} \cdot \mathbf{v}_i \right) \mathbf{r}_{ij} \right] \qquad (6)$$

where $\mathbf{J}_i$ is the atomic contribution of atom i to the heat flux, V is the volume of the GB model (supercell), m_i and $\mathbf{v}_i$ are the mass and velocity of atom i, respectively, ϕ_{ij} is the interatomic potential energy between atoms i and j, $\mathbf{I}$ is a unit tensor of second rank and $\mathbf{F}_{ij}$ is the force exerted by atom j on atom i. By substituting Eq. 6 into Eq. 5, atomic thermal conductivities κ_i, which are the atomic contributions to overall lattice thermal conductivity, can be calculated according to

$$\kappa_{\mathrm{lattice}} = \sum_i \kappa_i = \sum_i \frac{1}{F_{\mathrm{ext}} T} \lim_{t \to \infty} \langle J_{i,x} \rangle_t \qquad (7)$$

where $J_{i,\,x}$ is the contribution of atom i to the heat flux in the x direction. As seen in Eq. 6, atomic thermal conductivities are proportional to the inverse of the supercell volume, and thus must be normalised by multiplying the supercell volume for comparison between GB models. In addition, because the intensities in the thermal conductivity map in Figs. 4 and 5 also depend on the number of atoms in the depth direction, Gaussian-smeared atomic thermal conductivities projected onto the two-dimensional planes were divided by the cell depth. This procedure for calculating thermal conductivity is the same as reported in our previous work on STGBs[25]: For each GB orientation, models were constructed with three different half-crystal widths (distances between GB planes of as close to 4, 5 and 6 nm as feasible for that particular misorientation) by altering the number of bulk layers. MD simulations were then performed in the NPT ensemble for 100 ps with a timestep of 1 fs for each model to determine its equilibrium cell dimensions at 300 K. Next, an NVT ensemble was applied for 100 ps with temperature scaling, followed by 300 ps using a Nosé-Hoover thermostat, to ensure thermal equilibrium had been reached. Perturbed MD simulations were then performed on the equilibrated GB models for 1.1 ns and the average heat flux of the last 1.0 ns used to calculate the thermal conductivity. The first 0.1 ns of data was discarded because this was the time needed for the system to transition from thermal equilibrium to a steady state under the perturbation. For each model, perturbed MD simulations were performed with at least four different magnitudes of the perturbation (after confirming the response was within the linear regime) and the average thermal conductivity calculated. The effective thermal conductivity for a width of exactly 5 nm was then extracted from a linear regression fit to these averaged thermal conductivities. Atomic thermal conductivities, plotted in Figs. 4 and 5, were extracted from the GB models with half-crystal widths of about 5 nm. Further details on the perturbed MD method are also available elsewhere[60,62–64].

Machine learning. LAEs identified for each GB model using the complete-linkage algorithm were grouped and classified using Ward's minimum variance method of hierarchical clustering[42] as implemented in SciPy[59], again using the dissimilarity metric d in Eq. 2, as it is equivalent to the Euclidean distance. We also tested several other methods, such as the average method, but Ward's method was found to perform the most reliably and consistently. With this method, LAEs in the various GB structures were grouped into six different categories within three supergroups based on their level of lattice distortion.

The prediction model for thermal conductivity was constructed using the number of LAEs per unit area of a GB in each LAE group m, N_m, as input variables. Values of N_m were weighted by a Gaussian function, G, of the distance, x, of the LAE's atom from the GB plane according to

$$N_m = \frac{1}{A}\sum_i^n G(x) = \frac{1}{A}\sum_i^n \frac{1}{\sqrt{2\pi\sigma^2}}\exp\left(-\frac{x^2}{2\sigma^2}\right) \tag{8}$$

where A is the GB cross-sectional area, n is the number of atoms in the LAE group, i is the index of an atom in the LAE group, and σ is the variance (set to 1.5 Å). N_m corresponds to the number density of atoms in the vicinity of the GB plane decomposed into the contribution of each LAE group.

Fitting was performed using regularised multiple linear regression (Ridge regression) as implemented in scikit-learn[65]. Ridge regression shrinks the regression coefficients, $\boldsymbol{\beta}$, to prevent overfitting to the training data, by penalizing their size according to

$$\boldsymbol{\beta} = \underset{\boldsymbol{\beta}}{\operatorname{argmin}}\left\{\sum_i^t\left(y_i - \beta_0 - \sum_j^p x_{ij}\beta_j\right)^2 + \lambda\sum_j^p \beta_j^2\right\} \tag{9}$$

where t is the number of training data, y_i is the ith observed value, p is the number of input variables, x_{ij} is the jth component of the input variable for the ith training datum, β_0 and β_j are the intercept and the jth regression coefficients, respectively, and λ is the regularization parameter[66]. Because thermal conductivity should be zero when all N_m are zero, i.e., there are no atoms in the vicinity of the GB plane, in this study the intercept β_0 was set to zero. For training data, 70 of the symmetric GB models were randomly selected with the proviso that each class of GB (namely, the six types of tilt GBs grouped by rotation axis, low-angle tilt GBs (open or dense), high-angle tilt GBs, twist GBs and high-pressure GBs) was represented at least once. The model was trained using $\lambda = 3\times10^{-4}$, determined through cross-validation. The remaining 18 symmetric GBs and all four asymmetric tilt GBs were used as test data to estimate the predictive performance. Input values N_m were not standardised because this was found to reduce the predictive performance of the model.

Data availability

GB models used in this study are available as Supplementary Data 1. Effective thermal conductivities of all the GB models used in multiple linear regression are summarised in Supplementary Tables 1 to 9. All other data that support the findings of this study are available from one of corresponding authors S.F. upon request.

Code availability

Details of computer codes used in this study are provided in Supplementary Methods.

Received: 22 October 2019; Accepted: 13 March 2020;

References

1. Biswas, K. et al. High-performance bulk thermoelectrics with all-scale hierarchical architectures. *Nature* **489**, 414–418 (2012).
2. He, J. & Tritt, T. M. Advances in thermoelectric materials research: looking back and moving forward. *Science* **357**, eaak9997 (2017).
3. Kim, S. I. et al. Dense dislocation arrays embedded in grain boundaries for high-performance bulk thermoelectrics. *Science* **348**, 109–114 (2015).
4. Padture, N. P. Advanced structural ceramics in aerospace propulsion. *Nat. Mater.* **15**, 804–809 (2016).
5. Yang, H. S., Bai, G. R., Thompson, L. J. & Eastman, J. A. Interfacial thermal resistance in nanocrystalline yttria-stabilized zirconia. *Acta Mater.* **50**, 2309–2317 (2002).
6. Cahill, D. G. et al. Nanoscale thermal transport. II. 2003-2012. *Appl. Phys. Rev.* **1**, 011305 (2014).
7. Li, S. et al. High thermal conductivity in cubic boron arsenide crystals. *Science* **361**, 579–581 (2018).
8. Cahill, D. G. et al. Nanoscale thermal transport. *J. Appl. Phys.* **93**, 793–818 (2003).
9. Losego, M. D., Grady, M. E., Sottos, N. R., Cahill, D. G. & Braun, P. V. Effects of chemical bonding on heat transport across interfaces. *Nat. Mater.* **11**, 502–506 (2012).
10. Poudel, B. et al. High-thermoelectric performance of nanostructured bismuth antimony telluride bulk alloys. *Science* **320**, 634–638 (2008).
11. Ibáñez, M. et al. High-performance thermoelectric nanocomposites from nanocrystal building blocks. *Nat. Commun.* **7**, 1–7 (2016).
12. Wang, Z., Alaniz, J. E., Jang, W., Garay, J. E. & Dames, C. Thermal conductivity of nanocrystalline silicon: Importance of grain size and frequency-dependent mean free paths. *Nano Lett.* **11**, 2206–2213 (2011).
13. Nakamura, Y. et al. Anomalous reduction of thermal conductivity in coherent nanocrystal architecture for silicon thermoelectric material. *Nano Energy* **12**, 845–851 (2015).
14. Ju, S. & Liang, X. Thermal conductivity of nanocrystalline silicon by direct molecular dynamics simulation. *J. Appl. Phys.* **112**, 064305 (2012).
15. Dong, H., Wen, B. & Melnik, R. Relative importance of grain boundaries and size effects in thermal conductivity of nanocrystalline materials. *Sci. Rep.* **4**, 7037 (2014).
16. Aketo, D., Shiga, T. & Shiomi, J. Scaling laws of cumulative thermal conductivity for short and long phonon mean free paths. *Appl. Phys. Lett.* **105**, 131901 (2014).
17. Sood, A. et al. Direct visualization of thermal conductivity suppression due to enhanced phonon scattering near individual grain boundaries. *Nano Lett.* **18**, 3466–3472 (2018).
18. Tai, K., Lawrence, A., Harmer, M. P. & Dillon, S. J. Misorientation dependence of Al_2O_3 grain boundary thermal resistance. *Appl. Phys. Lett.* **102**, 034101 (2013).
19. Xu, D. et al. Thermal boundary resistance correlated with strain energy in individual Si film-wafer twist boundaries. *Mater. Today Phys.* **6**, 53–59 (2018).
20. Schelling, P. K., Phillpot, S. R. & Keblinski, P. Kapitza conductance and phonon scattering at grain boundaries by simulation. *J. Appl. Phys.* **95**, 6082–6091 (2004).
21. Watanabe, T., Ni, B., Phillpot, S. R., Schelling, P. K. & Keblinski, P. Thermal conductance across grain boundaries in diamond from molecular dynamics simulation. *J. Appl. Phys.* **102**, 063503 (2007).
22. Bagri, A., Kim, S. P., Ruoff, R. S. & Shenoy, V. B. Thermal transport across twin grain boundaries in polycrystalline graphene from nonequilibrium molecular dynamics simulations. *Nano Lett.* **11**, 3917–3921 (2011).
23. Chernatynskiy, A., Bai, X. M. & Gan, J. Systematic investigation of the misorientation- and temperature-dependent Kapitza resistance in CeO_2. *Int. J. Heat Mass Transf.* **99**, 461–469 (2016).
24. Yeandel, S. R., Molinari, M. & Parker, S. C. The impact of tilt grain boundaries on the thermal transport in perovskite $SrTiO_3$ layered nanostructures. A computational study. *Nanoscale* **10**, 15010–15022 (2018).
25. Fujii, S., Yokoi, T. & Yoshiya, M. Atomistic mechanisms of thermal transport across symmetric tilt grain boundaries in MgO. *Acta Mater.* **171**, 154–162 (2019).
26. Wolf, D. Structure-energy correlation for grain boundaries in F.C.C. metals–III. Symmetrical tilt boundaries. *Acta Metall. Mater.* **38**, 781–790 (1990).
27. Wolf, D. Structure-energy correlation for grain boundaries in f.c.c. metals–IV. Asymmetrical twist (general) boundaries. *Acta Metall. Mater.* **38**, 791–798 (1990).
28. Homer, E. R., Patala, S. & Priedeman, J. L. Grain boundary plane orientation fundamental zones and structure-property relationships. *Sci. Rep.* **5**, 1–13 (2015).
29. Priester, L. *Grain Boundaries: From Theory To Engineering, Springer Series In Materials Science*, Vol. 172 (Springer, 2013).
30. Cantwell, P. R. et al. Grain boundary complexions. *Acta Mater.* **62**, 1–48 (2014).
31. Schoenholz, S. S., Cubuk, E. D., Sussman, D. M., Kaxiras, E. & Liu, A. J. A structural approach to relaxation in glassy liquids. *Nat. Phys.* **12**, 469–472 (2016).

32. Ramprasad, R., Batra, R., Pilania, G., Mannodi-Kanakkithodi, A. & Kim, C. Machine learning in materials informatics: recent applications and prospects. *npj Comput. Mater.* **3**, 54 (2017).
33. Patala, S. Understanding grain boundaries – The role of crystallography, structural descriptors and machine learning. *Comput. Mater. Sci.* **162**, 281–294 (2019).
34. Konstantinou, K., Mocanu, F. C., Lee, T. H. & Elliott, S. R. Revealing the intrinsic nature of the mid-gap defects in amorphous $Ge_2Sb_2Te_5$. *Nat. Commun.* **10**, 3065 (2019).
35. Jäger, M. O. J., Morooka, E. V., Federici Canova, F., Himanen, L. & Foster, A. S. Machine learning hydrogen adsorption on nanoclusters through structural descriptors. *npj Comput. Mater.* **4**, 37 (2018).
36. Sharp, T. A. et al. Machine learning determination of atomic dynamics at grain boundaries. *Proc. Natl Acad. Sci. USA* **115**, 10943–10947 (2018).
37. Tomoyuki, T. et al. Fast and scalable prediction of local energy at grain boundaries: machine-learning based modeling of first-principles calculations. *Model. Simul. Mater. Sci. Eng.* **25**, 75003 (2017).
38. Rosenbrock, C. W., Homer, E. R., Csányi, G. & Hart, G. L. W. Discovering the building blocks of atomic systems using machine learning: application to grain boundaries. *npj Comput. Mater.* **3**, 1–7 (2017).
39. Bartók, A. P., Kondor, R. & Csányi, G. On representing chemical environments. *Phys. Rev. B* **87**, 1–16 (2013).
40. Bartók, A. P., Kondor, R. & Csányi, G. Erratum: on representing chemical environments [Phys. Rev. B 87, 184115 (2013)]. *Phys. Rev. B* **96**, 9–10 (2017).
41. Priedeman, J. L., Rosenbrock, C. W., Johnson, O. K. & Homer, E. R. Quantifying and connecting atomic and crystallographic grain boundary structure using local environment representation and dimensionality reduction techniques. *Acta Mater.* **161**, 431–443 (2018).
42. Ward, J. H. Hierarchical grouping to optimize an objective function. *J. Am. Stat. Assoc.* **58**, 236–244 (1963).
43. Stukowski, A., Bulatov, V. V. & Arsenlis, A. Automated identification and indexing of dislocations in crystal interfaces. *Model. Simul. Mater. Sci. Eng.* **20**, 085007 (2012).
44. Ren, G. K. et al. Contribution of point defects and nano-grains to thermal transport behaviours of oxide-based thermoelectrics. *npj Comput. Mater.* **2**, 1–9 (2016).
45. Wilson, R. B. & Cahill, D. G. Limits to Fourier theory in high thermal conductivity single crystals. *Appl. Phys. Lett.* **107**, 203112 (2015).
46. Kiyohara, S., Oda, H., Miyata, T. & Mizoguchi, T. Prediction of interface structures and energies via virtual screening. *Sci. Adv.* **2**, e1600746 (2016).
47. Yonezu, T., Tamura, T., Takeuchi, I. & Karasuyama, M. Knowledge-transfer-based cost-effective search for interface structures: a case study on fcc-Al [110] tilt grain boundary. *Phys. Rev. Mater.* **2**, 1–9 (2018).
48. Zhu, Q., Samanta, A., Li, B., Rudd, R. E. & Frolov, T. Predicting phase behavior of grain boundaries with evolutionary search and machine learning. *Nat. Commun.* **9**, 467 (2018).
49. Spiteri, D., Anaya, J. & Kuball, M. The effects of grain size and grain boundary characteristics on the thermal conductivity of nanocrystalline diamond. *J. Appl. Phys.* **119**, 085102 (2016).
50. Yokoi, T. & Yoshiya, M. Atomistic simulations of grain boundary transformation under high pressures in MgO. *Phys. B* **532**, 2–8 (2018).
51. Plimpton, S. Fast Parallel Algorithms for Short-range molecular dynamics. *J. Comput. Phys.* **117**, 1–19 (1995).
52. Landuzzi, F. et al. Molecular dynamics of ionic self-diffusion at an MgO grain boundary. *J. Mater. Sci.* **50**, 2502–2509 (2015).
53. Gale, J. D. GULP: a computer program for the symmetry-adapted simulation of solids. *J. Chem. Soc. Faraday Trans.* **93**, 629–637 (1997).
54. Yan, Y. et al. Impurity-induced structural transformation of a MgO grain boundary. *Phys. Rev. Lett.* **81**, 3675–3678 (1998).
55. Wang, Z., Saito, M., McKenna, K. P. & Ikuhara, Y. Polymorphism of dislocation core structures at the atomic scale. *Nat. Commun.* **5**, 3239 (2014).
56. Himanen, L. et al. DScribe: library of descriptors for machine learning in materials science. *Comput. Phys. Commun.* **247**, 106949 (2019).
57. De, S., Bartók, A. P., Csányi, G. & Ceriotti, M. Comparing molecules and solids across structural and alchemical space. *Phys. Chem. Chem. Phys.* **18**, 13754–13769 (2016).
58. Bartók, A. P., Payne, M. C., Kondor, R. & Csányi, G. Gaussian approximation potentials: the accuracy of quantum mechanics, without the electrons. *Phys. Rev. Lett.* **104**, 1–4 (2010).
59. Jones, E., et al. SciPy: Open Source Scientific Tools for Python, http://www.scipy.org/ (2001).
60. Yoshiya, M., Harada, A., Takeuchi, M., Matsunaga, K. & Matsubara, H. Perturbed molecular dynamics for calculating thermal conductivity of zirconia. *Mol. Simul.* **30**, 953–961 (2004).
61. Irving, J. H. & Kirkwood, J. G. The statistical mechanical theory of transport processes. IV. The equations of hydrodynamics. *J. Chem. Phys.* **18**, 817 (1950).
62. Fujii, S., Yoshiya, M. & Fisher, C. A. J. Quantifying Anharmonic Vibrations in Thermoelectric Layered Cobaltites and Their Role in Suppressing Thermal Conductivity. *Sci. Rep.* **8**, 11152 (2018).
63. Fujii, S. et al. Impact of dynamic interlayer interactions on thermal conductivity of $Ca_3Co_4O_9$. *J. Electron. Mater.* **43**, 1905–1915 (2014).
64. Fujii, S. & Yoshiya, M. Manipulating Thermal Conductivity by Interfacial Modification of Misfit-Layered Cobaltites $Ca_3Co_4O_9$. *J. Electron. Mater.* **45**, 1217–1226 (2016).
65. Pedregosa, F. et al. Scikit-learn: Machine Learning in Python. *J. Mach. Learn. Res.* **12**, 2825–2830 (2011).
66. Hastie, T., Tibshirani, R. & Friedman, J. The Elements of Statistical Learning: Data Mining, Inference, and Prediction, Second Edition (Springer, 2017).

Acknowledgements

This work was supported by “Materials Research by Information Integration” Initiative (MI^2I) project of the Support Program for Starting Up Innovation Hub from the Japan Science and Technology Agency (JST) and Grant-in-Aid for Scientific Research on Innovative Areas ‘New Materials Science on Nanoscale Structures and Functions of Crystal Defect Cores’ from the Japan Society for the Promotion of Science (JSPS) [grant number 19H05786].

Author contributions

S.F. conceived the research idea, carried out theoretical calculations, performed machine learning and wrote the paper. C.A.J.F and T.Y. contributed to writing of the paper with oversight by M.Y. T.Y. constructed grain boundary models. M.Y., C.A.J.F. and H.M. advised on the machine learning method and interpretation of results. All authors discussed the results, and read and commented on the paper.

Competing interests

The authors declare no competing interests.

Additional information

Supplementary information is available for this paper at https://doi.org/10.1038/s41467-020-15619-9.

Correspondence and requests for materials should be addressed to S.F. or M.Y.

Peer review information *Nature Communications* thanks Srikanth Patala and Keith McKenna for their contribution to the peer review of this work. Peer reviewer reports are available.

Reprints and permission information is available at http://www.nature.com/reprints

Scripta Materialia 202 (2021) 113991

Contents lists available at ScienceDirect

Scripta Materialia

journal homepage: www.elsevier.com/locate/scriptamat

Direct numerical analyses of nanoscale thermal transport near MgO edge dislocations

Wataru Sekimoto[a], Susumu Fujii[a,b], Masato Yoshiya[a,b,c,*]

[a] Division of Materials and Manufacturing Science, Osaka University, 2-1 Yamadaoka, Suita, Osaka 565-0871, Japan.
[b] Nanostructures Research Laboratory, Japan Fine Ceramics Center, 2-4-1 Mutsuno, Atsuta, Nagoya 456-8587, Japan.
[c] Anisotropic Design & Additive Manufacturing Research Center, Osaka University, 2-1 Yamadaoka, Suita, Osaka 565-0871, Japan

ARTICLE INFO

Article history:
Received 28 February 2021
Revised 1 May 2021
Accepted 8 May 2021
Available online 24 May 2021

Keywords:
Dislocation
Thermal conductivity
Materials design
Molecular dynamics
Anisotropy

ABSTRACT

We report numerical analyses to examine the impact of edge dislocation onto phonon thermal conduction in its vicinity. Two types of edge dislocations, one with open core and another with densely-packed core, show different magnitude of suppression of thermal conductivity across dislocation lines, more than crystallographic anisotropy. It is also found that small density of dislocations effectively scatters phonons lowering thermal conductivity while higher density of dislocations is less effective to suppress thermal conduction. Detailed analyses on bond strains and atomic vibrational states indicated that, while linear dependence of atomic thermal conductivity is found when bond strain is small as in elastic strain field, non-linear/anharmonic dependence of atomic thermal conductivity emerges for the highly strained and under-coordinated atoms at the cores. A combination of these leads to remarkable suppression in thermal conductivity at non-arrayed dislocations even if atoms are positioned away from dislocation core.

Extensive studies of dislocations for many decades have enabled us to go further toward nanostructures. Those include pioneering studies Hall and Petch for hardening [1,2], which are paralleled by theoretical studies by Peierls, Cottrell, Read and Shockley and Eshelby et al., to name just a few [3–6], followed by transmission electron microscopy observation [7]. All of these have facilitated in-depth understanding of structure-property relationships mainly of mechanical properties even for complicated materials including nanostructured materials in terms of nucleation or transient dislocations [8–13], in conjunction with computational atomistic modeling techniques including those by molecular dynamics simulations with classical force fields [14–16] and *ab initio* calculations [17–21], and recently also by machine learning [22].

Attempts have been made to exploit dislocations for more diverse properties other than mechanical properties. The roles of dislocations on colossal pipe diffusion [23–25] and epitaxial growth are well known. However, most of them often remain to remove detrimental effects of dislocations or make them benign against the target properties of materials [26–29]. Recently, a new strategy for molecular decoding by utilizing dislocation is proposed [30]. With an aid of pipe diffusion along dislocations, conducting nanowires are realized in an insulator material [31]. Photo-assisted/impeded plastic deformation is experimentally demonstrated for a semiconductor material [32], which can be attributed to interplay between photons, electrons and dislocations [33].

More successful results have been obtained for possible applications for thermoelectrics where conflicting demands for two transport properties of quantum waves persist. One of pioneering study reported that increased dislocation density together with grain boundaries (GBs) and vacancies by high pressure torsion (HPT) successfully suppress phonon thermal conductivity, thereby increasing the thermoelectric conversion efficiency [34]. Misfit dislocations and arrays of dislocations, or low angle GBs, are found to be effective to suppress thermal conductivity (especially when dopant segregation occurs), while minimizing detrimental impact on electronic counterparts [35–39] . Following those geometrically-necessary (GN) dislocations, it has been experimentally confirmed that statistically-stored (SS) dislocations also play pivotal role for controlling phonon thermal conductivity [40,41], which opens up a new way to maximizing the thermoelectric figure of merit through careful tailoring of microstructures or nanostructures. However, interpretation of those favorable results rely on conventional analytical theories [42,43] proposed many decades ago, while large deviation from Matthiessen's sum rule is reported [44].

A pioneering work by Klemens proposed phonon scattering by dislocations based on a discrete lattice model with nonlinear elas-

---

[*] Corresponding author.
E-mail address: yoshiya@mat.eng.osaka-u.ac.jp (M. Yoshiya).

https://doi.org/10.1016/j.scriptamat.2021.113991

ticity theory where dislocations are described by an array of vacancies with elastic strain field around it [42,43], which remain unchanged in updates for nanostructures by Cahill et al [44,45]. In contrast, Fujii et al. recently demonstrated that thermal conductivity near arrayed GN dislocations, or low angle tilt GBs, depends highly on the atomic structures of dislocations, where a dislocation core with lower number density of atoms is more effective for reducing thermal conductivity [46]. In addition, they also revealed that even small bond strains near GN dislocations can dramatically reduce thermal conductivity, through the development of a model that predicts GB thermal conductivity from their atomic structures [47].

It is expected, however, that isolated SS dislocations introduce different impact on thermal conduction in its vicinity compared with the ones by GBs where strain fields of arrayed GN dislocations can be cancelled out. Lack of precise understanding of the influence of SS dislocations on phonon thermal conduction impedes further attempts by experiments as introduction or annihilation of SS dislocation through thermal materials processing inevitably accompanies rapid vacancy diffusion and slow grain growth. Thus, in this study, numerical analyses are performed to understand the roles that SS dislocation play on thermal conduction using molecular dynamics.

To evaluate and analyze thermal conductivity, we used perturbed molecular dynamics method [48]. For this purpose we have added custom-written codes to LAMMPS package [49]. Advantages of using it in this study over other methods includes direct quantifications of thermal conductivity based solely on motions of atoms, without artificial phonon scatterings which complicates the analyses or any assumption regarding phonon scatterings. In this method, thermal conductivity is obtained as a function of temporal average of microscopic heat flux, **J**, which is given by

$$\mathbf{J} = \sum_i \mathbf{J}_i = \sum_i \frac{1}{2V}\left[\left\{m_i\mathbf{v}_i^2 + \sum_j \phi_{ij}\right\}\mathbf{I}\cdot\mathbf{v}_i - \sum_j \left(\mathbf{F}_{ij}\cdot\mathbf{v}_i\right)\mathbf{r}_{ij}\right] \qquad (1)$$

where m_i and $\mathbf{v}_i$ are mass and velocity of atom i, ϕ_{ij} denotes internal energy determined by interatomic interaction, V is volume of a supercell, $\mathbf{F}_{ij}$ is a force exerted from atom j to atom i, $\mathbf{r}_{ij} = \mathbf{r}_j - \mathbf{r}_i$ with $\mathbf{r}_i$ being a position of atom i, and $\mathbf{I}$ is a unit tensor of second rank. Since the summation is taken over all the atoms, atomic heat flux, $\mathbf{J}_i$, can be unambiguously determined [48,50]. Phonon thermal conductivity is then given by,

$$\kappa_{\mathrm{ph}} = \sum_i \kappa_i = \sum_i \frac{1}{\mathbf{F}_{\mathrm{ext}}T} \lim_{t\to\infty} \langle \mathrm{J}_i \rangle_t \qquad (2)$$

where T is target temperature of a system. In this method, small amount of perturbation which is determined by current instantaneous microscopic heat flux is added to the equation of motion. Its magnitude and direction are determined by an adjustable parameter, $\mathbf{F}_{\mathrm{ext}}$, to the extent it generates non-zero heat flux within the linear response regime. Dependence on it disappears by dividing temporal average of heat flux by it. Because of this relationship between overall thermal conductivity and microscopic heat flux of each atom, contributions of each atom to overall thermal conductivity, which hereafter is referred to as atomic thermal conductivity, can be uniquely decomposed to. This enables mapping of atomic thermal conductivity around dislocations [46,48,50,51]. As shown in Eq. (2), atomic thermal conductivities are extensive variables but can be readily converted to intensive variables by dividing the heat flux (Eq. (1)) by the volume per atom instead of the volume of a supercell [51].

In this study, rock-salt structured MgO is chosen as a model material. Taking into account the fact that the difference in ionic radii between O and Mg is greater than atomic radii of Fe and C, this crystal is actually formed by FCC sublattice of large O ions with small Mg ions at its octahedral sites, in common with other variety of oxides and also with metals. This enables comparison with them and extension of findings to those materials. Interatomic bonding between Mg and O is highly ionic and nondirectional, and thus simple classical pair-wise Buckingham potential is used [52]. This yields thermal conductivity of 119.2 W/mK for a single crystal. The overestimation of thermal conductivity compared with the experimental value (~ 50 W/mK [53,54]) can be mainly attributed to the effects of isotopes, impurities and pores in experimental samples [46]. We intentionally neglect these effects to focus on the relative changes of thermal conductivity caused solely by dislocations. In addition, the group velocities of phonons in MgO are overestimated with the employed Buckingham potential compared with that obtained by *ab initio* calculations (see Figs. S1 and S2 in Supplementary Materials). However, the shape of phonon dispersions is well represented with this potential, and thus it is plausible to assume that phonon transport and its scattering mechanism is also well represented.

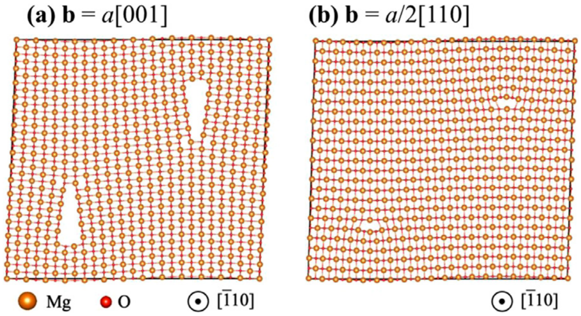

Fig. 1. Edge dislocation models with the Burgers vectors of (a) *a*[001] and (b) *a*/2[110]. The dislocation densities are about 7 × 10^{16} m^{-2}.

Supercells with dislocations are constructed as follows: At first two crystal slabs oriented along dislocation line, one with an extra half plane and one without it, are adjoined. The two adjoined slabs with a dislocation in each are then adjoined to form a supercell such that Burgers vectors of two edge dislocations are antiparallel and two edge dislocations are placed at farthest and most stable positions at an angle 45 degrees between two dislocation cores according to the Peach-Koehler equation. For each type of dislocation, models were constructed with different dislocation densities ρ up to about 7 × 10^{16} m^{-2}.

The dimensions of each supercell were determined under a constant pressure condition (1.013 × 10^5 Pa) by molecular dynamics for 100 ps at 300 K. Thermal equilibrium without the perturbation after 400 ps and steady state with the perturbation after 3 ns are achieved under a constant volume condition using Nosé-Hoover thermostat. Then, thermal conductivity was measured with the perturbation for 7 ns with reliable statistical accuracy. Multiple $\mathbf{F}_{\mathrm{ext}}$ are used to ensure that the system stays within linear response regime and for statistical accuracy of independently measured thermal conductivity including atomic thermal conductivity.

In this study, we investigated the impact of two different edge dislocations with a line vector $\mathbf{t} = [\bar{1}10]$ on the phonon thermal conductivity. One has an open dislocation core with a Burgers vector $\mathbf{b} = a[001]$ and the other has a densely packed core with $\mathbf{b} = a/2[110]$ (Fig. 1), where a corresponds to the lattice constant of MgO. Hereafter, these dislocations are referred to as [001] and 1/2[110] dislocations, respectively. The constructed cell for [001] dislocation with $\rho \cong 7 \times 10^{16}$ m^{-2} has the dimensions of 53.3 × 50.5 × 20.8 Å and contains 5880 atoms. Here, we focus on the thermal conduction across dislocation lines, because the suppression of thermal conductivity is much significant compared with those along the dislocation lines (see Fig. S3 in Supplementary Materials for details).

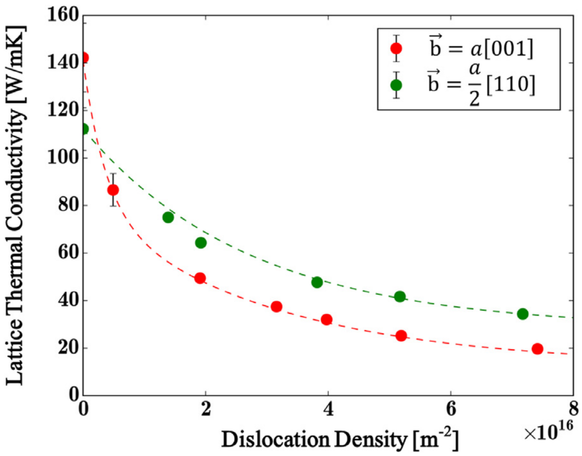

Fig. 2. Lattice thermal conductivity as a function of dislocation density for two edge dislocations with $\mathbf{b} = a[001]$ and $a/2[110]$.

Fig. 2 compares the dislocation-density dependence of phonon thermal conductivity between [001] and 1/2[110] dislocations. Thermal conductivity with no dislocations ($\rho = 0$) was also plotted in the figure to show the orientation dependence of single crystalline thermal conductivity. Introducing small density of dislocations steeply reduced the thermal conductivity, followed by gradual decreases with increasing ρ. The reduction of thermal conductivity is more evident for [001] dislocation with the open cores, as the thermal conductivity is always lower than that of 1/2[110] dislocation despite the higher single crystalline thermal conductivity. Especially, with the very high ρ of about 7×10^{16} m^{-2}, the thermal conductivity of 1/2[110] dislocation model is almost doubled that of [001] dislocation model. This indicates that open dislocation cores, which has lower atomic number density and more ruptured bonds, are more effective to decrease the thermal conductivity, while densely packed cores are less influential. This trend is consistent with the results of the low-angle tilt GBs (arrayed GN dislocations).

To investigate the suppression mechanism of thermal conduction in the vicinity of the dislocation cores, we calculated atomic thermal conductivities for $\rho \cong 7 \times 10^{16}$ m^{-2}, and projected them to a two dimensional plane (Fig. 3a). In both dislocation models, atomic thermal conductivities were substantially decreased not only in the vicinity of dislocation cores but also in the region away from them; the maximum of atomic thermal conductivities is 43 W/mK in 1/2[110] dislocation model, which is almost one thirds of the single crystalline thermal conductivity of MgO (119.2 W/mK) calculated in this study. The [001] dislocation model exhibits much lower atomic thermal conductivities at any region compared to the 1/2[110] model. These results demonstrate that the influence of dislocation cores on thermal transport is spatially widespread, especially when the dislocation core has an open structure.

Fig. 3a also shows that atomic thermal conductivities are relatively high at the region including an extra half plane and low between the dislocation cores, implying that the strain fields near the dislocation cores modify the thermal transport at the nanoscale. Thus, we estimated the bond strain of each atom according to the following definition:

$$\varepsilon_i = \frac{\sum_i^{CN_i} l_{ij} - l_{\text{bulk}} \times CN_i}{l_{\text{bulk}} \times CN_i}, \tag{3}$$

where ε_i is the bond strain of atom i, CN_i is the coordination number, l_{ij} and l_{bulk} are the distances from atom i to the nearest neighbor atom j in the dislocation model and the bulk model, respectively. The two-dimensional maps of the bond strains are plotted in Fig. 3b. A typical strain field pair was found for both dislocations, where the extra half plane induced the compressive strain while the other side was subjected to the tensile strain. Comparing Fig. 3a and 3b, it can be seen that there is a strong correlation between the bond strains and atomic thermal conductivities, i.e., thermal conductivity is relatively large when the bonds are compressed, and vice versa. Indeed, our separate calculations on the uniformly compressed or expanded MgO single crystals revealed that the compressive (tensile) strains increase (decrease) the lattice thermal conductivity significantly (See Fig. S4 in Supplementary Materials).

Fig. 3c displays the differences in the mean square displacement (MSD) of each atom compared to the bulk MgO relative to its average over all directions. The MSD values correspond to the amplitudes of atomic vibrations. As seen from the comparison of Fig. 3b and 3c, the bond strain is correlated well with the MSD in both dislocation models, indicating that compressed bonds lead to the stronger interactions Mg and O ions and thereby smaller MSD, and vice versa. The bond strain apparently modifies the dynamical behavior of atoms, disrupting their collective motions and consequently reducing the thermal conductivity. It was also found from Fig. 3c that the MSD values significantly increased for the under-coordinated atoms at the cores and their neighboring atoms. These atoms exhibit very low atomic thermal conductivities as shown in Fig. 3a, due to the largely anharmonic vibrations induced by the coordination deficiencies at the cores.

To gain a more quantitative understanding, the atomic thermal conductivities are plotted as a function of the bond strain in Fig. 4, by taking the average of them for each 0.5% of bond strain ε. Only fully coordinated atoms (CN = 6) were included in this figure to separate the impacts of bond strains and coordination deficiencies. The difference in atomic thermal conductivities between [001] and 1/2[110] models is as large as 15.3 W/mK at $\varepsilon = 0\%$, demonstrating the large scattering effect of the open core structure. In both [001] and 1/2[110] dislocations, atomic thermal conductivities linearly decreased as the bond strain increased, especially in the range of -0.5% $\leq \varepsilon \leq$ 0.5%. The magnitudes of decreases are 5.1 W/mK for [001] dislocation and 7.6 W/mK for 1/2[110] dislocation, respectively, which are non-negligible considering their overall thermal conductivities of 20 and 34 W/mK. These results quantitatively showed that the suppression of thermal conductivity can be attributed not only to the scattering by the cores but also to the strain field in its vicinity.

In addition, non-linear/anharmonic influence of bond strains onto atomic thermal conductivity is quantitatively demonstrated in Fig. 4. The compressive strains with $\varepsilon <$ -0.5% did not increase the atomic thermal conductivities, probably due to the significant bond strains near the dislocation cores that is non-uniform not only in lengths but also in angles. On the other hand, with larger tensile strains, atomic thermal conductivities continued to decrease in 1/2[110] model, while they plateaued out in [001] model. The large tensile strains would be less effective near the open core structure because the thermal conductivity is already significantly reduced. With the large tensile strain of $\varepsilon = 1.5\%$, atomic thermal conductivities are as low as 17.9 ± 2.8 W/mK for [001] dislocation model and 21.9 ± 2.7 W/mK for 1/2[110] dislocation model, respectively. The value for 1/2[110] dislocation model is comparable to that of the under-coordinated atoms at the dislocation core (21.2 ± 4.7 W/mK), indicating the large impact of bond strains. On the other hand, the under-coordinated atoms in [001] dislocation model exhibit much lower atomic thermal conductivity of 11.2 ± 6.2 W/mK compared with that of the fully coordinated atoms. The different trends between two dislocation cores are due to the different magnitude of anharmonic vibrations as suggested in the results of MSD (Fig. 3c): the under-coordinated atoms at the [001] dislocation core vibrates with larger MSD values (larger am-

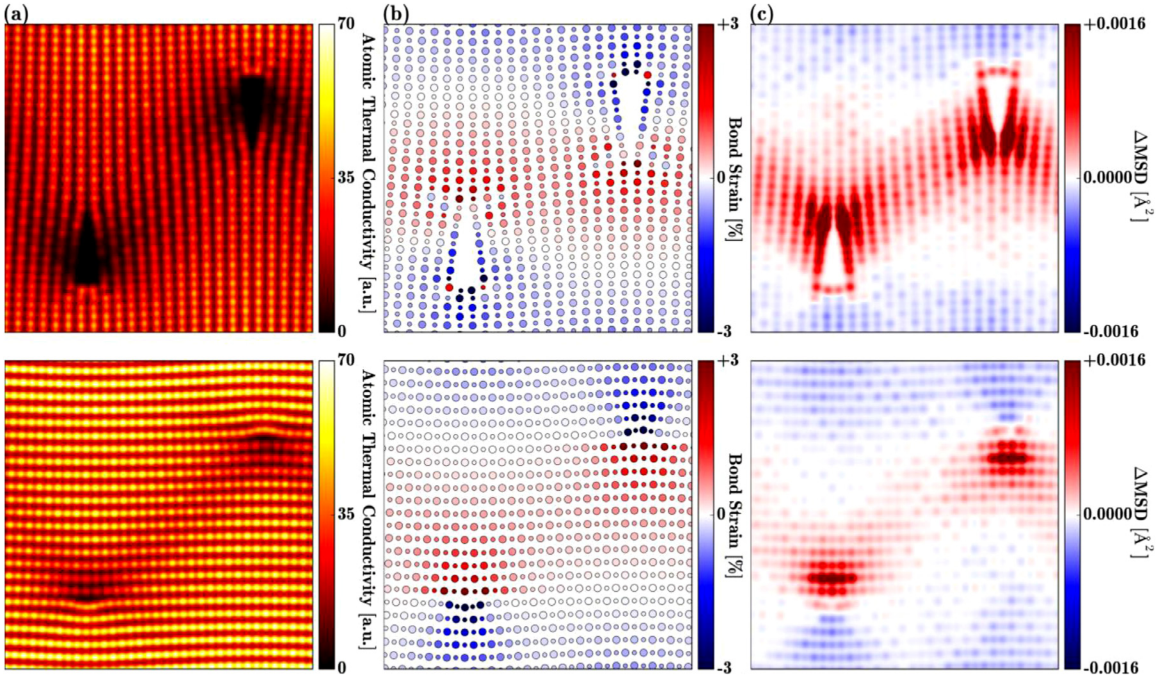

Fig. 3. Two-dimensional maps of (a) atomic thermal conductivities, (b) bond strains, and (c) differences in mean square displacements ΔMSD, compared to the bulk MgO. The upper and lower panels show the results of two edge dislocations with **b** = a[001] and a/2[110].

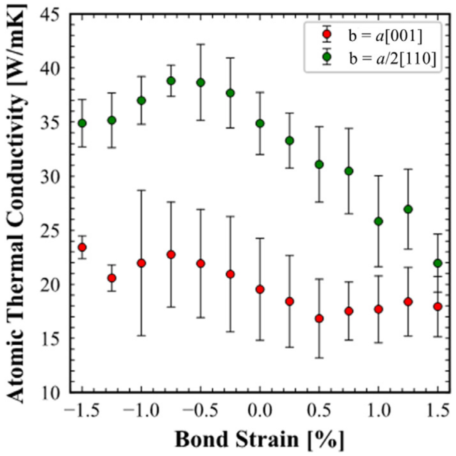

Fig. 4. Atomic thermal conductivities as a function of bond strain for two edge dislocations with **b** = a[001] and a/2[110].

plitudes) than those at the 1/2[110] dislocation core. These results demonstrated that nanoscale thermal conduction near dislocations is highly dependent on the local distortion such as bond strains and coordination deficiencies induced by the different types of the core structures.

In summary, we performed numerical analyses of phonon thermal conduction in the vicinity of edge dislocations in MgO by means of perturbed molecular dynamics. The main factors in disturbing the collective vibrations of atoms are found to be the dislocation core structures with coordination deficiencies and linear/nonlinear bond strains, beyond the simple description as one-dimensional obstacles and associated linear-elastic strain field deduced earlier. These then suppress atomic thermal conductivity, not only of atoms in the vicinity of the dislocation core but also of atoms away from the dislocation core. As a consequence, overall thermal conduction is suppressed by the dislocations, and dependence of thermal conductivity on dislocation density becomes nonlinear.

Author contributions

WS performed theoretical calculations and analyses. SF and MY advised on the calculations and analyses. MY and SF designed the study. All authors discussed the results and wrote the manuscript.

Declaration of Competing Interest

The authors declare no competing financial interest.

Acknowledgments

This study is in part supported by Grant-in-Aid for Scientific Research on Innovative Areas ‘New Materials Science on Nanoscale Structures and Functions of Crystal Defect Cores’ [Grant Number: JP19H05786]. SF was also supported by Grant-in-Aid for Scientific Research [Grant Numbers: JP20H05195 and JP20K15034]. MY was also supported by Grant-in-Aid for Scientific Research [Grant Number: JP20K05062].

Supplementary materials

Supplementary material associated with this article can be found, in the online version, at doi:10.1016/j.scriptamat.2021.113991.

References

[1] E.O. Hall, Proc. Phys. Soc. Sect. B 64 (1951) 747–753.
[2] N.J. Petch, J. Iron Steel Inst. 174 (1953) 25–28.
[3] R. Peierls, Proc. Phys. Soc. 52 (1940) 34–37.
[4] A.H. Cottrell, B.A. Bilby, Proc. Phys. Soc. Sect. A 62 (1949) 49–62.
[5] W.T. Read, W. Shockley, Phys. Rev. 78 (1950) 275–289.
[6] J.D. Eshelby, W.T. Read, W. Shockley, Acta Metall. 1 (1953) 251–259.
[7] P.B. Hirsch, R.W. Horne, M.J. Whelan, Philos. Mag. 1 (1956) 677–684.
[8] R.J. Asaro, S. Suresh, Acta Mater. 53 (2005) 3369–3382.
[9] S. Suresh, J. Li, Nature 456 (2008) 716–717.

[10] P. Gu, B.K. Kad, M. Dao, Scr. Mater. 62 (2010) 361–364.
[11] P. Gu, M. Dao, R.J. Asaro, S. Suresh, Acta Mater. 59 (2011) 6861–6868.
[12] L.Y. Chen, M. He, J. Shin, G. Richter, D.S. Gianola, Nat. Mater. 14 (2015) 707–713.
[13] J. Li, Nat. Mater. 14 (2015) 656–657.
[14] J. Wang, R.G. Hoagland, J.P. Hirth, A. Misra, Acta Mater. 56 (2008) 5685–5693.
[15] T. Zhu, J. Li, A. Samanta, A. Leach, K. Gall, Phys. Rev. Lett. 100 (2008) 025502.
[16] K. Dang, D. Bamney, L. Capolungo, D.E. Spearot, Acta Mater. 185 (2020) 420–432.
[17] G.P.M. Leyson, L.G. Hector, W.A. Curtin, Acta Mater. 60 (2012) 3873–3884.
[18] D. Rodney, L. Ventelon, E. Clouet, L. Pizzagalli, F. Willaime, Acta Mater. 124 (2017) 633–659.
[19] G. Hachet, L. Ventelon, F. Willaime, E. Clouet, Acta Mater. 200 (2020) 481–489.
[20] L. Casillas-Trujillo, D. Gambino, L. Ventelon, B. Alling, Phys. Rev. B 102 (2020) 094420.
[21] A. Togo, I. Tanaka, Scr. Mater. 108 (2015) 1–5.
[22] A. Pandey, R. Pokharel, Scr. Mater. 193 (2021) 1–5.
[23] R.L. Tallman, E.A. Gulbransen, Nature 218 (1968) 1046–1047.
[24] A. Pertsinidis, X.S. Ling, Nature 413 (2001) 147–150.
[25] K. Otsuka, A. Kuwabara, A. Nakamura, T. Yamamoto, K. Matsunaga, Y. Ikuhara, Appl. Phys. Lett. 82 (2003) 877–879.
[26] S.F. Chichibu, A. Uedono, T. Onuma, B.A. Haskell, A. Chakraborty, T. Koyama, P.T. Fini, S. Keller, S.P. DenBaars, J.S. Speck, U.K. Mishra, S. Nakamura, S. Yamaguchi, S. Kamiyama, H. Amano, I. Akasaki, J. Han, T. Sota, Nat. Mater. 5 (2006) 810–816.
[27] D. Liang, J.E. Bowers, Nat. Photonics 4 (2010) 511–517.
[28] P. Yan, J. Zheng, M. Gu, J. Xiao, J.-G. Zhang, C.-M. Wang, Nat. Commun. 8 (2017) 14101.
[29] S.D. Lester, F.A. Ponce, M.G. Craford, D.A. Steigerwald, Appl. Phys. Lett. 66 (1995) 1249–1251.
[30] Y. Takashima, V.M. Martínez, S. Furukawa, M. Kondo, S. Shimomura, H. Uehara, M. Nakahama, K. Sugimoto, S. Kitagawa, Nat. Commun. 2 (2011) 168.
[31] A. Nakamura, K. Matsunaga, J. Tohma, T. Yamamoto, Y. Ikuhara, Nat. Mater. 2 (2003) 453–456.
[32] Y. Oshima, A. Nakamura, K. Matsunaga, Science 360 (2018) 772–774.
[33] K. Matsunaga, S. Hoshino, M. Ukita, Y. Oshima, T. Yokoi, A. Nakamura, Acta Mater. 195 (2020) 645–653.
[34] G. Rogl, D. Setman, E. Schafler, J. Horky, M. Kerber, M. Zehetbauer, M. Falmbigl, P. Rogl, E. Royanian, E. Bauer, Acta Mater. 60 (2012) 2146–2157.
[35] S.-H. Lo, J. He, K. Biswas, M.G. Kanatzidis, V.P. Dravid, Adv. Funct. Mater. 22 (2012) 5175–5184.
[36] S. Il Kim, K.H. Lee, H.A. Mun, H.S. Kim, S.W. Hwang, J.W. Roh, D.J. Yang, W.H. Shin, X.S. Li, Y.H. Lee, G.J. Snyder, S.W. Kim, Science 348 (2015) 109–114.
[37] H. Zhao, B. Cao, S. Li, N. Liu, J. Shen, S. Li, J. Jian, L. Gu, Y. Pei, G.J. Snyder, Z. Ren, X. Chen, Adv. Energy Mater. 7 (2017) 1700446.
[38] H. Mun, K.H. Lee, S.J. Yoo, H.-S. Kim, J. Jeong, S.H. Oh, G.J. Snyder, Y.H. Lee, Y.-M. Kim, S.W. Kim, Acta Mater. 159 (2018) 266–275.
[39] N. Goel, E.B. Webb, A. Oztekin, J.M. Rickman, S. Neti, J. Appl. Phys. 118 (2015) 115101.
[40] V. Karthikeyan, C.M. Arava, M.Z. Hlaing, B. Chen, C.H. Chan, K.-H. Lam, V.A.L. Roy, Scr. Mater. 174 (2020) 95–101.
[41] Z. Chen, Z. Jian, W. Li, Y. Chang, B. Ge, R. Hanus, J. Yang, Y. Chen, M. Huang, G.J. Snyder, Y. Pei, Adv. Mater. 29 (2017) 1606768.
[42] P.G. Klemens, Proc. Phys. Soc. Sect. A 68 (1955) 1113–1128.
[43] P.G. Klemens, in: F. Seitz, D. Turnbull (Eds.), Solid State Phys., Academic Press, 1958, pp. 1–98.
[44] D.G. Cahill, P.V. Braun, G. Chen, D.R. Clarke, S. Fan, K.E. Goodson, P. Keblinski, W.P. King, G.D. Mahan, A. Majumdar, H.J. Maris, S.R. Phillpot, E. Pop, L. Shi, Appl. Phys. Rev. 1 (2014) 011305.
[45] D.G. Cahill, W.K. Ford, K.E. Goodson, G.D. Mahan, A. Majumdar, H.J. Maris, R. Merlin, S.R. Phillpot, J. Appl. Phys. 93 (2003) 793–818.
[46] S. Fujii, T. Yokoi, M. Yoshiya, Acta Mater 171 (2019) 154–162.
[47] S. Fujii, T. Yokoi, C.A.J. Fisher, H. Moriwake, M. Yoshiya, Nat. Commun. 11 (2020) 1854.
[48] M. Yoshiya, A. Harada, M. Takeuchi, K. Matsunaga, H. Matsubara, Mol. Simul. 30 (2004) 953–961.
[49] S. Plimpton, J. Comput. Phys. 117 (1995) 1–19.
[50] M. Tada, M. Yoshiya, H. Yasuda, Proc. Phys. Soc. Sect. A 68 (1955) 1113–1128.
[51] S. Fujii, M. Yoshiya, J. Electron. Mater. 45 (2016) 1217–1226.
[52] J.D. Gale, J. Chem. Soc. Faraday Trans. 93 (1997) 629–637.
[53] A.M. Hofmeister, Phys. Chem. Miner. 41 (2014) 361–371.
[54] D.A. Dalton, W.-P. Hsieh, G.T. Hohensee, D.G. Cahill, A.F. Goncharov, Sci. Rep. 3 (2013) 2400.